Mass Sensing with Graphene and Carbon Nanotube Mechanical Resonators

Doctoral Thesis

Universitat Politècnica de Catalunya (UPC)
ICFO - The Institute of Photontic Sciences

Doctoral Thesis

Jil Schwender

Supervisor:
Prof. Dr. Adrian Bachtold

Thesis committee:
Prof. Dr. Martino Poggio
Dr. Alexander Eichler
Dr. Robert Sewell

Barcelona, September 27, 2018

"On ne fait jamais attention à ce qui a été fait;
on ne voit que ce qui reste à faire"

– Marie Curie

To my family …

Acknowledgements

> "Suppose we were able to share meanings freely without a compulsive urge to impose our view or conform to those of others and without distortion and self-deception. Would this not constitute a real revolution in culture?"
> – David Bohm

First of all I would like to thank my advisor Prof. Dr. Adrian Bachtold for giving me the opportunity to do my PhD in his group and for the valuable guidance throughout the project. The environment has always been highly motivating and encouraging.
I would also like to thank Prof. Dr. Martino Poggio, Dr. Alexander Eichler, and Dr. Robert Sewell for kindly accepting to be part of my thesis committee and for finding the time in their very busy schedule to read my thesis. Moreover, I would also like to express my gratitude towards Prof. Dr. Núria Barniol and Prof. Dr. Romain Quidant for agreeing to serve as substitute members.
Overall, I am sincerely grateful to all the other people people apart from Adrian that were actively involved in the project: Dr. Alexandros Tavernarakis and Dr. Ioannis Tsioutsios from the QuantumNanoMechanics group here at ICFO, Prof. Dr. Urs Staufer from TU Delft and our collaborators from Paris, Dr. Quan Dong and Prof. Dr. Yong Jin. Alex, thanks for your manifold explanations and for your help during the first months. I appreciate your straightforwardness. You helped me to grow as a scientist and as a person. Ioannis, thank you for your patience, kindness and your open ear throughout all our times working together. You were an irreplaceable teacher to me. Even after leaving the group you continued supporting me. During my last year of PhD I was very fortunate to get the chance to work with Urs, learn from such an experienced scientist and get a tremendous amount of help in wrapping up all the previous work I had done and in managing to see the forest for the trees. Urs, thanks for all your detailed corrections and comments on my thesis manuscript and thanks for reminding me that a PhD is not only about the results but also about the process of learning itself. Working with you has encouraged me immensely during my last months of PhD.
Throughout the last years, I had the luck to get experimental support and interact with several other people. There were Dr. Alexander Eichler and Dr. Gustavo Ceballos that both shared their experience with the ultra high vacuum setup with me and this

way saved me lots of extra hours in the lab fixing problems. Moreover, there was Dr. Maria José Esplandiu always available to help with any kind of issue related to the growth of carbon nanotubes or chemistry. Dr. Julien Chaste was so kind to share his expertise of mass sensing with me. Then there were the senior scientists in our group, Dr. Johannes Güttinger and Prof. Dr. Joel Moser, who both have an exceptional and rare talent for explaining science. I am glad that I had a chance to learn from both of you and experience your kindness. Johannes and Niki, thank you for listening and for encouraging me to keep going even during difficult times. Then there was Sergio, even though we never had the chance to work together on the same project I consider you my most faithful colleague since we started our Phd journey at a similar time. At any late hour that I was spending in the lab or the office I could find you around. I will miss our coffee breaks and train trips back to Barcelona that allowed me to share personal and work related thoughts with you. Thanks for your help and advice. Then only when I was close to finish, Dr. Chandan Samanta joined the group. Thanks Chandan for proof reading part of my thesis and for being available for discussions any time. I hope we will go again for some Indian dinner at some point.

I would also like to thank all the past and present members of the group for sharing some time in and outside of the lab. Dr. Peter Weber, Dr. Antoine Reserbat, Nicolas Morell, Jorge Vergara, Dr. Adrien Noury, Dr. Simon Hurand, Slaven Tepsic, Carles Urgell, Dr. Wei Yang and Dr. Gernot Gruber, thank you all for creating this nice atmosphere, for your company, for the fun at the group excursions and for fruitful discussions.

Apart from that I want to thank the people from the clean room and the maintenance for all their support. Luis Enrique and Javier Perez you answered questions fast and solved issues smoothly. Thank you for that. Dr. Johann Osmond, thank your for collaborating in the development of the in-house sample fabrication. The life of an experimentalist at ICFO wouldn't function the same without such a competent and dedicated maintenance team that finds solution for whatever issue in the lab. Thank you Carlos and Luis.

Finally, I want to thank the people that carried me all the way through the up and downs of my PhD thanks to their personal support. There is Anna Fontcuberta who taught me the passion for science and made me take the decision of pursuing a PhD. Anna, I really admire you for being such a great scientist and more importantly for being such a supporting and caring person even beyond my time in your lab. Thank you for all your meaningful advice since the very first day we met. Then there are my friends, from my school and university years, from my Erasmus time, from my time in Lausanne and from my last years at ICFO and in Barcelona. Thank you all for all the moments we shared and for being a part of my life. I am very grateful to have so incredibly diverse friends that enrich my life. Özlem, tesekkür ederim for being my ICFO buddy, for being a great friend and a generous and hospitable person. Marco, thanks for being the first Icfonian from outside the group to start a conversation with me that developed into a friendship. I am looking forward to having you as my neighbor. Anna and Tutu, I am so glad we kept in touch since our good old times. For me you continue being part of my everyday life even though we no longer live in

the same countries. I am happy to know that I can count on you always.
Nicht zuletzt möchte ich meiner Familie danken, ich bin sehr froh dass ich immer auf euch zählen kann, egal was ich tue oder wohin ich auch gehe. Danke, dass ihr meine Lebensentscheidungen respektiert und mich in all meinen Bemühungen unterstützt.
Ignasi, gràcies per ser el meu pilar que ha seguit creixent des del primer dia i per recordar-me les coses importants de la vida.

Barcelona, September 27, 2018

J. S.

Abstract

In recent years, carbon nanotube and graphene mechanical resonators have attracted considerable attention because of their unique properties. Their high resonance frequencies, high quality factors and their ultra-low mass turn them into exceptional sensors of minuscule external forces and masses. Their sensing capabilities hold promise for scanning probe microscopy, magnetic resonance imaging and mass spectrometry. Moreover, they are excellent probes for studying mechanical motion in the quantum regime, investigating nonlinear dynamics and carrying out surface science experiments on crystalline low-dimensional systems.

A goal for fully exploiting the potential of mechanical resonators remains: Reaching the fundamental limit of the resolution of mass sensing imposed by the thermomechanical noise of the resonator. Currently, limitations are typically due to noise in the motion transduction. Nanotube and graphene resonators are particularly sensitive to noise in the detection since their intrinsically small dimensions result in minuscule transduced electrical or optical signals.

This thesis researches ways for improving the mass resolution of the intrinsically smallest mechanical resonator systems, which are based on suspended graphene and carbon nanotubes. For this, we follow two complementary pathways. We first see how far we can go in terms of mass resolution with graphene resonators by reducing their size. We fabricate double clamped graphene resonators with submicron lengths and measure their mechanical properties at 4.2 K. The frequency stability of the resonators allows us to evaluate their mass resolution. We show that the frequency stability of graphene resonators is limited by the imprecision of the detection of the mechanical motion.

We then develop a new electrical downmixing scheme to read-out the mechanical motion with a lower noise compared to previous techniques. It utilizes a RLC resonator together with an amplifier based on a high electron mobility transistor operated at 4.2 K. The signal to noise ratio is improved thanks to signal read-out at higher frequency (1.6 MHz compared to 1-10 kHz) and low temperature amplification. We observe an improved frequency stability measuring a carbon nanotube mechanical resonator with this read-out. The stability is no longer limited by the measurement instrumentation noise but by the device itself. Observing the intrinsic

fluctuations of the resonator allows in future experiments to study surface science phenomena. We present some preliminary results that hint to the observation of the diffusion of xenon atoms on the surface of the resonator and to the adsorption of single fullerene molecules.

Abstracto

En los últimos años, los resonadores mecánicos de nanotubos de carbono y grafeno han atraído una atención considerable debido a sus propiedades únicas. Sus altas frecuencias de resonancia, sus factores de calidad altos y su masa extremadamente baja los convierten en sensores excepcionales de fuerzas externas y masas minúsculas. Sus capacidades de detección son prometedoras para la microscopía con sonda de barrido, la tomografía por resonancia magnética y la espectrometría de masas. Además, son sondas excelentes para estudiar el movimiento mecánico en el régimen cuántico, investigar la dinámica no lineal y llevar a cabo experimentos de ciencia de superficie en sistemas cristalinos de baja dimensión.

La explotación de todo el potencial de los resonadores mecánicos sigue siendo un objetivo: alcanzar el límite fundamental de la resolución de la detección de masas impuesta por el ruido termomecánico del resonador. Actualmente, las limitaciones se deben normalmente al ruido en la transducción de movimiento. Los resonadores de nanotubos y grafeno son particularmente sensibles al ruido en la detección, ya que sus dimensiones intrínsecamente pequeñas producen señales eléctricas u ópticas transducidas minúsculas.

Esta tesis investiga formas de mejorar la resolución de masa de los sistemas de resonadores mecánicos intrínsecamente más pequeños, que se basan en grafeno suspendido y nanotubos de carbono. Para esto, seguimos dos caminos complementarios. Primero vemos hasta dónde podemos llegar en términos de resolución de masa con resonadores de grafeno al reducir su tamaño. Fabricamos resonadores de grafeno de doble sujeción con longitudes submicrométricas y medimos sus propiedades mecánicas a 4,2 K. La estabilidad de la frecuencia de los resonadores nos permite evaluar su resolución de masa. Mostramos que la estabilidad de la frecuencia de los resonadores de grafeno está limitada por la imprecisión de la detección del movimiento mecánico.

Luego desarrollamos un nuevo esquema de downmixing eléctrico para leer el movimiento mecánico con un ruido más bajo en comparación con las técnicas anteriores. Utiliza un resonador RLC junto con un amplificador basado en un transistor de alta movilidad de electrones operado a 4,2 K. La relación señal / ruido se mejora gracias a la lectura de la señal a mayor frecuencia (1,6 MHz en comparación con 1-10 kHz)

y a la amplificación a temperatura baja. Observamos una mejor estabilidad de la frecuencia midiendo un resonador mecánico de nanotubos de carbono con esta lectura. La estabilidad ya no está limitada por el ruido de la instrumentación de medición, sino por el propio dispositivo. Observar las fluctuaciones intrínsecas del resonador permite en futuros experimentos estudiar fenómenos de ciencia de superficie. Presentamos algunos resultados preliminares que apuntan a la observación de difusión de átomos de xenón en la superficie del resonador y a la adsorción de moléculas individuales de fulereno.

Contents

List of Figures

1 Introduction

> ...it might tell us much of great interest about the strange phenomena that occur in complex situations. Furthermore, a point that is most important is that it would have an enormous number of technical applications.
>
> Richard P. Feynman, 1959

1.1 Nanotechnology a retrospect

Today we live in the information age. The speed of computers and the efficiency of storing information have increased tremendously. A life without technology has become in some way unimaginable for us and the world economy. The foundation of all technological advancements in the field of electronics has certainly been the invention of the transistor in 1947 by John Bardeen, Walter Brattain and William Shockley [1]. Only about a decade after, the first working integrated circuit was manufactured at Texas Instruments by Jack Kilby [2]. Since then and until only recently, the number of transistors fit in an integrated circuit of the same size has been doubled every two years. This trend was predicted in the 60's by Gordon Moore, the co-founder of Intel, and is today known all over the world as the Moore's law [3]. Now we have reached a point where we have computer processors that are only 695 mm^2 in size but still made up of 8 billion transistors each having a gate of only 14 nm in size (IBM) (see Figure 1.1 (a)).

This incredible and enduring improvement in the performance of integrated circuits was the result of the miniaturization of transistors. Miniaturization became possible

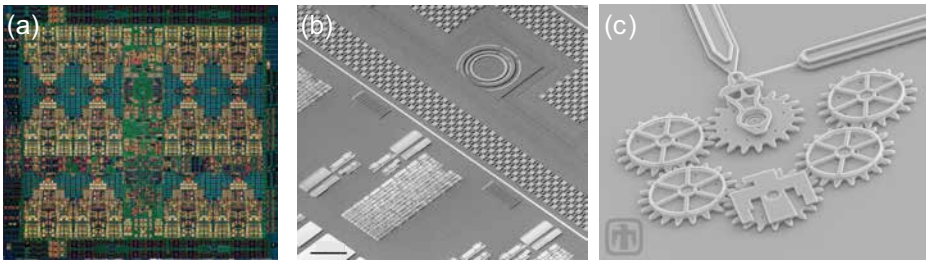

Figure 1.1 – Examples of devices from different areas of nanotechnology. (a) IBM Power9 processor consisting of 8 billion transistors on a chip of 695 mm^2. (b) Integrated electronic-photonic circuit. Ayar Labs, Berkley. (adapted by permission from ©Springer Nature [4]). (c) Six gear chain. Courtesy Sandia National Laboratories, SUMMiT™ Technologies, www.sandia.gov/mstc.

thanks to continuous research which lead to inventions that permit to observe, investigate and manipulate objects down to the level of a single atom or molecule. Among these inventions are imaging techniques such as scanning electron microscopy, atomic force microscopy and transmission electron microscopy as well as fabrication techniques such as electron beam lithography, molecular beam-epitaxy and atomic layer deposition. All of these techniques enable the engineering of new complex structures. In short time this field became known as nanotechnology. The great potential of nanotechnology not only for applications but also for fundamental research had been foreseen by Richard Feynman in his famous speech "plenty of room at the bottom" in 1959. Properties of materials are different at the small scale. For this reason the advances in nanofabrication techniques also led to the possibility of exploring many new and fascinating phenomena. Apart from electronics (see Figure 1.1 (a)), nanotechnology and nanoscience comprise many different areas, among them being nanophotonics (see Figure 1.1 (b)) and nanomechanics (Figure 1.1 (c) shows an example of a micromechanical system). In this thesis we focus on the study of nanoelectromechanical systems (NEMS) which integrate mechanical properties with electrical properties.

1.2 Nanoelectromechanical systems

NEMS belong to the field of nanomechanics. They have emerged from their forerunner, microelectromechanical systems (MEMS) and employ the electrical control of mechanical systems with nanoscale dimensions. Today applications employing MEMS can be found as accelerometers in mobile phones and in car airbags for example, as chemical sensors or as the active element of atomic force microscopes.

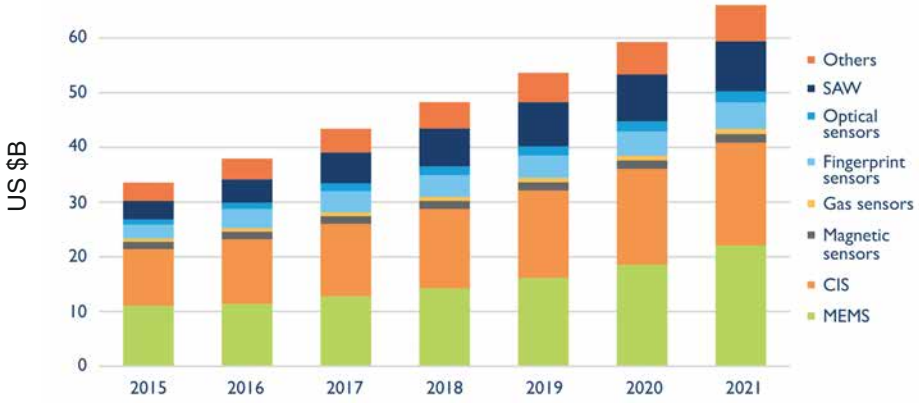

Figure 1.2 – Revenue of sensor and actuator market including MEMS based devices. (Status of the mems industry report, Yole Development 2017).

MEMS based sensing and actuator applications comprise 30% of the total sensor and actuator market share with a growing tendency over the next years (see Figure 1.2). The pathway of miniaturization of NEMS over the last decades has mainly been driven by the demand for better performance but also by their potential for probing unique fundamental properties. Besides, miniaturization of NEMS can result in a cost reduction and the implementation of applications integrated on a single chip. Over the last decades NEMS have proven to posses an unprecedent sensitivity of force [5, 6, 7, 8, 9] , mass [10, 11, 12, 13, 14, 15], charge [16, 17], spin [18, 19] and displacement [20]. The most remarkable experimental accomplishments include the detection of single spins [18] and molecules [21]. Both of which have great perspectives in real life-science application. Additionally, they are promising candidates for radio frequency oscillators [22, 23, 24, 25, 26, 27] and RF applications such as filters [28] and mixers [23]. From a fundamental point of you, NEMS allow to study quantum mechanics. The biggest milestone in this area was the observation of the quantum mechanical ground state by the measurement of zero point fluctuations [29, 30, 31]. All these groundbreaking achievements are owed to the small mass and high resonance frequencies of NEMS compared to micro and macroscopic mechanical systems.

Nanoelectromechanical systems made up of mechanical resonators can come in different dimensions and geometries. Examples are beams (Figure 1.3)(a,c)), cantilevers (Figure 1.3 (b)), strings (Figure 1.3 (c)), sheets (Figure 1.3 (d)) and drums (Figure 1.3 (e)) that can be combined into even more complex coupled systems (Figure 1.3 (f)). Their analogies in the 'macroscopic world' are bridges, springboards, guitar strings

and trampolines. They can be obtained through top down or bottom up fabrication processes. The top-down fabrication method starts-off with a bulk material and creates the desired structure by removing material in a controlled manner. This is done employing lithography techniques together with dry and wet etching processes. The work of a sculptor that carves his piece of art into the stone can picture the top-down approach of fabricating NEMS. Figure 1.3 (a-b) shows examples of resonators that have been fabricated with top down approaches.

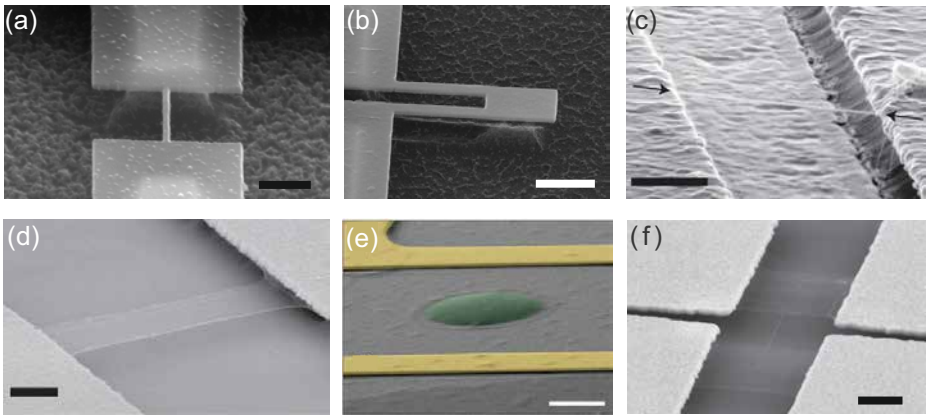

Figure 1.3 – Different NEMS device geometries. (a) Double clamped silicon carbide beam. The scale bar is 1 µm) [32]. (b) Silicon carbide nanocantilever. The scale bar is 1 µm (Roukes Group, Caltech). (c) Double clamped carbon nanotube resonator. The scale bar is 500 nm (adapted by permission from ©Springer Nature [33]). (d) Double clamped graphene sheet resonator. The scale bar is 500 nm (adapted by permission from ©Springer Nature [33]). (e) Graphene drum resonator. The scale bar is 3 µm (adapted by permission from ©Springer Nature [34]). (f) Coupled graphene resonator. The scale bar is 500 nm (adapted by permission from ©AIP Publishing [35]).

The advantage of this technique is that it relies on state of the art technologies used for the fabrication of integrated circuits. This allows for large-scale integration [36] and for implementing a large number of parallel NEMS onto the same chip. Both of which is important for utilizing NEMS in applications. However, top down fabrication of NEMS has also several limitations. The first point is the somewhat modes limit of NEMS dimensions imposed by the resolution limit of lithography techniques. The second problem with this approach is that chemical processes introduce surface defects into the material. Since the surface to volume ratio increases with decreasing device dimensions, so does the relative number of defects. Defects in a material can strongly affect and degrade the material properties. In NEMS the quality factor is typically affected by the number of defects in the material [37].

The bottom-up approach allows to overcome these limitations at the cost of having to find new strategies and processes for enabling reliable large scale integration. It uses the smallest possible building blocks down to the level of atoms and molecules to construct devices. Examples of bottom-up fabricated NEMS are based on nanowires, graphene and carbon nanotubes (see Figure 1.3)(d-e)). Carbon nanotubes and graphene NEMS are especially promising because they constitute the ultimate one and two dimensional material that can be found in nature. While carbon nanotube resonators are more promising sensors due to their small mass, graphene resonators can be more easily fabricated on large scale and therefore compromise both the advantages of top-down and bottom up fabricated NEMS. Moreover, they have a larger surface area that can be exploited in sensing a larger amount of analyte.

1.3 Graphene and carbon nanotube resonators

In recent years, carbon based nanoelectromechanical systems have been in the spot light of the scientific community owed to their low mass, high strength, chemical stability and their unique electronic properties. They have shown to reach resonance frequencies in the GHz regime [38, 39], they exhibit a high resonance frequency tunability [40, 41] and very large quality factors [33, 42, 43]. Moreover they have proven to be unprecedented sensors of external force [8, 44] and mass [12, 15] by the Bachtold group and previously others. All this makes them promising candidates for a number of NEMS based applications and for fascinating fundamental studies. Among promising applications are high frequency switches [45], filters [46, 47] and oscillators [27] and mass spectrometry [21, 48]. In terms of fundamental research they are systems that allow the study of nonlinear effects [33, 49, 50, 51, 52], coupling between mechanical and electrical properties [53, 54, 55] and surface science. In the field of surface science they have been used to observe the formation of atomic monolayers on their surface here in the group [56] and for the study of charge transfer from adsorbed atoms to the atoms of the resonator [57].

Carbon based NEMS have one major challenge: their small dimensions result in minuscule transduced signal in electrical and optical transduction techniques. Therefore many research efforts have been dedicated to the development of efficient transduction techniques that allow to detect the mechanical motion [8, 33, 40, 41, 42, 44, 58, 59, 60].

In pushing the performance of NEMS as mass sensors and high frequency oscillators, using graphene and carbon nanotubes is an inevitable step. Recent studies, however have shown that the ultimate mass sensing capability, limited only by the thermal motion of the devices, has never been actually experimentally observed, for none

of the studied NEMS [61]. The explanation for this is the presence of frequency fluctuations attributed either to noise in the read-out instrumentation or to the interaction of the resonator with its environment. Those fluctuations probably limit the frequency stability of most NEMS. Only few experimental studies could identify the origin of the frequency fluctuations to be related to the device itself [62, 63]. Most of the other works assigned the observed frequency fluctuations to be due to the noise in the measurement instrumentation [54, 64, 65, 66]. In some other cases the origin remained unidentified [43, 61]. Good frequency stability is crucial for the mass resolution of a resonator. Moreover it also gives an indication weather or not the system has potential for replacing macroscopic quartz oscillators. Quartz oscillators are characterized by an exceptional frequency stability. This means that studying and understanding these frequency fluctuations deserves more attention since it plays a key role in exploiting their ultimate performance for applications.

1.4 Thesis motivation and outline

We still continue being fascinated by graphene and nanotube resonators' great potential for NEMS applications and by their fundamental properties. However, we need to urgently find ways to address the remaining central issues that hinder their full exploitation up till today. This thesis works towards understanding and tackling these central issues. We start by pushing the device dimensions of graphene resonators down to the submicron level. In the second part of the thesis we implement an improved read-out scheme that enables the observation of intrinsic frequency fluctuations in carbon nanotube resonators. The outline of this thesis is the following:

Chapter 2 gives an overview over the mechanical and electrical properties of graphene and carbon nanotubes.

Chapter 3 introduces the linear and nonlinear harmonic oscillator used to describe the dynamics of mechanical modes of vibration. Furthermore it discusses beam mechanics needed to understand how material properties and device dimensions define the resonance frequency and the mechanical mode shape.

Chapter 4 summarizes different transduction techniques of mechanical motion with the focus on electrical techniques.

Chapter 5 introduces the basic principle behind the use of resonators as mass sensors and discusses its limitations.

Chapter 6 describes and summarizes the fabrication and characterization of graphene mechanical resonators. Moreover it presents sensing experiments with graphene and discusses the limitations of the mass resolution.

Chapter 7 discusses the implementation of a low noise read-out scheme and demonstrates the observation of frequency fluctuations in carbon nanotube resonators.

2 Graphene and carbon nanotubes

In this chapter we give a short overview on graphene and carbon nanotube research. We summarize the electronic and mechanical properties of graphene and carbon nanotubes owed to their unique crystalline structure.

2.1 Introduction

In 2004, the scientists Andre Geim and Konstantin Novoselov were the first to isolate graphene and experimentally demonstrate some of its unique properties [67]. This was the starting point of a new, amazingly fast growing research field dedicated to the study of graphene and other two-dimensional materials and earned these two researchers from Manchester the Nobel prize in 2010. Until then, graphene was believed to be thermodynamically unstable and thus its properties had only been predicted theoretically. First theoretical studies go back more than 60 years [68]. Today graphene can not only be obtained by mechanical exfoliation from graphite, but also be produced on large scale by chemical vapor deposition (CVD) [69].

Graphene is an atomically thin layer of carbon atoms arranged in a hexagonal lattice. Its carbon atoms are bound by covalent bonds. It is a two-dimensional material and constitutes the building block for the well known bulk material graphite as well as low dimensional carbon based materials such as carbon nanotubes (1-D) and C60 (bucky ball) molecules (0-D) (see Figure 2.1). Graphite consists of different graphene layers bound together by van der Waals forces (see Figure 2.1(d)). Graphene is considered the 'father' of all two-dimensional materials that have been discovered up till today. Some other examples of two-dimensional materials are transition metal dichalcogenides.

Carbon nanotubes, which are basically hollow cylinders made out of rolled up graphene sheets, are known for already much longer than their two-dimensional counterpart. Their experimental discovery by Iijima et al. (1991) [71] goes back to

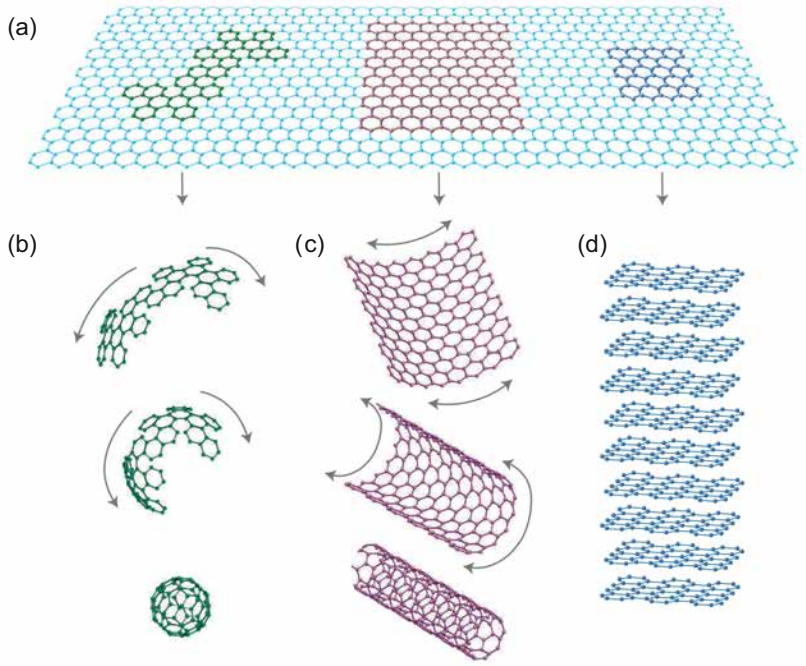

Figure 2.1 – (a) Graphene atomic hexagonal lattice. (b) 0-D buckyballs or fullerenes. (c) 1-D carbon nanotubes made up of rolled up graphene. (d) the 3-D graphite made up off stacked graphene layers (adapted by permission from ©Springer Nature [70]).

the 90's and has initiated its own research field. They can in principle be classified in two different types of carbon nanotubes: single walled carbon nanotubes (SWCNTs) and multi-walled carbon nanotubes (MWCNTs). SWCNTs are typically 1-3 nm in diameter and several μm long. MWCNTs are made up of several SWCNT's concentrically organized in a cylinder. Their diameters can reach up to several tens of nm and they are several μm long. CNTs can be synthesized with different methods such as arc discharge [71, 72], laser ablation [73] or CVD [74]. CVD is used in the work on carbon nanotubes described in this thesis.

Carbon nanotubes and graphene share many of their unique electrical and mechanical properties since they are both made out of hexagonally arranged carbon atoms. We want to discuss these properties briefly in the following paragraphs in order to lay the foundations for understanding the principal mechanism of carbon based nanomechanical resonators and motivate their use as mass sensor.

2.2 Electronic properties

Electronic properties of graphene

Graphene owes its exceptional properties to its unique crystalline structure and symmetry. Carbon atoms have six electrons that occupy the following orbitals: two in 1s, two in 2s, and one each in $2p_x$, $2p_y$. The 1s electrons are generally inert and do not contribute to chemical bonding. Only the other 4 electrons, occupying the outer shell do contribute to the bonding. In the graphene honeycomb lattice the neighboring carbon atoms bond via in-plane covalent bonds formed by the hybridization of the 2s, $2p_x$ and $2p_y$ orbitals. These bonds are also called sp^2 hybridizations or σ-bonds and contain one electron from each carbon atom. They are responsible for the mechanical strength of graphene and form the electronic band structure far away from the Fermi-energy. The fourth electron of each carbon atom, not participating in the sp^2 hybridization, occupies the $2p_z$ orbital which lies perpendicular to the lattice and forms the π-bonds. These π-bonds make up the electronic π-bands which define the electronic properties of graphene near the Fermi-energy. The hexagonal lattice of graphene can be described as a Bravais lattice with a basis of two atoms A and B per unit cell and the unit vectors $\mathbf{a}_1$ and $\mathbf{a}_2$ in real space (Figure 2.2). The distance between two carbon atoms (the carbon-carbon bond length) is $a_{c-c}=a/\sqrt{3}=0.142$ nm. In the reciprocal space this translates into a unit cell described by vectors $\mathbf{b}_1$ and $\mathbf{b}_2$. Its first Brillouin zone has a hexagonal shape with its high symmetric corner points K and K' (Figure 2.2). These symmetry points coincide with the charge neutrality point in the band structure, where valence and conduction band touch each other (Figure 2.3). Calculating the low energy band structure of the π-electrons using the tight binding approximation for the wave functions [68, 75] results in the following energy dispersion for the valance and the conduction band.

$$E(\mathbf{k})=\pm\gamma_0\sqrt{1+4\cos(\frac{a k_x}{2})\cos(\frac{\sqrt{3}a k_y}{2})+4\cos^2(\frac{a k_x}{2})}, \tag{2.1}$$

where k_x and k_y are the wave vectors in x and y direction respectively and γ_0 is the nearest hopping energy. Near the fermi energy, or the Dirac point, this results in a linear dispersion relation

$$E(\mathbf{k})=\hbar v_F|\mathbf{k}|, \tag{2.2}$$

with the Fermi velocity $v_F \approx 10^6$ m/s. Because of this unique electronic band structure in the vicinity of K and K' points, graphene is also described as a zero-bandgap semiconductor. Electrons and holes in graphene have zero effective mass and therefore behave like Dirac Fermions. The bandstructure of graphene can be seen in Figure 2.3. Graphene shows extremely high mobilities (up to 10^6 cm^2/Vs, [76]) and ballistic transport over large length scales (few micrometers) at low temperatures [77].

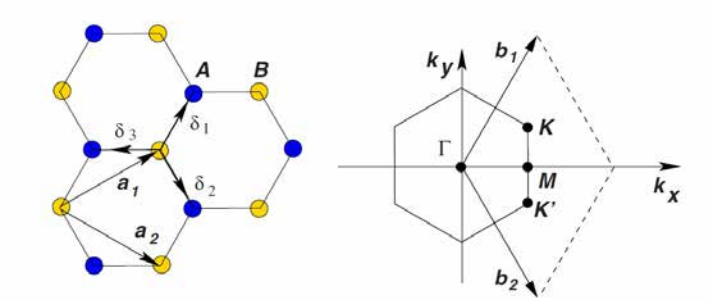

Figure 2.2 – Crystal lattice of graphene.Left: Graphene lattice with its sublattices A and B and its unit vectors $\mathbf{a}_1$ and $\mathbf{a}_2$. Right: Brillouin zone with its high symmetry points K and K' coinciding with the Dirac cones. (reprinted with permission from ©American Physical Society [75].)

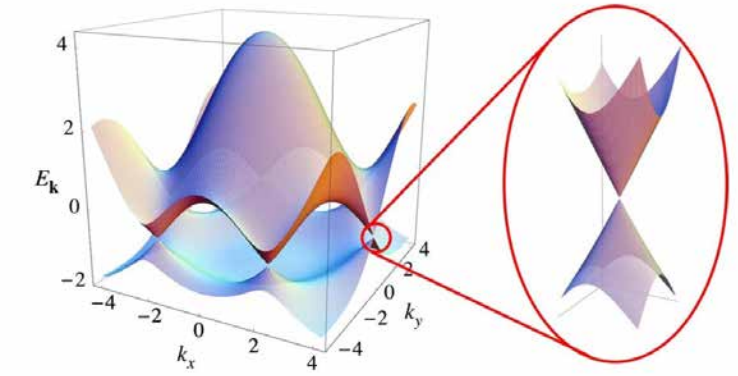

Figure 2.3 – Electronic band structure of graphene. On the right: the band structure in the vicinity of K and K' points (reprinted with permission from ©American Physical Society [75].)

Apart from this, applying a voltage bias on the gate electrode of the graphene device also allows to tune the amount of free charge carriers inside the graphene contributing to the electrical transport and switch from electrons to holes and vice versa. The electrostatic field can shift the Fermi level of the graphene from the valence band

via the charge neutrality point into the conduction band. This is also called the ambipolar field effect and has been observed in graphene by Novoselov et al. [67]. The strong response of the conduction of graphene to an external electric field (also called transconductance) [78] is crucial for the electrical transduction of the mechanical motion and this is exactly what we exploit in the read-out of the mechanical motion throughout this work (chapter 4.2.2).

Electronic properties of carbon nanotubes

The crystal and electronic structure of carbon nanotubes are closely related to that of graphene due to the fact that they both consist of carbon atoms arranged in a honeycomb lattice. Since a single walled carbon nanotube can be described as a rolled up graphene sheet with a specific symmetry axis, one just needs an additional vector that defines the angle between the graphene lattice orientation and the CNT axis. This vector is the chiral vector $\mathbf{C}_\mathrm{h} = n\mathbf{a}_1 + m\mathbf{a}_2$, where n and m are a set of integer numbers. This integer numbers define the diameter and the chiral angle or chirality of the nanotube which result in specific electronic properties (see Figure 2.4 (a)). Depending on their chiral angle nanotubes are classified into three different groups: Armchair (n,n) are all nanotubes which have a chiral angle of 30°, zig-zag (n,0) are all nanotubes with an angle of 0°and chiral nanotubes (n,m) are described by arbitrary chiral angles. The different chiral structure of nanotubes is sketched in Figure 2.4 (b).

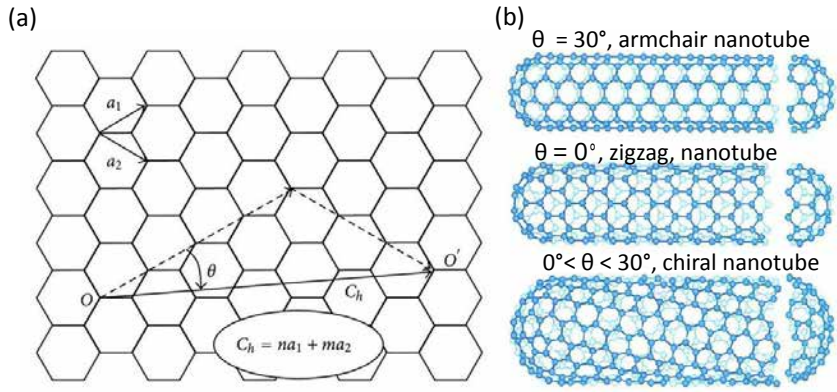

Figure 2.4 – (a) Hexagonal lattice with the chiral angle that defines on which axis the graphene is rolled up to form a nanotube. $\mathbf{C}_\mathrm{h}$ is the chiral vector (adapted from [79]). (b) The chiral angle defines the type of the nanotube. For armchair nanotubes the chiral indices $(n, m = n)$ are equal and the chiral angle is 30°. For zigzag nanotubes the chiral indices are $(n, m = 0)$ and the chiral angle is 0°and for the general case $0 < \theta < 30°$(from www.physics.umd.edu/mfuhrer/ntresearch.htm).

The band structure of carbon nanotubes can be calculated in a similar way as for graphene taking into account periodic boundary conditions [80]. The CNT band structure depends upon its chirality and results in either metallic or semiconductor nature. The boundary conditions lead to allowed states which are equally spaced in the reciprocal k-space. If these states cross the points of zero band gap (K-points) one has a metallic nanotube. If they do not cross the points of zero band gap one has a semiconducting tube (see Figure 2.5). Semiconducting nanotubes have an energy band gap of $E_g = 0.7$ eV/D[nm] [81], where D is the diameter of the nanotube.

Carbon nanotubes conduct charges only in one-dimension due to their hollow structure and their small dimensions, therefore electrical transport in carbon nanotubes can be described by the Landau-Buttiker formalism [82, 83]. This formalism describes transport in low dimensional systems.

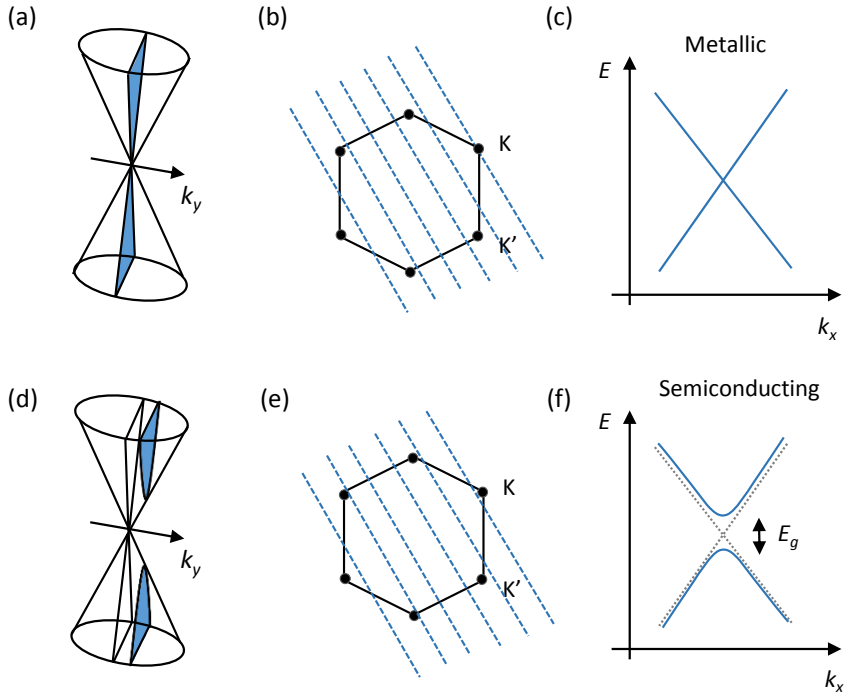

Figure 2.5 – Visualisation of the band structure of (a) metallic and (d) semiconducting nanotubes. (b) Brillouin zone. Allowed states for a metallic nanotube cross the K-points. (c) One dimensional energy dispersion of a metallic nanotube. (e) Brillouin zone. Allowed states for a semiconducting nanotube do not cross the K-points. This leads to the opening of a bandgap as seen in (f). Both (b) and (e) are adapted from [84].

Carbon nanotubes exhibit electron mobilites comparable to graphene (of around 10^4 cm^2/Vs at room temperature [85]). They also show the ambipolar field effect which allows to use a field-effect geometry to read-out the their mechanical motion.

Typically neither nanotubes nor graphene feature a minimum in conductance at zero gate voltage but instead exhibit hole or electron conduction. This is due to the pinning of the Fermi level through the metal contacts and due to surface adsorbates. Both of which results in a certain doping level. The pinning level due to the metal contacts is usually defined by the difference between the work function of the carbon nanotube/graphene and the contact metal and results in a screened field effect. A typical change of the conductance of a carbon nanotube as a function of the gate voltage can be seen in Figure 2.6 (a) for one of the devices studied in this thesis. Here, the contact metal leads to a p-type doping of the nanotube near the electrodes. The free carriers in the suspended part of the nanotube can still be controlled via the electric field. For a gate voltage below 0.4 V the electric transport takes place through hole conduction. At around 0.5 V, the Fermi energy is moved into the bandgap. The Fermi energy is in the electron band for a gate voltage above 0.7 V and transport is mediated through electrons. In this voltage regime a p-n-p junction forms between the suspended part of the nanotube and the metal contacts.

At low temperatures, the thermal energy of the electron $k_B T$ can no longer supply the energy required to charge the junction with a single electron (also known as charging energy $e^2/2C_{tot}$). In this regime, the carbon nanotube behaves like a single electron transistor [87, 88] with discrete energy states. A single electron transistor is basically a quantum dot connected via tunnel junctions to the source and drain electrodes [89, 90]. The source and drain electrodes serve as reservoirs with the electrochemical potentials μ_S and μ_D respectively. The inset of Figure 2.6(b) shows the response of the conductance to the electric field for a carbon nanotube in such a regime for gate voltages above 0.7 V. The observed oscillations in the conductance are also called Coulomb blockade oscillations. The gate electrode, i.e. the third terminal, capacitively couples to the quantum dot and allows to tune its electrochemical potential so that it can get aligned with the electrochemical potentials of the two reservoirs. If the electrochemical potential of the quantum dot is not aligned with the electrochemical potential of the two reservoirs the quantum dot is in a blocked state and the number of charge carriers in the quantum dot remains fixed (Figure 2.6 (c)). If the electrochemical potential of the source is aligned with the quantum dot electrons can tunnel one by one through the tunnel junction into and out of the quantum dot (Figure 2.6 (d)). The coulomb oscillations can exhibit a much larger local transconductance $\frac{dG}{dV_g^{DC}}$ than the one observed at negative gate voltage where no coulomb oscillations are observed (see Figure 2.6(b)). The large transconductance

in the Coulomb oscillation regime can be exploited to get a large electrical signal of the mechanical motion, since in the motion transduction schemes we employ, the electrical signal of mechanical origin is directly proportional to the transconductance (see chapter 4.2.2, equation 4.2).

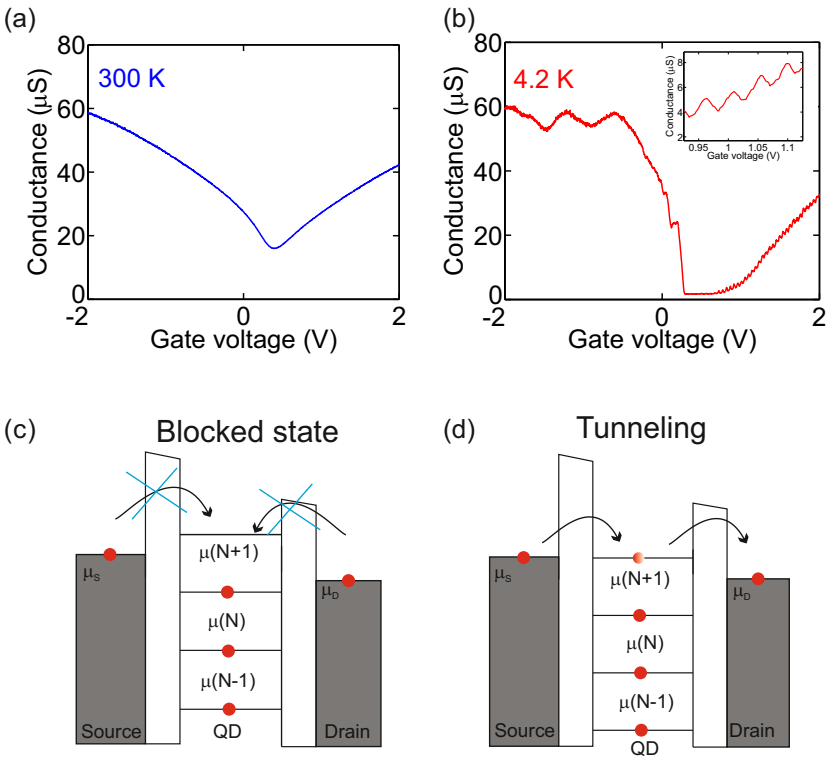

Figure 2.6 – (a) Gate voltage dependence of the conductance of a carbon nanotube device at room temperature. The device still conducts at the charge neutrality point since carriers get thermally activated over the bandgap. (b) Gate voltage dependence of the conductance of a nanotube at 4.2 K. In the positive voltage regime coulomb oscillations become visible (See inset). (c) and (d) show the electrochemical potentials of the three terminal device with source, drain and the quantum dot in between. In (c) the nanotube is in the coulomb blockade regime, where no charge can tunnel through the barrier. (d) The tunneling becomes possible when the electrochemical potential of the quantum dot is aligned with the electrochemcial potential of the source and drain electrodes. Both (c) and (d) are adapted from [86].

The importance of clean devices and ways to achieve them

The electrical properties of carbon nanotubes and graphene previously presented are only observable if the devices contain few defects and little contamination. In graphene and carbon nanotubes the conduction is achieved by the π-bands which lie above the plane of the hexagon-lattice of the carbon atoms. For this reason the conductance of graphene and carbon nanotubes is very receptive to surface changes that can result in unwanted doping. Doping screens the field effect response of carbon nanotubes and graphene resulting in a low transconductance. A large transconductance is crucial for the electrical transduction of the mechanical motion used throughout this thesis (chapter 4.2.2.1). Moreover, clean devices are also desirable for the study of surface science phenomena.

For these reasons, possible sources of contamination must be avoided. The biggest source of contamination is typically coming from the exposure of the nanotube or graphene resonator to chemicals throughout the fabrication processes. Ways to limit the contamination are the use of transfer techniques, where the graphene or the carbon nanotube is transferred in the last step of the fabrication. However, even then, a small amount of contamination is unavoidable. For carbon nanotubes exposure to chemicals can be complectly avoided by growing them over prefabricated trenches in the last step of the fabrication as we explain in chapter 7.3.

Current annealing is a complementary way for achieving clean devices. It allows to remove already present contamination and recover the electrical properties of a clean graphene or carbon nanotube device. In current annealing, a high current (up to μA for nanotubes and up to mA for graphene) is passed through the device. This results in a large dissipation of power and leads to Joule heating, which reduces the number of contaminants drastically. The success in cleaning devices with this process has been demonstrated in the Bachtold group [91]. Since the doping of the device is strongly determined by the level of contamination, removing contamination can recover the properties of a pristine sample. Figure 2.7 shows the electric field response of the conductance of a graphene device before and after current annealing. Only after current annealing the minimum in conductance, indicating the dirac cone, lies close to zero gate voltage. A reduction of the contamination also leads to an improvement of the transconduction, as observed in Figure 2.7. In ultraclean samples the level of doping is due to pinning of the Fermi-level at the electrodes.

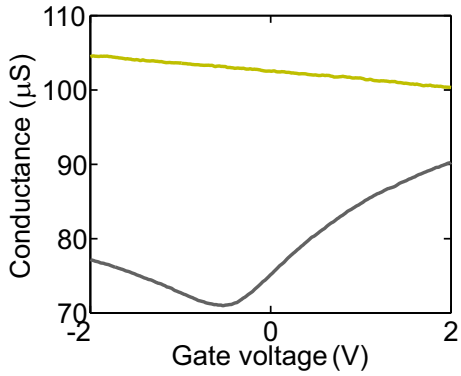

Figure 2.7 – Conductance of a graphene device before (yellow-green) and after (grey) current annealing. The current annealing removes dopants and moves the charge neutrality point close to zero gate voltage

2.3 Mechanical Properties

The exceptional mechanical properties of graphene and carbon nanotubes can be attributed to the strong sp^2 hybridized C-C bonds which result in a very high stiffness (which can be quantified by the Young's modulus). The high stiffness together with the low mass density make them exceptional good systems for high frequency electromechanical resonators.

The two-dimensional Young's modulus describes the ratio between stress σ and strain ϵ inside a material. It gives a measure of the in-plane strength of a material. Graphene and carbon nanotubes have a Young's modulus E with a corresponding bulk value of around 1 TPa. This the highest Young's modulus E ever measured up till today.

The two-dimensional Young's modulus of graphene was experimentally determined to lie around $E_{2D} = 340\,\mathrm{N/m}$. This value corresponds to a bulk value of 1 TPa if we divide it by the spacing between graphene layers in graphite. This value for bulk graphite has already previously been measured [92]. The breaking strength of graphene describes the maximum stress the material can sustain. It has a value of $\sigma_{\mathrm{int}} = 42\,\mathrm{N/m}$ corresponding to a graphite bulk value of around 130 GPa and a strain of 25%. These values were determined for free standing graphene via nanoindentation measurements with an AFM [93] and are the highest values reported so far for any material. This makes graphene the strongest material known. The mass density of

graphene and carbon nanotubes is $\rho_{\text{graphene/NT}}$=7.6x10^{-19} kg/$\mu$m^2.

The Young's modulus of a carbon nanotube could be experimentally determined by pulling a suspended nanotube apart with the use of two AFM tips [94] or by stretching it pushing with an AFM tip from the top [95] in a similar manner as for graphene. Another method extracted the Youngs modulus from measurements of the thermal vibration with electron microscopy [96]. The breaking strength of carbon nanotubes is around 30 GPa corresponding to a strain of 5%, so significantly lower than the one of graphene [94].

As we will see in detail in chapter 3.3, the natural resonance frequency of mechanical resonators is defined by the properties of the material. For all different types of resonators (cantilever, double clamped beam, double clamped membrane) the natural resonance frequency scales as $\propto \sqrt{\frac{E}{\rho}}$. Thanks to their is extremely small ρ and their extremely large Youngs modulus E, graphene and carbon nanotubes have very high resonance frequencies. One can tune the resonance frequency even further by introducing strain via an external electric field. For this reason carbon nanotubes as well as graphene are attractive for applications where high frequencies as well as frequency tuning are important, such as oscillators [25, 26, 27, 97] and mass sensing experiments [11, 12, 13, 14, 15].

3 Nanomechanical resonators

In this chapter we introduce the theoretical description needed to understand and describe the motion of nanomechanical resonators. We first introduce the model of the simple linear harmonic oscillator driven by thermal force. We then describe the vibration of the resonator driven by an external coherent force and go over to the nonlinear systems. In the last part of this chapter we study the beam mechanics of the double clamped beam and the double clamped membrane, represented in our experiments by carbon nanotube and graphene resonators respectively.

3.1 Linear harmonic oscillator

We first consider the motion of a harmonic oscillator in the absence of damping, external driving or mode coupling. A simple harmonic oscillator is related to Hooke's law $F = -k \cdot z$, which assumes a linear relation between restoring force and displacement. In Hooke's law k is the spring constant of the system and z the time dependent displacement. Following Newtons equation, this restoring force also must be equal to $m_{\text{eff}} \cdot \ddot{z}$, where m_{eff} is the effective mass of the resonator (see chapter 3.3.3, equation 3.39) and $\ddot{z}$ its acceleration. From this, we get the equation of an undriven and undamped mechanical system described by the following equation:

$$m_{\text{eff}} \ddot{z}(t) + k z(t) = 0, \tag{3.1}$$

where m_{eff} is the effective mass which is defined by the mode shape of the resonator. The motion, i.e. the time dependent displacement, is then derived by solving equation 3.1 and results in:

$$z(t) = z_0 \exp(i(\omega_0 t + \phi)), \tag{3.2}$$

where ω_0 is the angular mechanical resonance frequency also given by $\omega_0 = \sqrt{(k/m_{\text{eff}})}$ and ϕ is the phase.

A real resonator however always interacts with its environment. The interaction can manifest itself in the form of a force or dissipation. The force can be a random noise force and an external driving force. Dissipation describes an energy loss of the resonator to its environment resulting in a damped motion. Dissipation takes place via the clamping points of the resonator. For this reason, in a more realistic scenario the equation of motion of a harmonic oscillator can be described with two additional terms:

$$m_{\mathrm{eff}}\ddot{z}(t)+m_{\mathrm{eff}}\gamma_{\mathrm{m}}\dot{z}(t)+kz(t)=F(t), \tag{3.3}$$

where γ_{m} is the linear damping rate and $F(t)$ describes any time dependent force which can be for example thermal noise and an intentional external driving force as described later on in this chapter. The important resonator properties are the mechanical resonance frequency $f_0=2\pi\omega_0$, the effective mass m_{eff} and the quality factor Q. The quality factor is the dimensionless figure of merit of a mechanical oscillator which quantifies the damping of the system, it is defined as the total energy stored E_{tot} compared to the energy lost per cycle of vibration $\Delta E_{\mathrm{cycle}}$ as follows:

$$Q=2\pi\frac{E_{\mathrm{tot}}}{\Delta E_{\mathrm{cycle}}}. \tag{3.4}$$

The quality factor can be described by $Q=\omega_0/\gamma_{\mathrm{m}}$. In other words the quality factor estimates the number of cycles the oscillator can sustain till it has lost all its energy to the environment. The amplitude of the damped vibration decays exponentially with a characteristic time constant of $\tau=2Q/\omega_0$.

3.1.1 Thermomechanical motion

The resonator couples and therefore thermalizes with its environment. This thermalization process leads to the energy loss described by the damping of the system. However, this interaction of the resonator with its environment does not only lead to dissipation but also to a randomly fluctuating force $\delta F_{\mathrm{th}}(t)$. It basically relates the dissipative term ($m_{\mathrm{eff}}\gamma_{\mathrm{m}}\dot{z}$) in the equation of motion to the fundamental random thermal fluctuations which drive the resonator. This relation is summarized in the fluctuation-dissipation theorem [98]. This theorem states that in thermal equilibrium the fluctuating thermal forces acting onto the resonator are directly related to the dissipation of the resonator. In the following we will derive this relation (equation 3.12).

The equation of motion for a thermally driven resonator can be described by equation 3.3, where the term for the driving force F_{d} is replaced by $\delta F_{\mathrm{th}}(t)$. Here $\delta F_{\mathrm{th}}(t)$

describes the random thermal fluctuating forces acting on the resonator. It is convenient to consider the equation of motion in the frequency domain rather than in the time domain in order to look at the response of the resonator to thermal forces. For this we perform the Fourier transformation of equation 3.3:

$$z(\omega) = \chi(\omega)\delta F_{\mathrm{th}}(\omega), \tag{3.5}$$

where $\chi(\omega)$ is the mechanical susceptibility given by:

$$\chi(\omega) = \frac{1}{m_{\mathrm{eff}}(\omega_0^2 - \omega^2 - i\gamma_{\mathrm{m}}\omega)}. \tag{3.6}$$

It describes the response of the displacement $z(\omega)$ to the random fluctuating force $\delta F_{\mathrm{th}}(\omega)$. Usually, the mechanical susceptibility of an oscillator can not be directly measured. However it can be accessed over the mechanical motion $z(t)$ which is translated into a signal $a(t)$ that we measure. The translation happens via the motion transduction scheme that we use to read-out the mechanical motion and therefore depends on the scheme itself. The transduction of z into a is usually linear, $a = \beta z$. Measuring the power spectral density (PSD) $S_{aa}(\omega)$ [1] of the signal $a(t)$ allows us to access the mechanical susceptibility of the oscillator.

The autocorrelation function of the signal $a(t)$ is defined as:

$$C_a(\tau) = \left\langle a^*(t)a(t+\tau)\right\rangle = \int_{-\infty}^{\infty} a^*(t)a(t+\tau)\,dt, \tag{3.7}$$

where $a^*(t)$ is the complex conjugate of $a(t)$. The Wiener-Khinchin theorem relates the autocorrelation function to its PSD as a Fourier transform pair [99]. This means that $S_{aa}(\omega)$ can be obtained from the Fourier transform of its autocorrelation function $C_a(\tau)$ (equation 3.7) given by:

$$\begin{aligned} F\{C_a(\tau)\}(\omega) &= \int_{-\infty}^{+\infty} e^{i\omega\tau}\,d\tau \int_{-\infty}^{+\infty} a^*(t)a(t+\tau)\,dt \\ &= \int_{-\infty}^{+\infty} a^*(t)e^{-i\omega t}\,dt \int_{-\infty}^{+\infty} a(t')e^{i\omega t'}\,dt' \\ &= a(-\omega)\cdot a(\omega) \end{aligned} \tag{3.8}$$

where $t' = t+\tau$ and $dt' = d\tau$ and $a(\omega) = \int_{-\infty}^{+\infty} a(t)e^{i\omega t}\,dt$. Since we consider real

[1] Note that $S_{aa}(\omega)$ is the double-sided PSD, defined over the negative and positive frequency spectrum, whereas $S_a(\omega)$ is the single sided PSD defined only over the positive frequency spectrum. Typically a spectrum analyzer measures the single-sided PSD. For $\omega > 0$ they are related as $S_a(\omega) = 2S_{aa}(\omega)$.

signals $a(t)$, $a(-\omega)=(a(\omega))^*$ and the PSD is simply given by:

$$S_{aa}(\omega)=|a(\omega)|^2. \tag{3.9}$$

The unit of the PSD is [(unit of a)^2/Hz]. This means that in a typical spectral measurement where the signal is in units of V, the unit of the PSD is [V^2/Hz]. Inserting equation 3.5 into equation 3.9 one can relate the spectral density of the force $S_{FF}(\omega)=|\delta F_{\mathrm{th}}(\omega)|^2$ to the spectral density of the displacement $S_{zz}(\omega)$ via the mechanical susceptibility $\chi(\omega)$:

$$S_{zz}(\omega)=\left(\frac{1}{\beta}\right)^2\langle a(\omega)a(-\omega)\rangle=|\chi(\omega)|^2 S_{FF}(\omega). \tag{3.10}$$

This equation expresses the same as equation 3.5, but in experimentally measurable parameters.

With the help of the linear response theory [100], the single sided thermal force noise $S_F^{\mathrm{th}}(\omega)$ of the random fluctuating forces $\delta F_{\mathrm{th}}(t)$ can then be described by:

$$S_F^{\mathrm{th}}(\omega)=-\frac{4k_BT}{\omega}\Im\left(\frac{1}{\chi(\omega)}\right), \tag{3.11}$$

where k_{B} is the Boltzmann constant and T is the temperature. The symbol $\Im$ refers to the imaginary part. In the limit of weak damping, $\gamma_{\mathrm{m}}\ll\omega_0$, this equation can be written as:

$$S_F^{\mathrm{th}}(\omega)=4k_{\mathrm{B}}Tm_{\mathrm{eff}}\gamma_{\mathrm{m}}. \tag{3.12}$$

The thermal force noise is frequency independent, so it is white noise. It only depends on the temperature of the oscillator, its energy dissipation rate γ_{m} and its effective mass m_{eff}. The expression of the thermal force noise is very similar to the expression of the Johnson-Nyquist noise [101] which describes the voltage noise of a resistor. Also the voltage noise of a resistor can be explained with the fluctuation-dissipation theorem. We will discuss more the Johnson-Nyquist noise in chapter 7.

From the thermal force noise spectral density we can get the spectral density of the thermal displacement $S_z^{\mathrm{th}}(\omega)$ using equation 3.12 and equation 3.10:

$$S_z^{\mathrm{th}}(\omega)=\frac{4k_{\mathrm{B}}T\gamma_{\mathrm{m}}}{m_{\mathrm{eff}}[(\omega_0^2-\omega^2)^2+(\gamma_{\mathrm{m}}^2\omega^2)]}. \tag{3.13}$$

The mean energy of the harmonic oscillator in thermal equilibrium is given by the

kinetic energy $\langle T \rangle$ and the potential energy term $\langle U \rangle$:

$$\langle E \rangle = \frac{1}{2} m_{\text{eff}} \langle \dot{z}_{\text{th}}^2 \rangle + \frac{1}{2} k \langle z_{\text{th}}^2 \rangle, \tag{3.14}$$

where $\langle z_{\text{th}}^2 \rangle$ is the variance of displacement. The mean energy of an harmonic oscillator should be also given by:

$$\langle E \rangle = \langle T \rangle + \langle U \rangle = \hbar \omega_0 \left(\frac{1}{2} + \frac{1}{e^{\frac{\hbar \omega_0}{k_B T}} - 1} \right), \tag{3.15}$$

which in the limit for high temperature ($k_B T \gg \hbar \omega_0$) reduces to $\langle E \rangle = \frac{1}{2} k_B T + \frac{1}{2} k_B T$. [2]This approximaton is valid for our case since at temperatures down to 4.2 K the thermal energy is much larger than the phonon energy. For a resonator vibrationg at 100 MHz for example the phonon energy is $\hbar \omega_0 \approx 0.4 \mu$eV whereas the thermal energy is $k_B T \approx 0.36$ meV. From the equipartition theorem we know that in thermal equilibrium the kinetic energy should be equal to the potential energy so:

$$\frac{1}{2} m_{\text{eff}} \langle \dot{z}_{\text{th}}^2 \rangle = \frac{1}{2} k \langle z_{\text{th}}^2 \rangle = \frac{1}{2} k_B T. \tag{3.16}$$

Knowing that $k = m_{\text{eff}} \omega^2$ we then get:

$$\langle z_{\text{th}}^2 \rangle = \frac{k_B T}{m_{\text{eff}} \omega_0^2}. \tag{3.17}$$

Moreover, the variance of displacement can be calculated as the area under the one-sided spectrum of the thermal displacement $S_z^{\text{th}}(\omega)$:

$$\langle z_{\text{th}}^2 \rangle = \int_0^\infty \frac{1}{2\pi} S_z^{\text{th}}(\omega) d\omega = \frac{k_B T}{m_{\text{eff}} \omega_0^2}. \tag{3.18}$$

The temperature of the resonator mode becomes experimentally accessible by looking at the area under the thermal displacement noise peak as schematically shown in Figure 3.1. The temperature dependance of the variance of the displacement also allows to estimate the effective mass m_{eff} of the resonator.

[2] $k_B T \gg \hbar \omega_0$ allows to approximate the term $e^{\frac{\hbar \omega_0}{k_B T}}$ with a taylor expansion $e^{\frac{\hbar \omega_0}{k_B T}} \approx 1 + \frac{\hbar \omega_0}{k_B T} + ...$, with this the mean energy then can be written as: $\langle E \rangle \approx \hbar \omega_0 \left(\frac{1}{2} + \frac{k_B T}{\hbar \omega_0} \right) \approx k_B T$.

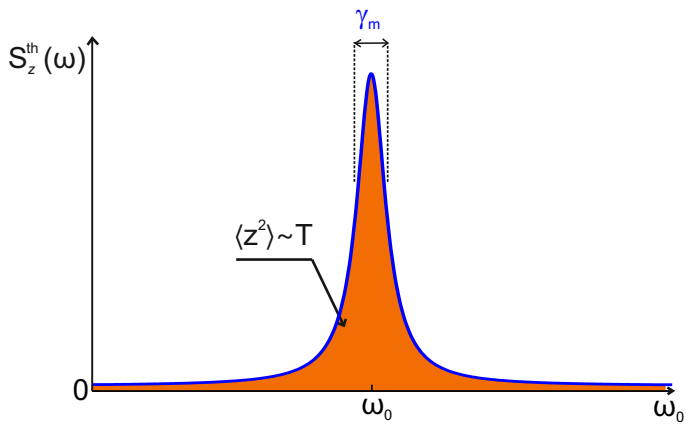

Figure 3.1 – Spectral density of the thermal displacement of a damped harmonic oscillator. The area under the peak is the variance of displacement $\langle z^2 \rangle$. It is proportional to the temperature T at which the mode is thermalized.

3.1.2 Coherently driven harmonic oscillator

We now come back to the equation of motion of a damped harmonic oscillator (equation 3.3). But now $F(t)$ describes an intentional, external driving force, of the form $F_0 \cos(\omega_d t)$, where F_0 is the driving amplitude and ω_d is the driving frequency.

The equation of motion with a coherent drive then becomes:

$$m_{\text{eff}} \ddot{z} + m_{\text{eff}} \gamma_m \dot{z} + k z = F_0 \cos(\omega_d t). \tag{3.19}$$

The response of the amplitude in the frequency domain is then given by:

$$z(\omega_d) = \frac{F_0}{m_{\text{eff}}} \frac{1}{\sqrt{(\omega_0^2 - \omega_d^2)^2 + (\gamma_m \omega_d)^2}}. \tag{3.20}$$

and the phase response in the frequency domain by

$$\phi(\omega_d) = \arctan\left(\frac{\gamma_m \omega_0}{(\omega_0^2 - \omega_d^2)} \right). \tag{3.21}$$

The amplitude and phase response described by equation 3.20 and 3.21 respectively can be seen in Figure 3.2. We see that the amplitude signal is maximum on resonance (so for $\omega_d = \omega_0$), whereas on resonance the mechanical motion is $\pi/2$ out of phase with the drive ($\phi(\omega_0) = \pi/2$).

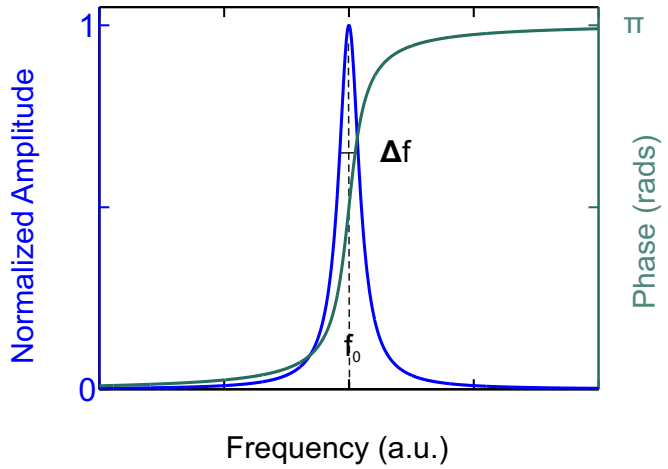

Figure 3.2 – Amplitude $z(\omega_\mathrm{d})$ and phase $\phi(\omega_\mathrm{d})$ response of a driven damped harmonic oscillator as a function of the driving frequency ω_d. The amplitude has its maximum at the resonance frequency f_0. Here the phase goes through a 180° shift. The linear damping rate γ_m is given by the line width of the squared normalized amplitude response at half maximum.

3.2 Nonlinear oscillator

The motion of a nanomechanical resonator can be described by the harmonic oscillator model as long as the restoring force scales linearly with the displacement. This is only valid for small displacement amplitudes. Once the nanomechanical resonator is driven into large amplitudes of motion, nonlinearities start to play an important role. They can appear in the form of a nonlinear restoring force which changes the resonance frequency and a nonlinear damping term which modifies the damping rate of the resonator. In the following we describe in more detail the equation of motion for a nonlinear oscillator with and without a nonlinear damping term. We also give an overview on the origin of nonlinearities.

3.2.1 Oscillator with linear and nonlinear restoring force: Duffing oscillator

A nanomechanical resonator can be described as Duffing oscillator when the large amplitude of motion results in a nonlinear restoring force. In this case the equation of motion has an additional term compared to the equation of motion of the harmonic oscillator. This term describes the nonlinear restoring force. It is proportional to the

cubic displacement of the resonator. The equation of motion then becomes:

$$m_{\text{eff}}\ddot{z} + m_{\text{eff}}\gamma_{\text{m}}\dot{z} + kz + \alpha z^3 = F_0\cos(\omega_{\text{d}}t), \tag{3.22}$$

where α is the Duffing nonlinear constant. This equation can be solved for the limit of small oscillations [102]. The amplitude of motion is then given by:

$$z(\omega_{\text{d}}) \approx \frac{F_0}{m_{\text{eff}}} \frac{1}{\sqrt{(\omega_0^2 + \frac{3}{4}\alpha z(\omega_{\text{d}})^2 - \omega_{\text{d}}^2)^2 + (\gamma_{\text{m}}\omega_{\text{d}})^2}} \tag{3.23}$$

and the phase is:

$$\phi(\omega_{\text{d}}) \approx \arctan\left(\frac{\omega_{\text{d}}\omega_0}{\frac{\omega_0}{\gamma_{\text{m}}}(\omega_0^2 + \frac{3}{4}\alpha z(\omega_{\text{d}})^2 - \omega_{\text{d}}^2)}\right). \tag{3.24}$$

Equation (3.23) has the form of a modified Lorentzian. Above a critical driving amplitude (where the term proportional to the cubic displacement is no longer negligible), this equation has two stable solutions and one unstable solution. This results in a bistable response of amplitude and phase near the resonance frequency and a hysteresis. Hysteresis means that the response depends on the direction in which the driving frequency is swept. The amplitude responses below and above this critical driving are sketched in Figure 3.3 . For low driving, the amplitude response is described by a simple Lorentzian function. For high driving, the resonance frequency shifts to higher or lower values depending on the sign of duffing nonlinearity α. A shift to higher resonance frequencies with increasing amplitude is the result of an increase (decrease) in the stiffness of the resonator.

The nonlinear response of the dynamics of an oscillator, as described by the previously derived equations, can be the result of different mechanisms. The most common mechanisms are geometrical effects and nonlinear external potentials [102]. Nonlinearities limit the dynamic range of a resonator, which defines the signal to noise ratio at the onset of nonlinearity.

3.2.2 Duffing oscillator with nonlinear damping

In a regime where damping depends on the amplitude of motion, nonlinearities become apparent in the damping as well. In the equation of motion this nonlinear damping, also known as a non-conservative nonlinear process, can be taken into account by a nonlinear dissipative force term $F = \eta z^2 \dot{z}$. The equation of motion of a Duffing oscillator with nonlinear damping can then be described by the following

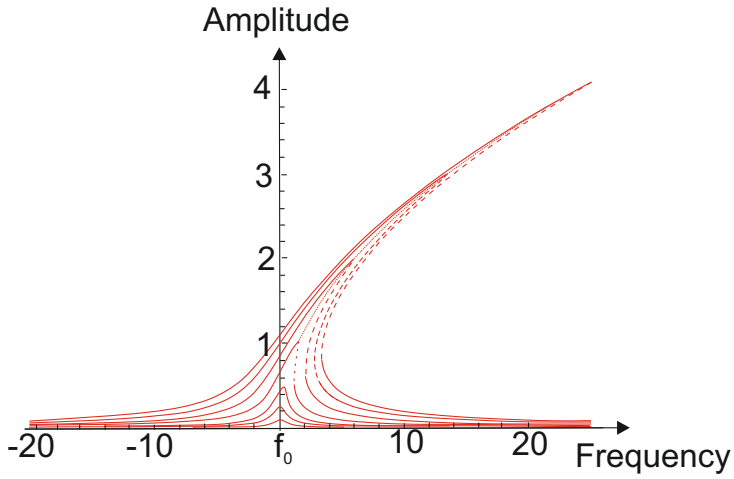

Figure 3.3 – Amplitude response of a Duffing oscillator for different driving amplitudes. Figure adapted from [102].

equation of motion [102]:

$$m_{\text{eff}}\ddot{z} + m_{\text{eff}}\gamma_{\text{m}}\dot{z} + kz + \alpha z^3 + \eta z^2\dot{z} = F_0\cos(\omega_{\text{d}}t), \tag{3.25}$$

where η is a dimensionless coefficient, which describes the nonlinear damping. The solution of this equation for the amplitude is:

$$z(\omega_{\text{d}}) \approx \frac{F_0}{2m_{\text{eff}}\omega_0^2} \frac{1}{\sqrt{\left(\frac{\omega_{\text{d}}-\omega_0}{\omega_0} - \frac{3\alpha}{8m_{\text{eff}}\omega_{\text{d}})^2}z(\omega_{\text{d}})^2\right)^2 + \left(\frac{\gamma_{\text{m}}}{2\omega_0} + \frac{\eta}{8m_{\text{eff}}\omega_0}z(\omega_{\text{d}})^2\right)^2}}, \tag{3.26}$$

and for the phase:

$$\phi(\omega_{\text{d}}) \approx \arctan\left(\frac{\frac{\gamma_{\text{m}}}{2} + \frac{\eta}{8}z(\omega_{\text{d}})^2}{m_{\text{eff}}(\omega_{\text{d}}-\omega_0) - \frac{3\alpha}{8\omega_0}z(\omega_{\text{d}})^2}\right). \tag{3.27}$$

For a Duffing resonator with nonlinear damping ($\eta > 0$), the normalized amplitude of the mechanical vibration decreases with increasing driving force and increasing amplitude of motion. The normalized amplitude can be obtained by dividing the peak amplitude z_{peak} by the the amplitude of the driving force F_0. For a Duffing resonator without nonlinear damping, the normalized amplitude remains constant when increasing the driving force.

3.3 Beam mechanics

Here we relate the dynamic properties of a mechanical resonator which can be described by a harmonic oscillator to a specific resonator type and its geometrical and mechanical properties. Beam mechanics allows to estimate the resonance frequency and the effective mass of a resonator if we know its dimensions and mechanical properties such as mass density, Youngs modulus and built-in tension. Conversely it allows to extract the effective mass (m_{eff}) of the device and the built-in tension if we look at the response of the resonance frequency to an external electrostatic field. Many resonator geometries can be reduced to a beam geometry. The resonators we study to a double clamped beam geometry. We therefore want to develop in the following section the mechanics of a double clamped beam which we then extend to the model of a double clamped beam exposed to a uniformly distributed electrostatic force. We finish with a short summary of the effective mass of different resonator modes.

3.3.1 Double clamped beam

Carbon nanotube resonators can be modeled as a double clamped beam with a tubular cross section. For simplicity, we simplify the problem by considering a rod (see Figure 3.4). The continuum model we present considers flexural modes of vibration. This means that displacement takes place in z-direction and forces are applied in z-direction. The motion of any resonator can be described by a displacement function $\xi(x,t)$. This displacement function is the product of the function describing the motion $z(t)$ with a function describing the mode shape $u(x)$. The total displacement function can then be described by the sum of the displacement functions of all n modes of the resonator:

$$\xi(x,t)=\sum_n \xi_n(x,t)=\sum_n z_n(t)u_n(x), \tag{3.28}$$

The motion z_n of each resonator mode is well described by the equation of the damped harmonic oscillator. The mode shape $u(x)$ is normalized such that the maximum displacement $|u(x)|$ is 1. In Continuum mechanics, we look at the total elastic potential energy stored in a beam. The elastic energy of a beam is due to bending and stretching. The total elastic energy can be written as:

$$U_{\text{elastic}}=\frac{1}{2}\int_0^L\left[EI\xi''(x,t)^2+\left(T_0+\int_0^L\frac{EA}{2L}\xi'(x,t)^2dx\right)\xi'(x,t)^2\right]dx, \tag{3.29}$$

where L is the length of the resonator, E the Youngs modulus, $I = \frac{\pi r^4}{4}$ the moment of inertia with r being the radius of the nanotube, $T_0 = A\sigma$ the built-in tension with σ being the stress and A the uniform circular cross sectional area, $T_{\text{tot}} = T_0 + \int_0^L \frac{EA}{2L}\xi'(x,t)^2 dx$ the total tension, and ξ' the derivation of ξ with respect to x. The first term in the integral of equation 3.29 accounts for the flexural rigidity and the 2nd term for extensional rigidity.

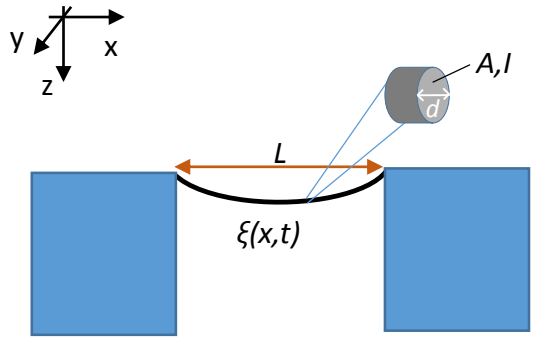

Figure 3.4 – Schematics of a double clamped rod. Deflection happens in z direction. $\xi(x,t)$ describes the displacement function. A is the cross section of the rod, I the momentum of inertia, d its diameter and L its total length. The elastic energy is given by integrating a small element dx over L.

The equation of motion of a rod is then calculated using the Euler-Bernoulli beam theory (where $L \gg d$). It is given by the differential equation that minimizes the total beam energy. With the total beam energy given by:

$$U_{\text{tot}} = U_{\text{elastic}} + U_{\text{kin}} = U_{\text{elastic}} + \frac{1}{2}\int_0^L (\rho A \dot{\xi}(x,t))^2 dx, \tag{3.30}$$

where ρ is the uniform mass density. The equation of motion for a free rod (without external force) then becomes:

$$\rho A \ddot{\xi}(x,t) - T_{\text{tot}}\xi(x,t)'' - EI\xi(x,t)'''' = 0. \tag{3.31}$$

This equation of motion can be easily solved for two limiting cases. The first limiting case considers a mechanical rod where the tension is much smaller than the bending rigidity ($T_{\text{tot}} \ll EI/L^2$). The 2$^{\text{nd}}$ term in equation 3.31 can then be neglected. The equation for the mode shape u_n can be derived using the Ansatz $z_n(t) = c_n \cos(\omega_n) +$

$d_n \sin(\omega_n)$, where c_n and d_n are two mode dependent constants:

$$u_n(x)'''' - \frac{\alpha_n^4}{L} u_n(x) = 0, \tag{3.32}$$

where $\alpha_n = L(\rho A \omega_n / EI)^{1/4}$ is a dimensional parameter which depends on the resonance frequency of the specific mode n. This differential equation can be solved with the boundary conditions of a double clamped rod ($u_n(0)=0$, $u_n'(0)=0$, $u_n(L)=0$ and $u_n'(L)=0$). It means that the ends of the rod are fixed. The mode shape is found to have the following form:

$$u_n(x) = A\left[\cosh\left(\frac{\alpha_n x}{L}\right) - \cos\left(\frac{\alpha_n x}{L}\right)\right] - B\left[\sinh\left(\frac{\alpha_n x}{L}\right) - \sin\left(\frac{\alpha_n x}{L}\right)\right], \tag{3.33}$$

where A and B are defined using the boundary conditions and fulfilling the normalization condition for the maximum displacement ($|u(x)|=1$). Figure 3.5(a) shows the first three normalized modes for a rod in the bending regime. The resonance frequency of the n$^{\text{th}}$ mechanical mode is given by [103]:

$$f_n = \frac{\alpha_n^2}{2\pi L^2} \sqrt{\frac{EI}{\rho A}}, \tag{3.34}$$

where $\alpha_1 = 4.73$, $\alpha_2 = 7.85$ and $\alpha_3 = 10.1$.

For a double clamped rod in the tension limit ($T_{\text{tot}} \gg EI/L^2$), the term coming from the bending rigidity can be neglected in equation 3.31. The nanotube is then described as a string. The equation of motion for the modeshape then reduces to:

$$u_n(x)'' - \frac{\rho \omega_n^2}{\sigma} u_n(x) = 0, \tag{3.35}$$

This differential equation is solved using the boundary conditions $u_n(0)=0$ and $u_n(L)=0$. The solution for the modeshape is found to be:

$$u_n(x) = \sin\left(\frac{n\pi x}{L}\right). \tag{3.36}$$

The first three normalized modes for a rod in the tension regime are shown in Figure 3.5(b). The resonance frequency of the n$^{\text{th}}$ mode is then given by [103]:

$$f_n = \frac{n}{2L} \sqrt{\frac{T}{\rho A}}, \tag{3.37}$$

where $n = 1,2,3...$ gives the mode number.

Regardless whether the nanotube behaves like a slacky (tension negligible) or rather like a tensioned rod, its resonance frequency always increases with decreasing device length. We also see the resonance frequency scales with $1/\sqrt{\rho}$. Carbon nanotubes are therefore very good candidates for achieving high frequency nanoelectromechanical resonators.

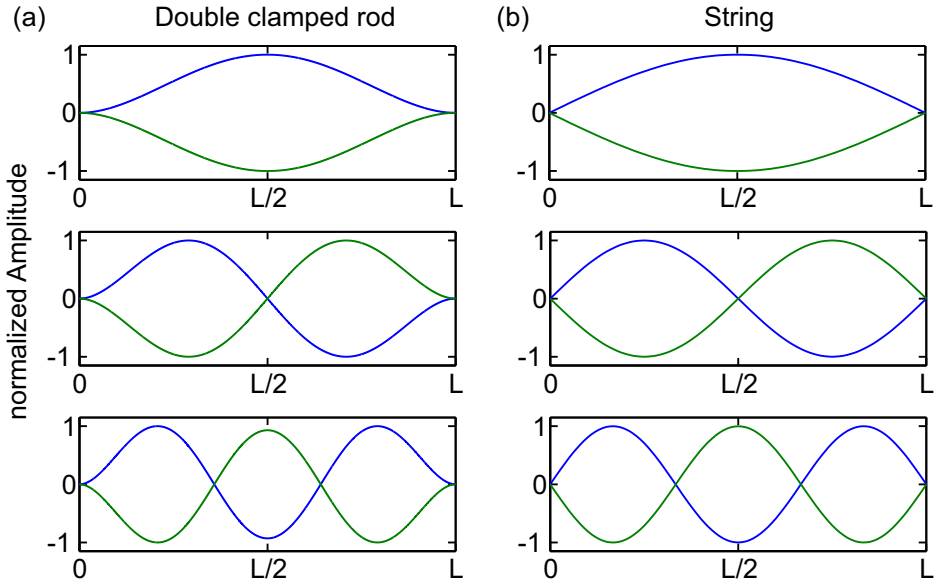

Figure 3.5 – Mode shapes of a double clamped rod. (a)First three modes for a rod in the bending limit. (b) first three modes of a rod in the tension limit, here it is also called string. Adapted from [103].

3.3.2 Double clamped membrane

Double clamped graphene resonators under tension can be modeled as the two dimensional analog of a carbon nanotube string. Basically, a graphene resonator can be described as a 2-dimensional membrane, where we can neglect the flexural rigidity. In a one-dimensional approximation we can therefore describe its resonance frequency by the same equation as already introduced for a one-dimensional string (3.37).

3.3.3 Effective mass of carbon nanotubes and graphene resonators

The mode shape for the different type of resonator geometries allows us to derive their corresponding effective mass. With the effective mass, we obtain a correction term needed to describe the motion of any type of resonator as an harmonic oscillator. We can write the total potential energy of the nth mode of an harmonic oscillator as [103]:

$$U_{\text{potential}} = \frac{1}{2}\omega_n^2 |z_n(t)|^2 \int_0^L \rho A |u_n(x)|^2 dx = \frac{1}{2}\omega_n^2 |z_n(t)|^2 m_{\text{eff},n}, \tag{3.38}$$

where the effective mass is [103]:

$$m_{\text{eff},n} = \int_0^L \rho A |u_n|^2 dx = m\frac{1}{L}\int_0^L |u_n(x)|^2 dx, \tag{3.39}$$

where m is the mass of the resonator. We can then estimate the effective mass of the fundamental mode of a resonator in the bending regime using the mode shape defined in equation 3.33 [103]:

$$m_{\text{eff},1} = m\frac{1}{L}\int_0^L |u_n(x)|^2 dx = m \cdot 0.3965. \tag{3.40}$$

For higher modes we get $\frac{m_{\text{eff},2}}{m} = 0.4390$ and $\frac{m_{\text{eff},3}}{m} = 0.4371$. For $n \geq 4$ it saturates to $\frac{m_{\text{eff},3}}{m} = 0.4372$. The effective mass for a carbon nanotube resonator in the bending regime is therefore slightly mode dependent and we can calculate it knowing the mode dependent correction factor.

For a resonator in the tension limit that describes a string like carbon nanotube or a double clamped graphene resonator we can calculate the effective mass of the nth mode in the same manner using the mode shape equation 3.36 [103]:

$$m_{\text{eff},n} = m\frac{1}{L}\int_0^L |u_n(x)|^2 dx = \frac{m}{2}, \tag{3.41}$$

here the factor is mode independent. The result for all modes is 1/2.

3.3.4 External tension

Now that we know the effective masses of resonators under tension such as strings and membranes we can use a simple model to understand how an electrostatic force

affects the resonance frequency of these resonators. We can look at this problem in terms of the spring constant. The application of a voltage bias on the gate electrode will deflect the resonator towards the gate and will therefore result in a change in the spring constant k. In the harmonic oscillator model, this means that we describe the restoring force $F = -k_{\text{eff}} z(t)$ with an effective spring constant k_{eff}. The electrostatic force is given by $F_{\text{el}} = \frac{1}{2} C_{\text{g}}' V_{\text{g}}^2$, where C_{g}' is the derivative of the resonator-gate capacitance C_{g} with respect to z. With this electrostatic force the spring constant then becomes:

$$k_{\text{eff}} = k - \frac{\partial F_{\text{el}}}{\partial z} = k - \frac{1}{2} C_{\text{g}}'' V_{\text{g}}^2 \tag{3.42}$$

where $k = m_{\text{eff}} \omega^2$. Here, we get the term $\frac{1}{2} C_{\text{g}}'' V_{\text{g}}^2$ by expanding the capacitance to $C_{\text{g}} = C + C' z$. It describes the softening of the spring constant due to the nonlinear electrostatic force. If we express this softening in terms of the resonance frequency, we get [33]:

$$\begin{aligned} f(V_{\text{g}}) &= \frac{1}{2\pi} \sqrt{\frac{k_{\text{eff}}}{m_{\text{eff}}}} \\ &= f_0 \sqrt{1 - \frac{1}{8\pi^2 f_0^2 m_{\text{eff}}} C_{\text{g}}'' V_{\text{g}}^2} \\ &\approx f_0 \left[1 - \frac{1}{16\pi^2 f_0^2 m_{\text{eff}}} C_{\text{g}}'' V_{\text{g}}^2 \right] \\ &\approx f_0 - f_0 \frac{L}{4\pi^2 T_0} C_{\text{g}}'' V_{\text{g}}^2, \end{aligned} \tag{3.43}$$

where the approximation is a taylor series of the square root. Here $f_0 = \frac{1}{2L} \sqrt{\frac{T_0}{\rho A}} = \frac{1}{2} \sqrt{\frac{T_0}{m_{\text{eff}} L}}$ is the resonance frequency of the mode defined only by the built-in tension T_0. Any additional strain induced through the stretching of the device by the deflection towards the gate is neglected in this model.

3.3.5 Summary

A resonator can be described in the bending or in the tension regime depending weather the restoring force is dominated by the bending rigidity or by the tension. The tension can be tuned via the electrostatic field and therefore even a resonator without built-in tension can be tuned into the tension dominated regime. In the case of nanotube and graphene resonators the bending rigidity is extremely small and easily overcome by either the in-built or externally applied tension. For this

reason these devices can typically be modelled as a 1-dimensional string. The built-in tension of the device is defined during the fabrication.

4 Actuation and detection techniques of mechanical resonators

In this chapter we first discuss in detail the techniques used throughout this thesis to actuate and detect the mechanical motion of graphene and carbon nanotubes. The techniques we focus on are: electrical actuation and detection based on electrical frequency mixing (Two-Source mixing and Frequency modulation mixing). After a description of these electrical techniques, we lay out their advantages and disadvantages. We finish the chapter with a short overview on other widely used techniques that were not part of this thesis but have lead to important contributions within the scientific community: Crosscorrelation, rectification technique, direct electrical read-out, and optical detection.

4.1 Introduction

Key to recent improvements in force and mass sensitivities achieved with nanomechanical resonators is an efficient transduction of the mechanical motion into a detectable electrical or optical signal. Especially for carbon nanotubes and graphene this is a major challenge, since they are small their motion is transduced into minuscule electrical and optical signals that have to be extracted from a large background noise. Various techniques have been implemented for actuating and for detecting the motion of different nanomechanical resonators, among them optical [104], magnetomotive [105, 106], piezoresistive [107], piezoelectric [108] and capacitive (electrostatic) [24] techniques. Here, we discuss the capacitive techniques which are the most suitable and widely used techniques for low-dimensional resonators such as carbon nanotubes and graphene.

4.2 Electrical actuation and detection of mechanical resonators

4.2.1 Electrostatic actuation

Electrostatic actuation of the mechanical resonator is based on a capacitive force between two conducting elements. It can be understood by looking at a transistor like geometry where one conductor is formed by the carbon nanotube or the graphene and the other one by the underlying gate electrode. The carbon nanotube or the graphene is suspended over the gate electrode and can vibrate freely. It is electrically contacted by a source and a drain electrode. The transistor-like geometry is sketched in Figure 4.1. The carbon nanotube or the graphene sheet together with the underlying gate electrode form a capacitor with a capacitance C_g. Therefore, applying a DC voltage V_g^{DC} to the gate will charge the resonator ($q = C_g V_g$) and lead to an electrostatic force $F_{el}^{DC} = \frac{1}{2} C_g' V_g^{DC}$ that statically deflects the resonator towards the gate electrode (in z direction, as sketched in Figure 3.4). Here, C_g' is the derivative of the capacitance C_g with respect to z. Introducing an additional AC voltage $\tilde{V}_g^{\omega} = \tilde{V}_g \cos(\omega t)$ at the gate electrode, sets the resonator into motion around its new equilibrium position defined by V_g^{DC}. The electrostatic force acting on the resonator then becomes an oscillating force:

$$F_{el} = \frac{1}{2} C_g' V_g^2 = \frac{1}{2} C_g' (V_g^{DC} + \tilde{V}_g^{\omega})^2. \tag{4.1}$$

Neglecting the term quadratic in $(\tilde{V}_g^{\omega})^2$, this then simplifies to an electrostatic part $F_{el}^{DC} = \frac{1}{2} C_g' (V_g^{DC})^2$ and an oscillating part $\tilde{F}_{el} \approx C_g' V_g^{DC} \tilde{V}_g^{\omega}$ of the force. The DC-term does not only change the static deflection of the resonator but also the tension. The resonator has its largest amplitude of motion once the frequency ω of the oscillating force coincides with the mechanical resonance frequency ω_0 of the resonator. Electrostatic actuation is commonly used together with electrical and optical detection of the motion. The electrical detection techniques of the mechanical motion are explained and mathematically described in the following section.

4.2.2 Electrical detection

All electrical readout techniques are based on the transistor-like geometry which allows the motion of the resonator to couple to its own charge via the field-effect. Carbon nanotubes and graphene show a typical field effect: their charge and hence their conductance is tunable via an external electric field. The electric field, generated by

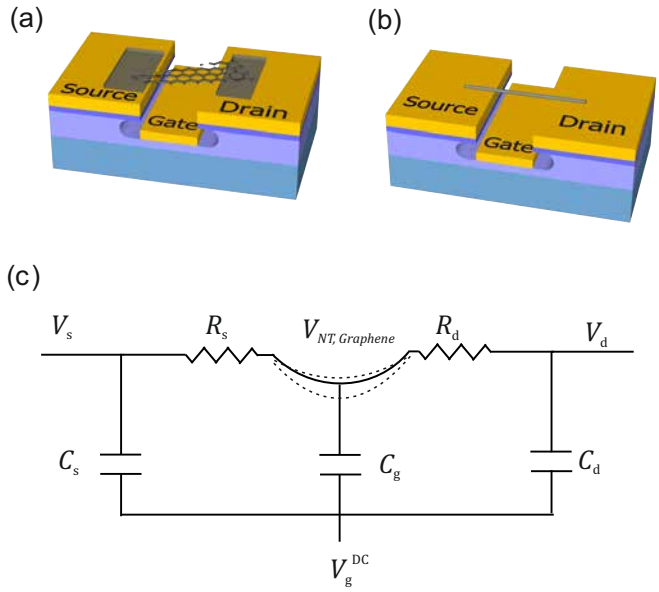

Figure 4.1 – Graphene and carbon nanotube transistor configuration and equivalent circuit diagram.(a) Schematic of graphene transistor geometry with source, drain and gate electrode. (b) Schematic of carbon nanotube transistor. (c) Equivalent circuit diagram for both geometries. The gate capacitance C_g is needed for actuation and detection. C_s and C_d are parasitic capacitances. They can be reduced with a local gate configuration as in (a) and (b).

the gate voltage, tunes the distance between the gate and the resonator. A modulation of the distance z (or modulation of the capacitance $\tilde{C}_g$) as well as a modulation of the gate voltage $\tilde{V}_g^{\omega}$ leads to a modulation in the charge $\tilde{q} = \tilde{C}_g(\omega)V_g^{DC} + C_g\tilde{V}_g^{\omega}$. Here, the charge modulation via the capacitance is induced by the mechanical motion, whereas the charge modulation via the modulated gate voltage has a purely electrical origin. A modulation in the charge results in modulation in the conductance $\tilde{G}$ of the carbon nanotube or the graphene. The total conductance modulation then also originates from a distance $z(\omega)$ and voltage modulation $\tilde{V}_g^{\omega}$ and can be described by the following equation:

$$G(V_g, z) = G(V_g^{DC}) + \tilde{G} = G(V_g^{DC}) + \frac{dG}{dV_g^{DC}}\tilde{V}_g^{\omega} + \frac{dG}{dz}z(\omega). \tag{4.2}$$

The conductance change with the deflection z can be described by $\frac{dG}{dz} = \frac{dG}{dq}\frac{dq}{dz}$. Together with $\frac{dG}{dq} = \frac{dG}{dV_g^{DC}}\frac{dV_g^{DC}}{dq} = \frac{dG}{dV_g^{DC}}\frac{1}{C_g}$ and $\frac{dq}{dz} = \frac{\delta(C_g V_{gDC})}{\delta z} = V_g^{DC}C_g'$ with $C_g' = dC_g/dz$, the modulated part of the conductance $\tilde{G}^{\omega}$ then simplifies to the following equation:

$$\tilde{G} = \frac{dG}{dV_g^{DC}} \tilde{V}_g^{\omega} + \frac{dG}{dV_g^{DC}} \frac{C_g'}{C_g} z(\omega) V_g^{DC}. \tag{4.3}$$

The total modulated conductance is proportional to the amplitude of motion of the resonator $z(\omega)$ described in chapter 3, equation 3.20 and results in a total current flowing through the resonator expressed by the following equation:

$$I_{tot} = V_{SD}(G(V_g^{DC}) + \tilde{G}) = V_{SD} G(V_g^{DC}) + V_{SD} \frac{dG}{dV_g^{DC}} \tilde{V}_g^{\omega} + V_{SD} \frac{dG}{dV_g^{DC}} \frac{C_g'}{C_g} z(\omega) V_g^{DC} \tag{4.4}$$

The first two terms are purely electrical, whereas the last term is due to the mechanical motion of the resonator. If the voltage is modulated at the resonance frequency of the resonator, then the conductance modulation is largest and results in a peak in the current signal. The amplitude of this electromechanical signal depends on the transconductance $\frac{dG}{dV_g^{DC}}$ of the resonator. Typically, high transconductance is obtained in devices with a large conductance. The large transconductance results in a significantly high electromechanical signal and makes electrical detection very suitable for these type of resonators. Carbon nanotubes and graphene resonators typically vibrate in the MHz regime. For the signal read-out in real time, this would mean to detect the electromechanical current at MHz frequencies also. This, however, is very challenging due to several reasons. Signal levels are rather small because we are typically dealing with high resistive devices (1-100 kΩ). Additionally, the device (see Figure 4.1) has a limited readout bandwidth. Assuming the device has a resistance of 40 kΩ that is symmetrically split between the source and the drain contact. Then the resistance at the drain is $R_d = 20\,k\Omega$. At the drain electrode, where the signal is read-out, the resistance R_d and the parasitic capacitance C_d of the drain electrode form a lowpass filter with the following cutoff frequency:

$$f_{cut-off} = \frac{1}{2\pi R_d C_d} \tag{4.5}$$

In a measurement circuit the capacitance limiting the read-out bandwidth is not only given by the parasitic capacitance C_d of the device, but also by the capacitance of the wire bond and the capacitance of the cable used to read-out the signal. Taking into account the capacitance of the cable (100 pF) only, the cutoff frequency of the measurement circuit then becomes 80 kHz. The parasitic capacitance between the drain electrode and the gate electrode and the parasitic capacitance of the wire bond lower the cut-off frequency of 80 kHz even further.

4.2.2.1 Standard frequency mixing techniques

All frequency mixing techniques are based on downconversion of a high frequency current signal to a frequency below $f_{\text{cut-off}}$ of the corresponding device configuration. These techniques have been experimentally demonstrated for the electrical read-out of the mechanical motion of a nanomechanical resonators coupled to a single electron transistor [20], and for carbon nanotube [40] and graphene resonators [41]. The techniques exploit the nonzero transconductance of carbon nanotube and graphene to use them as the active mixing element of the different modulated voltages. In the following sections we explain the different mixing techniques in more detail.

Two-Source mixing technique

The first experimental demonstrations of the electrical read-out of nanomechanical motion have used the two-source mixing technique [20, 40, 41]. The read-out scheme is illustrated in Figure 4.2(a). The two-source technique allows to measure the mechanical resonance by looking at the current modulation flowing through the resonator which carries the information of the mechanical properties. The information of the mechanical amplitude can be transferred into a low frequency signal by applying an ac voltage to the source of the device (apart from the ac voltage at the gate) at a slightly different frequency $\omega+\Delta\omega$ compared to $\tilde{V}_{\text{g}}^{\omega}$. The current flowing through the device then depends on the conductance modulation $\tilde{G}^{\omega}=\tilde{G}\cos(\omega t)$ and the ac voltage at the source $\tilde{V}_{\text{SD}}^{\omega}=\tilde{V}_{\text{SD}}\cos((\omega+\Delta\omega)t)$. It is defined by:

$$I_{\text{tot}}=V_{\text{SD}}G=(G(V_{\text{g}}^{\text{DC}})+\tilde{G}^{\omega})\tilde{V}_{\text{SD}}^{\omega+\Delta\omega}=G(V_{\text{g}}^{\text{DC}})\tilde{V}_{\text{SD}}^{\omega+\Delta\omega}+\tilde{G}^{\omega}\tilde{V}_{\text{SD}}^{\omega+\Delta\omega}. \tag{4.6}$$

The first term describes a current with no information on the mechanics. The second term mixes terms of two different frequencies and contains the signal of interest. It can be expanded and simplified in the following way:

$$\tilde{G}^{\omega}\tilde{V}_{\text{SD}}^{\omega+\Delta\omega}=\tilde{G}\cos(\omega t)\tilde{V}_{\text{SD}}\cos((\omega+\Delta\omega)t)=\frac{1}{2}\tilde{V}_{\text{SD}}\tilde{G}(\cos(2\omega t)+\cos(\Delta\omega t)). \tag{4.7}$$

The mixing results in two different mixing terms. One at the high frequency 2ω, and one at a low frequency $\Delta\omega$. The mechanical information can therefore be read-out at measuring the amplitude of the current at low frequency $\Delta\omega$. The current amplitude at $\Delta\omega$, with the help of equation 4.3, is given by:

$$I^{\Delta\omega}=\frac{1}{2}\tilde{G}\,\tilde{V}_{\text{SD}}=\frac{1}{2}\tilde{V}_{\text{SD}}\frac{dG}{dV_{\text{g}}^{\text{DC}}}\left(\tilde{V}_{\text{g}}+\frac{C_{\text{g}}'}{C_{\text{g}}}z(\omega)V_{\text{g}}^{\text{DC}}\right) \tag{4.8}$$

The first term of this expression is a purely electrical background signal. The second

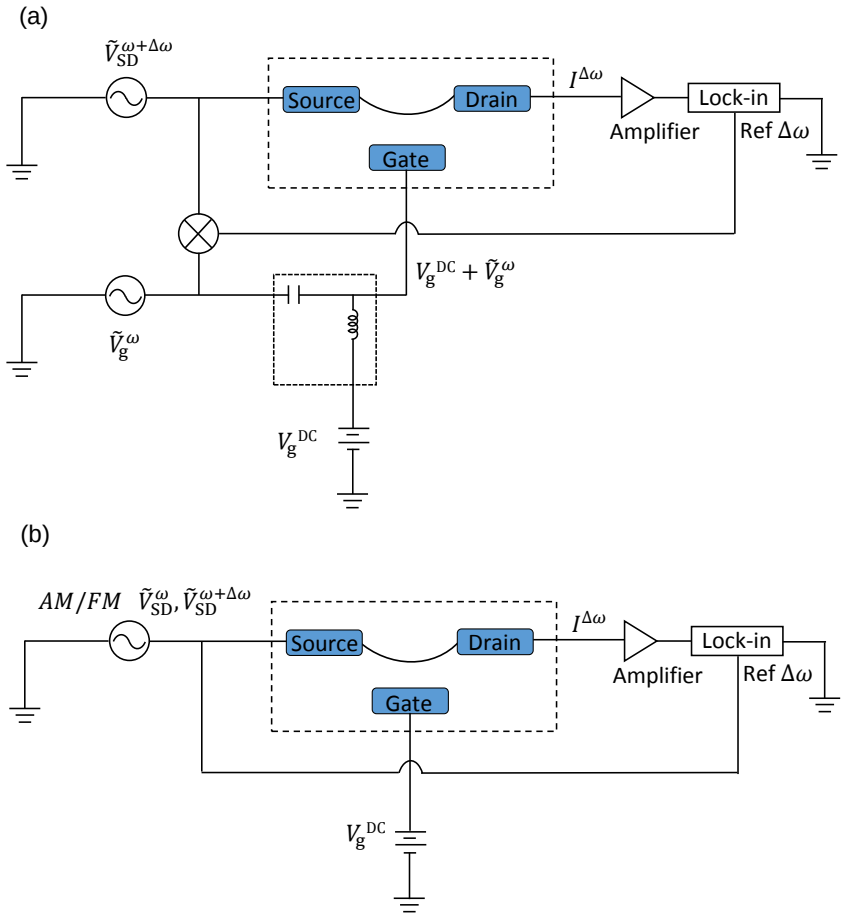

Figure 4.2 – (a) Two Source read-out schematic. (b) AM/FM read-out schematic.

term is the electromechanical term of interest that results in a current signal directly proportional to the amplitude of motion z. The two-source mixing technique is therefore a mechanical motion transduction scheme where the measured signal is linearly related to the mechanical amplitude of motion as introduced in chapter 3. The factor that translates z into a current is given by $\beta = \frac{1}{2}\tilde{V}_{SD}\frac{dG}{dV_g^{DC}}\frac{C_g'}{C_g}V_g^{DC}$. Noise in any parameter that defines β as well as noise affecting the mechanical response z itself therefore translates into noise in the measured current signal. Noise in the voltage amplitude $\tilde{V}_{SD}$ for example results in noise in the measured mixing current. Noise in V_g^{DC} instead does not contribute to noise in β only but also affects the mechanical response directly through electrostatically induced changes in the spring

constant. How different sources of noise affect the mass sensing performance of nanomechanical resonators will be discussed in more detail in the next chapter and experimental results on the limitations are found in 6.4.4, 7.4 7.5 and A.

Amplitude Modulation

Downmixing of the mechanical vibrations into a low frequency current can also be achieved using amplitude modulation and has been previously used for the read-out of carbon nanotube resonators [58]. Here, an amplitude modulated voltage applied at the source of the device is sufficient to provide both, the driving $\tilde{V}_{\mathrm{SD}}^{\omega}$ and the $V_{\mathrm{SD}}^{\omega+\delta\omega}$ mixing voltage. An ac voltage at the source together with a DC voltage at the gate is equivalent to an effective oscillating voltage at the gate ($V_{\mathrm{g}}^{\mathrm{DC}}-\frac{1}{2}\tilde{V}_{\mathrm{SD}}^{\omega}$,) the factor $1/2$ comes from the contact resistance (Figure 4.2 (b)). It therefore also results in the conductance modulation. An amplitude modulation at $\Delta\omega$ of any ac voltage $A\cos(\omega t)$ with amplitude A is defined as the following:

$$\begin{aligned} V_{\mathrm{AM}} &= (1+m\cos(\Delta\omega t))A\cos(\omega t) \\ &= A\cos(\omega t)+\frac{Am}{2}(\cos((\omega+\Delta\omega)t)+\cos((\omega-\Delta\omega)t)) \end{aligned} \tag{4.9}$$

where m is the strength of the modulation. The AM modulated voltage combines the driving and the mixing voltages at different frequencies needed for the downmixing read-out. It can be seen as a two-source downmixing scheme with the following voltages on the gate and the source:

$$\begin{aligned} \tilde{V}_{\mathrm{g}}^{\omega} &= \frac{1}{2}\tilde{V}_{\mathrm{SD}}\cos(\omega t) \\ \tilde{V}_{\mathrm{SD}}^{\omega+\Delta\omega} &= \tilde{V}_{\mathrm{SD}}\, m\cos((\omega+\Delta\omega)t). \end{aligned} \tag{4.10}$$

The current amplitude measured at $\Delta\omega$ at the drain of the device is similar to 4.8 given by:

$$I_{\mathrm{AM}}^{\Delta\omega} = \frac{m}{2}\tilde{V}_{\mathrm{SD}}\frac{dG}{dV_{\mathrm{g}}^{\mathrm{DC}}}\left(\tilde{V}_{\mathrm{SD}}+\frac{C_{\mathrm{g}}'}{C_{\mathrm{g}}}z(\omega)V_{\mathrm{g}}^{\mathrm{DC}}\right) \tag{4.11}$$

Frequency-Modulation

Another way of implementing the read-out with a single source used for the mixing is the frequency modulation (FM) mixing (see Figure 4.2(b)). It has been used first for the read-out of carbon nanotube resonators [58] and later on for graphene resonators as well also here in the Bachtold group [33, 60]. Here, instead of an amplitude modu-

lated voltage it is a frequency modulated voltage that is applied to the source of the device. At the gate, again a DC voltage is sufficient. The read-out scheme is sketched in Figure 4.2(b) also. Frequency modulation at $\Delta\omega$ of any ac voltage $A\cos(\omega t)$, with amplitude A is defined by:

$$V_{\mathrm{FM}} = A\cos(\omega t + (\omega_{\Delta}/\Delta\omega)\sin(\Delta\omega t)), \tag{4.12}$$

where ω is the driving frequency also called carrier frequency and ω_{Δ} the frequency deviation. This results in a mixing current that can be read-out at the frequency $\Delta\omega$ at the drain of the nanotube given by:

$$I_{\mathrm{FM}}^{\Delta\omega} = \frac{1}{2} V_{\mathrm{g}}^{\mathrm{DC}} \frac{dG}{dV_{\mathrm{g}}^{\mathrm{DC}}} \frac{C_{\mathrm{g}}'}{C_{\mathrm{g}}} \tilde{V}_{\mathrm{SD}} \omega_{\Delta} \frac{\partial}{\partial\omega} Re(z(\omega)), \tag{4.13}$$

where $Re(z(\omega))$ is the real part of the vibration amplitude and $\frac{\partial}{\partial\omega}$ its derivative with respect to ω. The FM mixing allows to get a mixing current of purely electromechanical origin (it only has a term that contains the amplitude of motion) and is more efficient in rejecting electrical background noise compared to the two-source mixing or the amplitude modulation technique. However, the measured mixing current containing the mechanical information is not directly proportional to the amplitude of motion but to the real part of the complex resonance response. The line shape is for that reason no longer a Lorentzian. For a FM-line shape, the Q factor of the resonator can be approximated by estimating the linewidth as the separation between the two minima $\frac{\partial}{\partial\omega} Re(z(\omega))$. It is no longer estimated as the full width half maximum as for the Lorentzian response [33].

Amplitude modulation and FM modulation mixing both work with a single source that already creates the mixing. Here, the nanotube or the graphene device therefore only needs to act as a demodulator which recovers the mechanical information from the modulated driving signal.

4.2.2.2 Other electrical detection techniques

Noise measurement

Noise measurement is based on the two-source down mixing scheme and has been developed in the Bachtold group for the detection of the thermal resonance of a carbon nanotube resonator at cryogenic temperatures [8]. This technique has allowed to achieve the highest force sensitivity ever reported thus far. A schematic of the read-out scheme is shown in Figure 4.3. A small oscillating voltage $\tilde{V}_{\mathrm{SD}}^{\Delta\omega} = \tilde{V}_{\mathrm{SD}}\cos(\omega_{\mathrm{SD}})$ is applied to the source of the nanotube where ω_{SD} is a few tens of kHz detuned from

the resonance frequency of the device. A DC voltage is applied to the gate electrode in order to control the tension. This technique does not drive the resonance, since the RF-signal applied to the source is detuned from the resonance frequency and it results in current fluctuations originating from the thermal motion of the resonator which modulates the conductance via the capacitance. At the drain of the device the following current fluctuations can be measured:

$$I^{\omega_{SD}-\omega_0} = \frac{1}{2}\tilde{V}_{SD}\frac{dG}{dV_g^{DC}}V_g^{DC}\frac{C_g'}{C_g}z(\omega_{SD}). \tag{4.14}$$

The current fluctuations are then converted into voltage fluctuations via a resistor and are measured using a Fast-Fourrier signal analyzer. As in the two-source mixing scheme, the current fluctuations measured at the drain can be converted into displacement fluctuations using $z = I^{\omega_{SD}-\omega_0}/\beta^2$ where $\beta = \frac{1}{2}\tilde{V}_{SD}\frac{dG}{dV_g^{DC}}\frac{C_g'}{C_g}V_g^{DC}$. Later on we will see that the read-out we implemented as a part of this thesis also allows us to resolve the thermal motion (see annex A.3).

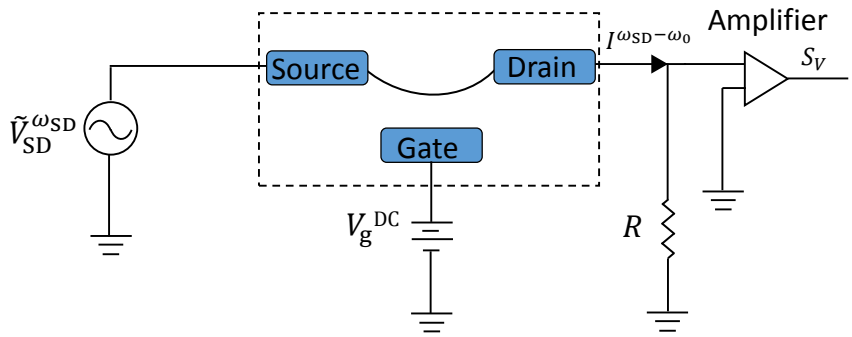

Figure 4.3 – Noise measurement read-out scheme

Rectification technique

In another read-out scheme, the mechanical motion is transduced into a DC signal [42]. This is why it is called rectification. Here the carbon nanotube does not act as a mixer or a demodulator but as a rectifier. The read-out scheme is illustrated in Figure 4.4. The motion is actuated using a nearby antenna which sends an oscillating electric field $\tilde{V}_{RF}^{\omega} = \tilde{V}_{RF}\cos(\omega t)$. The rectification only works if the device is operated in a Coulomb blockade regime. Here, the second order term of the conductance

modulation with the gate ($d^2G/dV_g^{DC^2}$) can not be neglected and results in a DC component of the mixing current which is proportional to the square of the amplitude of motion. The DC component of the mixing current can be measured on the drain by applying a DC-voltage V_{SD}^{DC} to the source and to the gate V_g^{DC}. The DC component is given by:

$$I_{DC} = \frac{1}{4} V_{SD}^{DC} \frac{d^2G}{dV_g^{DC^2}} \left(\frac{V_g^{DC} C_g'}{C_g} \right)^2 z^2 \tag{4.15}$$

The disadvantage of this technique lies it its large 1/f noise since it is working at DC.

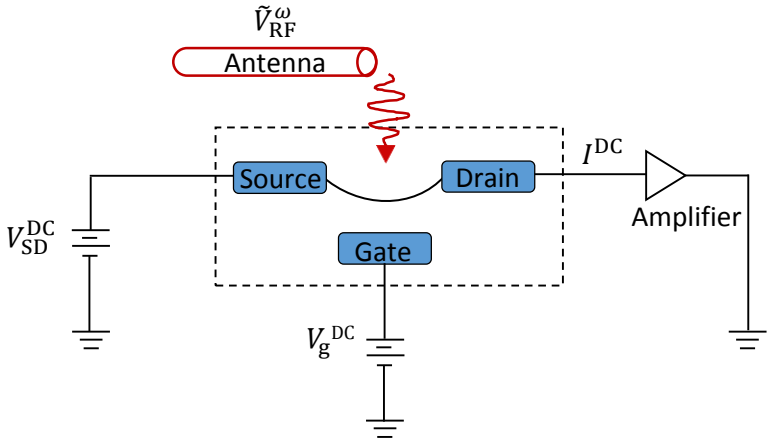

Figure 4.4 – Rectification read-out scheme

Direct electrical detection

All previous techniques have the drawback that they have a limited read-out bandwidth. This makes them unsuitable for RF applications (filters and oscillators). A recent work showed that the direct read-out of graphene resonators is possible [59]. Direct read-out means that the signal carrying the information about the mechanical motion is read out at the same frequency as the resonance frequency of the mechanical motion of the device. Many times this is not possible due to the cut-off frequency previously described. However Xu et al. (2010) managed to achieve direct read-out by working with a graphene device with a local gate and a highly resistive substrate in order to reduce parasitic capacitance which limit the read-out bandwidth. A direct read-out scheme uses a DC as well as an oscillating voltage applied at the gate to drive the resonator as previously described. At the drain the RF-current signal is

read-out with a network analyzer by applying a voltage V_{SD}^{DC} to the source (see Figure 4.5). The measured current is given by:

$$I_{direct}^{\omega} = j\omega C_g\left(\frac{C_{tot}}{C_g}\tilde{V}_g - V_g^{DC}\frac{C_g'}{C_g}z(\omega)\right) + V_{SD}^{DC}\frac{dG}{dV_g^{DC}}\left(\tilde{V}_g - \frac{C_g'}{C_g}z(\omega)\right), \tag{4.16}$$

where C_g is the capacitance between the graphene and the gate and C_{tot} is the total capacitance including the parasitic capacitances. The first term gives the parasitic background signal, the second term originates from the mechanical motion, the third term again gives an electrical background coming from the transconductance, whereas the last term gives the mechanical contribution coming from the transconductance as well. It becomes clear that a high transconductance will facilitate the direct read-out. Small parasitic capacitances will result in a small first term and will allow the observation of the signal of mechanical origin. For high transconductance devices such as nanotubes and graphene, the contribution of the mechanical transconductance term is usually dominating.

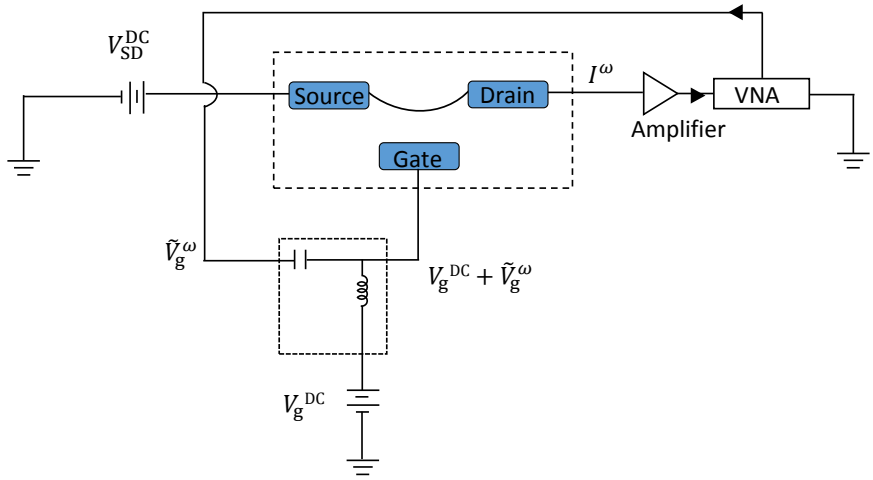

Figure 4.5 – Direct read-out scheme

4.3 Optical actuation and detection

The first experimental demonstration of purely optical actuation and detection of a graphene resonator has been achieved by Bunch et al. [44]. Optical actuation of graphene resonators uses a laser beam focused onto the surface of the device. Intensity modulating the power of the laser beam at the driving frequency results

in a temperature modulation of the device. This temperature modulation leads to a periodic contraction or expansion of the graphene resonator and sets it into motion. For optical detection, another laser beam is used. The reflection of the laser beam at the bottom of the underlying substrate creates an interference pattern with the incoming beam. The reflected laser beam gets intensity modulated when the graphene resonator moves with inside the interference pattern. The graphene motion is detected by recording the intensity modulation of the reflected light using a fast photo-diode.

Optical-read out of carbon nanotubes, in contrast to graphene, is much more challenging. This is due to the small cross sections of carbon nanotubes compared to the optical beam waste of lasers. Beam and resonator interaction needs to be maximized.

5 Mass sensing and frequency fluctuations in NEMS

In this chapter we introduce and derive the mass resolution. It is the figure of merit of the performance of nanomechanical systems as mass sensors. We then describe the parameters defining the mass resolution of a nanomechanical resonator: mass and frequency stability (Allan deviation). In the last part we present the mathematical description of the frequency stability of a resonator limited by the imprecision noise of the detection.

5.1 Introduction

Mass sensing with nanomechanical systems has been a field of interest in application oriented research for many years. The great potential of NEMS for mass sensing is owed to their small masses and high quality factors [109]. The best NEMS based mass sensor reported thus far is based on a carbon nanotube resonator and has been demonstrated in the Bachtold group. It is capable of resolving the mass of a single proton [15]. This level of sensitivity makes NEMS based mass spectrometry a promising future alternative to conventional mass spectrometry. Conventional mass spectrometry is commonly used to analyze the chemical composition of samples. The technique relies on ionization and differentiates elements based on their different mass over charge ratio. Recent efforts have shown that the detection of single proteins in real time is possible with a NEMS based mass spectrometer [21, 48]. The big advantage of using NEMS for mass spectrometry is that ionization is not needed. This means that fragile bio molecules and proteins do not get damaged during the process.

Apart from mass spectrometry, NEMS mass sensors have been used in various experiments to detect a few number of atoms or molecules [11, 12, 13, 110]. Besides, they have also been employed for gas chromatography [111, 112] and as sensors of single particles in liquid environments [113, 114], both of which together with mass

spectrometry are important advances for the exploitation of NEMS in life-science applications. Moreover, they have also been used for fundamental studies of diffusion effects [62], phase transitions [115] and monolayer formation [56].

All recently reported records in mass resolution of NEMS have been possible mainly through downsizing device dimensions and, thus, their mass. However this approach as has one major issue: a smaller resonator is overall more sensitive to its environment. For this reason small resonators typically exhibit large fluctuations of their resonance frequency which limit the mass resolution and hinders achieving the ultimate, thermomechanical noise limited mass resolution. A recent study indeed showed that none of the reported experimental studies have observed a frequency stability limited by the thermomechanical noise of the resonator [61]. A better understanding of the origin of frequency fluctuations in NEMS is a very important step in reaching the full mass sensing potential of NEMS. In the following sections we introduce important concepts needed to evaluate and understand the mass resolution and frequency fluctuations in nanomechanical resonators.

5.2 Mass resolution

In mass sensing with nanomechanical systems one exploits the fact that the resonance frequency f_0 of a resonator is sensitive to its mass. This means that any added mass δm will lead to a shift in the resonance frequency δf_0. We want to derive the relation between the added mass and the shift in the resonance frequency from the kinetic energy of the simple harmonic oscillator. When a point like particle of mass δm lands on the resonator, the resonator's kinetic energy will be increased by the kinetic energy attributed to the point like particle. The kinetic energy of the point-like particle will depend on the time dependent local deflection of the resonator described by the modeshape function $\xi(x',t)=(z(t)\cdot u(x'))$ introduced earlier. The kinetic energy depends on the position x' where the particle lands and the modeshape $u(x')$. Hence the total kinetic energy of the combined system of the resonator and the particle can be described by:

$$\langle E_{\mathrm{kin,tot}}\rangle = \frac{1}{2}m_{\mathrm{eff}}\dot{z}(t)^2+\frac{1}{2}\delta m[u(x')]^2\dot{z}(t)^2=\frac{1}{2}(m_{\mathrm{eff}}+\delta m[u(x')]^2)\dot{z}(t)^2. \qquad (5.1)$$

This kinetic energy is equivalent to the kinetic energy of a harmonic oscillator of mass $m'=m_{\mathrm{eff}}+\delta m[u(x')]^2$. This means that the resonance frequency of the resonator together with the particle is given by:

$$f_0'=\frac{1}{2\pi}\sqrt{\frac{k}{m_{\mathrm{eff}}+\delta m[u(x')]^2}}\approx\frac{1}{2\pi}\sqrt{\frac{k}{m_{\mathrm{eff}}}}\left(1-\frac{1}{2}\frac{\delta m[u(x')]^2}{m_{\mathrm{eff}}}\right), \qquad (5.2)$$

where the last approximation is the result of a taylor series of the square root for $\delta m \ll m_{\text{eff}}$. The shift in resonance frequency given by $\delta f_0 = f_0 - f_0'$ is therefore described by the following equation [21]:

$$\delta f_0 = \left(-\frac{1}{2}\frac{f_0}{m_{\text{eff}}}[u(x')]^2\right)\delta m, \tag{5.3}$$

where the factor $-\frac{1}{2}\frac{f_0}{m_{\text{eff}}}[u(x')]^2$ is known as the responsivity of NEMS. Looking at this equation we see that if a particle lands where the amplitude of displacement in z is maximum, that is at the anti-node of the mechanical mode, then the frequency shift is maximum, whereas if it lands at the clamping points (nodes of vibration) the frequency shift is 0. The equation only holds true for cases where the spring constant, that means the stiffness, of the resonator does not change with the adsorption of a particle. Additionally, it assumes that the modeshape stays unchanged before, during and after the landing of a particle.

The mass resolution gives the value of the smallest mass δm that can still be resolved. Here, one typically looks at the mass resolution assuming the maximum response in frequency shift. The maximum response is equivalent with the landing point of the particle where $\max(u(x')) = 1$. This means that $[u(x')]^2 = 1$. The mass resolution is then given by:

$$\delta m = 2m_{\text{eff}} \cdot \frac{\delta f_0}{f_0}. \tag{5.4}$$

The smallest detectable mass δm is directly proportional to the effective mass m_{eff} of the resonator and therefore also to the mass of the resonator [1]. Carbon based nanomechanical systems with their low mass are very attractive for high mass resolution sensing. As introduced in chapter 2.3, carbon nanotubes and graphene constitute the ultimate limit in dimensions and consequently also in mass. They have a significantly smaller mass (ag-1fg) compared to other materials used for NEMS (several tenths of fg). Additionally, their resolution can be further tuned by downscaling their device dimensions. This leads to an even smaller mass and at the same time higher resonance frequencies. Both of which improves the mass resolution. However, the mass resolution also scales linearly with δf_0, the smallest frequency shift that can still be resolved. This parameter is limited by the frequency fluctuations of the resonator. We can also say that δf_0 is given by the frequency fluctuations. The normalized frequency fluctuations $\frac{\delta f_0}{f_0}$ are also known as frequency stability. Typically

[1] In a more simple manner this equation can also be derived by just assuming $m' = m_{\text{eff}} + \delta m$. Then the resonance frequency is simply given by $f_0' = \frac{1}{2\pi}\sqrt{\frac{k}{m_{\text{eff}}+\delta m}} \approx \frac{1}{2\pi}\sqrt{\frac{k}{m_{\text{eff}}}}\left(1-\frac{1}{2}\frac{\delta m}{m_{\text{eff}}}\right)$ and the shift in resonance frequency then becomes $\delta f_0 = f_0 - f_0' = -\frac{\delta m}{2m_{\text{eff}}} \cdot f_0$. This result however does not consider the modeshape dependence.

the frequency stability is estimated by evaluating the time dependent measurement of the frequency fluctuations by calculating the Allan deviation.

5.3 Allan deviation

The Allan deviation of the resonance frequency does not only allow us to evaluate the mass resolution of a resonator but it also provides information on the nature of the noise of the mechanical resonator. We compute the Allan deviation as [116]

$$\sigma_{\text{Allan}}(\tau_{\text{A}}) = \sqrt{\frac{1}{2(N-1)} \sum_{i=1}^{N-1} \left(\frac{\overline{f}_{i+1} - \overline{f}_i}{f_0} \right)^2}, \tag{5.5}$$

with $\overline{f}_i$ being the averaged frequency during the time interval i of length τ_{A}, f_0 the resonance frequency averaged over the whole measurement and N the total number of time intervals. The Allan deviation is usually plotted as a function of the time τ_{A}, which is often called the integration time. The Allan deviation can be seen as the time-domain equivalent of the power spectral density of the fractional noise of the resonance frequency $S_{\delta f_0/f_0}$. The Allan deviation is related to the spectral density of the fractional frequency noise by the following equation [117]:

$$\sigma_{\text{Allan}}(\tau_{\text{A}}) = \sqrt{2 \int_0^\infty S_{\delta f_0/f_0}(f) \frac{\sin^4(\pi \tau_{\text{A}} f)}{(\pi \tau_{\text{A}} f)^2} df}, \tag{5.6}$$

From this equation one can derive the Allan deviation for any known power spectral density of frequency noise. When the frequency noise is a 1/f noise, the Allan deviation remains constant when increasing τ_{A}. When the frequency noise is white, the Allan deviation scales as $1/\sqrt{\tau_{\text{A}}}$ [118]. Even though the power spectral density of the frequency noise can be accessed experimentally, the Allan deviation is the more useful parameter if one wants to understand the resonator sensitivity performance on specific time scales. This is the case in any study of dynamic processes as for example in mass sensing experiments.

5.4 Frequency fluctuations and imprecision noise

Frequency noise can have different origins. The fundamental limit of frequency noise is given by the thermal noise of the resonator and is present in all devices. However, the frequency stability of all the measured devices was never limited by their thermomechanical noise [61]. The frequency stability was either limited by

imprecision noise in the detection or by other sources of frequency noise intrinsic to the device. The different type of noise sources that contribute the overall noise affecting the frequency stability are schematically shown in Figure 5.1. The main sources of noise are: thermomechanical noise, noise in the transduction of the motion, noise in the amplification and any additional electrical noise. Details on noise processes that govern the noise in the transduction of the motion can be found in Reference [119]. Theoretical models that account for other noise sources affecting the frequency stability are temperature fluctuations [120], adsorption-desorption noise [62, 118], diffusion [121] and defect motion [118]. The theoretical Allan deviation for these noise processes that are intrinsic to the device - meaning they originate from the mechanical domain of the device- can be found in References [118] and [62]. Identifying the origin of frequency noise in experiments remains quite a difficult task. In some experiments frequency fluctuations could be indeed attributed to the uncontrolled adsorption and desorption of molecules and atoms on and from the surface [62]. In general, frequency noise is more pronounced in smaller resonators owed to the fact that their resonance frequencies are more receptive to changes in their environment.

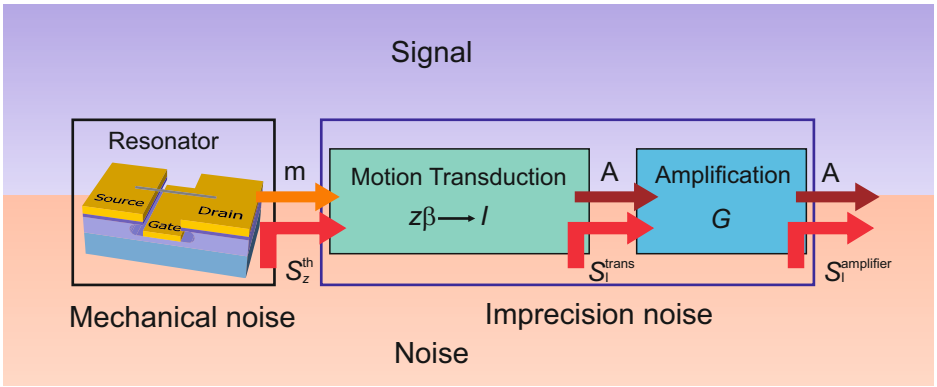

Figure 5.1 – Schematic showing the different noise sources that contribute to the noise affecting the frequency stability. Other noise sources intrinsic to the device add up to the thermomechanical noise in the mechanical domain. (The schematic is adapted from [119].)

Imprecision noise in the detection contributes to the frequency noise of nanomechanical resonators. However it cannot be easily differentiated from other sources of frequency noise. It manifests itself as additive white noise and reduces the overall frequency stability of the resonator. Additive because it appears in the form of added noise in the signal amplitude which is translated into frequency noise. The Allan

deviation for an imprecision noise limited system is given by:

$$\sigma_{\text{Allan}}(\tau_A) \cong \frac{\Delta f}{f_0}\frac{N_T}{S}\sqrt{\frac{1}{2\pi\tau_A}}, \tag{5.7}$$

where S is the signal amplitude of the driven resonance at f_0, Δf the full width at half maximum of the resonance, and N_T the noise floor of the detection. The factor $\frac{1}{2\pi\tau_A}$ is only valid for a first order low pass filter and changes for measurements performed with a higher order filter [61]. Looking at the equation we can see that an increase in the signal to noise ratio results in an improvement of the overall frequency stability. The improvement in the signal to noise ration can be either achieved by lowering the detection noise or by increasing the signal level by applying a higher driving force. The frequency stability is also affected by the mechanical linewidth of the device.

Thermal noise is a white noise. The frequency stability of a resonator limited by thermal noise can also be described by equation 5.7, where the noise level N_T is given by the thermal noise of the resonator. In the limit of thermomechanical noise however the frequency stability is more commonly described by the dynamic range equation given by [122]:

$$\langle\frac{\delta f_0}{f_0}\rangle = \frac{1}{Q}10^{-(\text{DR}/20)}, \tag{5.8}$$

where DR represents the dynamic range. The dynamic range is defined as the ratio between the maximum signal in the linear response regime of the resonator (also known as the critical amplitude A_c) compared to the signal level of the thermal noise peak expressed in dB. The dynamic range is given by $DR = 10\log\left(\frac{E_c}{k_B T}\right)$, where $E_c = m_{\text{eff}}\omega_0^2\langle z_c^2\rangle$ is the energy of the resonator at the critical amplitude A_c. Equation 5.8 can then be written in terms of the signal to noise ratio in the mechanical domain including the dependence on the measurement integration time τ_A :

$$\langle\frac{\delta f_0}{f_0}\rangle \propto \frac{1}{Q}\frac{\sqrt{S_z^{\text{th}}}}{A_c}\frac{1}{\sqrt{2\pi\tau_A}}, \tag{5.9}$$

where $S_z^{\text{th}} = \frac{4k_B TQ}{m_{\text{eff}}\omega_0^3}$ is the thermomechanical noise spectral density at resonance as given by equation 3.13. This equation is equivalent to equation 5.7 with the signal to noise ratio defined in the mechanical domain. Here the noise floor is given by the thermomechanical displacement noise $\sqrt{S_z^{\text{th}}}$ instead of the noise of the detection. In the literature, the mass resolution is commonly estimated based on the DR equation [41, 123, 124, 125]. This equation gives the frequency stability of a resonator and consequently the mass resolution in an ideal case scenario, where the noise level is

given by the thermomechanical noise of the resonator, whereas measurements of the resonance frequency fluctuations as a function of time allow to access a realistic value of the frequency stability using equation 5.5.

Now that we have introduced the concept of the Allan deviation, we come back to the initial question on how the Allan deviation relates to the mass resolution. The Allan deviation quantifies $\frac{\delta f_0}{f_0}$. This means that the mass resolution can be estimated from the Allan deviation by the following relation:

$$\delta m(\tau_A) = 2m_{\text{eff}} \cdot \frac{\delta f_0}{f_0} = 2m_{\text{eff}} \cdot \sigma_{\text{Allan}}(\tau_A). \tag{5.10}$$

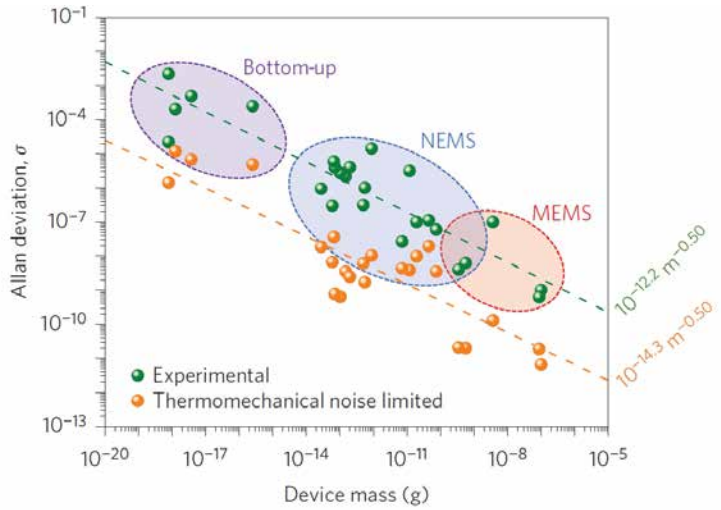

Figure 5.2 – Dependence of the experimentally observed frequency stability and the thermomechanical noise limited frequency stability of micromechanical, nanomechanical and bottom up fabricated resonators on their mass at room temperature. (adapted by permission from ©Springer Nature [61].

How the mass resolution scales with the device dimensions depends on how the Allan deviation scales with the device dimensions and this in turn depends on the origin of the frequency noise. It has been shown recently that independent of the design and the type of mode of the resonator both the theoretical thermomechanical noise limited Allan deviation and the experimentally observed Allan deviation scale as $1/\sqrt{m}$, where m is the mass of the resonator (see Figure 5.2). This holds true from MEMS over NEMS to bottom up fabricated resonators. This means that the mass

resolution is expected to scale as [61]:

$$\delta m \propto \sqrt{m}, \tag{5.11}$$

since m_{eff} is proportional to m. The mass resolution is consequently expected to scale as $\sqrt{wL}$ in the case of a double clamped graphene resonator of width w and length L and as $\sqrt{rL}$ in the case of a nanotube resonator of diameter r and length L.

6 Mass sensing with graphene resonators

In this chapter we study the mass resolution of several short (length$\leq 1\,\mu$m) double clamped resonators made out of graphene. After a short introduction on the use of graphene resonators for mass sensing we present the fabrication technique employed to achieve such resonators. We then describe the experimental setup used throughout all the measurements presented in this thesis. Afterwards we discuss the experimental results, from the electrical and mechanical properties to the mass resolution and the observation of the adsorption of fullerene molecules on the surface of the resonator. We finish the chapter with a discussion on the limitation of the frequency stability.

6.1 Introduction

Mass sensors based on mechanical systems have found their way into a large number of applications for quite some time [109]. Some examples are quartz oscillators [126] and micro-cantilevers [127]. They all rely on the detection of the shift in resonance frequency which is directly proportional to the mass of the probed molecules or atoms adsorbed on the surface. The great potential of nanomechanical resonators for mass sensing originates from their minuscule mass and high resonance frequencies compared to macro-scale or micro-scale resonators. The limit in mass resolution with nanomechanical systems was predicted to lie around 1.7 yg [109]. Only recently the theoretical limit has been experimentally demonstrated with a carbon nanotube resonator [15]. Up till today this result still constitutes the record in mass resolution.

Among all nanomechanical resonator based mass sensors, carbon nanotube and graphene represent the smallest resonators measured thus far and therefore also the best mass sensors. For this reason carbon based nano-mechanical systems are always in the spotlight when looking for unprecedented mass resolution. Graphene nanomechanical resonators are not expected to achieve a mass resolution compa-

rable to that of carbon nanotubes due to their larger mass. However, they have two important advantages over carbon nanotubes. Firstly, they have a much larger surface area which allows to capture and analyze a large amount of analyte in sensing experiments and secondly, they are compatible with large scale fabrication and implementation. Both, the size of the captive area as well as the possibility of large scale integration are of outermost importance if mass sensors based on carbon based nanomechanical resonators want to be utilized for applications.

The ultimate theoretical mass resolution of a resonator is defined by the frequency stability limited by the thermomechanical vibrations of the resonator (chapter 5). However, the regime where exclusively thermomechanical noise determines the frequency stability has never been reached experimentally [61]. For this reason, the study of the frequency stability of the ultimate two-dimensional mechanical mass sensing system- graphene- is an important step in getting closer to uncovering the fundamental noise processes currently limiting the mass sensing performance.

In this chapter, we perform first frequency stability measurements with double clamped graphene resonators (540 nm to 1 μm long) at 4.2 K that allow us to access the mass resolution of these devices. We find the mass resolution to be around 49±25 zg, comparable to state of the art silicon carbide devices. We then study the adsorption of fullerene molecules on these resonators. As already expected from the mass resolution of 49±25 zg which corresponds to the mass of about 41 fullerene molecules, we are not able to observe the adsorption of single fullerene molecules. The frequency stability suggests that we are limited by the measurement imprecision noise. The large imprecision noise of the detection also explains why we are not able to observe the mechanical motion of graphene devices with lengths below 540 nm.

6.2 Fabrication

In this section, we give a brief summary of the fabrication methods that were used to achieve the nanoelectromechanical resonators made out of graphene.

When choosing the device design and fabrication process for graphene nanomechanical resonators it is important to have in mind the importance of having (i) very clean devices which is crucial for sensing experiment and (ii) low parasitic capacitance between the electrodes and the back gate (crucial for the capacitive read-out of the mechanical motion). We achieve clean devices by transferring graphene in the last step of the fabrication process. In this way, the graphene is exposed to less chemicals compared to other techniques. The parasitic capacitance is minimized by working with a local gate configuration rather than with a global gate (e.g. using a doped

silicon substrate). In the following we explain the two main steps of the fabrication process of graphene resonators: the fabrication of the source and drain electrodes separated by a trench with a local gate at the bottom and the transfer process of graphene.

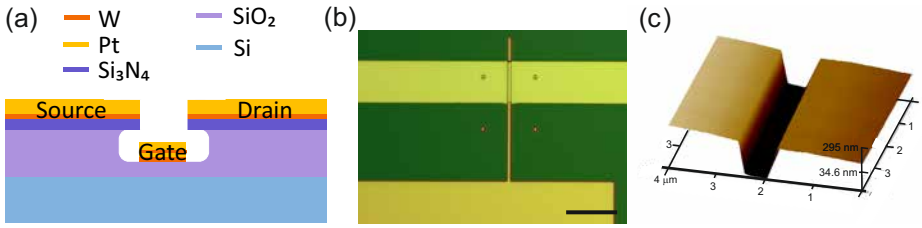

Figure 6.1 – Prefabricated trenches. (a) Cross section schematic of prefabricated trenches. (b) Optical microscope image of a final trench. The scale bar is 10 µm. (c) Atomic force microscope (AFM) image of one of the final trenches.

Fabrication of substrate

In a first step, we fabricate three terminal devices that consist of two electrodes separated by a trench with a local gate electrode at the bottom [128]. Their layout is shown in Figure 6.1 (a). For this, highly resistive silicon (Si) wafers covered with a layer of thermally grown silicon dioxide (SiO_2) and a layer of silicon nitride (Si_3N_4) are used. The Si_3N_4 is grown by plasma enhanced chemical vapor deposition. On these wafers trenches are defined by UV-photolithography. The photoresist-mask is then transferred into the Si_3N_4 via an reactive ion etching (RIE) step. This is followed by a wet etching process in buffered oxide etchant (1:7)) to etch a part of the underlying SiO_2, and to create the undercut needed for separating the metal electrodes. After that, a a double layer composed of 5 nm of tungsten (W)and 75 nm of platinum (Pt) is evaporated to define the gate electrode together with a bond-pad. In a second UV-lithography step, source and drain electrodes are patterned as continues lines crossing the trenches. In a final step another double layer composed of 5 nm of W and 75 nm of PT is evaporated and lifted-off [129]. This defines the source and drain bond-pads and the electrical contacts ending at the trench. The final distance between the electrodes and the gate is either 350 nm or 150 nm and the separation between the source and the drain electrodes is between 1 µm and 170 nm depending on the device. An optical microscope and an AFM image of the final trench structure are shown in Figure 6.1 (b) and (c) respectively. The optical image shows the source,drain and gate electrodes (Figure 6.1 (b)). The AFM image shows just a small area (4 µm by 4 µm in size) of the trench with the electrodes (Figure 6.1 (b)). We then transfer

graphene on these predefined trenches with electrodes and local gate contacts.

Graphene transfer

In order to place graphene on top of prepatterned trenches we use a transfer technique that was first developed by Dean et al. at Columbia University [130] (Figure 6.2). In our group it was implemented and used by Weber et al. [131]. To realize this type of transfer we start with the mechanical exfoliation of graphene from graphite crystals using polydimethylsiloxane (PDMS). Graphene flakes are then further exfoliated from the PDMS onto a Si substrate previously spin coated with a 100 nm thick layer of polyvinyl alcohol (PVA) and a 200 nm thick layer of polymethylmethacrylat (PMMA) 495 K (Figure 6.2(b)). PDMS is used because it introduces less residues than standard scotch tape. The thickness of the PVA/PMMA double layer is selected in order to give the largest optical contrast of graphene in an optical microscope. The optical contrast can be calibrated such that it allows to recognize single and bilayer graphene flakes [132, 133]. Figure 6.3 shows optical microscope images of monolayer and bilayer graphene flakes on a Si/PVA/PMMA substrate. Once we have found a monolayer or bilayer graphene flake (Figure 6.4 (a)), the PMMA membrane is separated from the Si substrate by dissolving the PVA layer in DI-water (Figure 6.2(d,e)). The membrane with the graphene monolayer is then fished out of the water with a brass slide that has a hole with the shape of a volcano (Figure 6.2(f)). The hole permits the membrane to stay suspended (Figure 6.2(g)). Afterwards, the PMMA membrane is dried on a hot plate at 105 °C and then the brass slide is mounted upside down into a micro-manipulator. With the help of the micro-manipulator the graphene flake can be aligned with the trench using an optical microscope (Figure 6.2(h) and 6.5(a)). Once the alignment is controlled, we bring the sample into contact with the membrane by slowly moving up the stage of the microscope, ensuring at the same time that neither flake nor trench move relative to each other. This process is repeated at different temperatures of the substrate. At a certain point the temperature will be high enough for the PMMA membrane to partly melt and then stick to the substrate. At this moment the graphene flake is transferred onto the trench. The substrate together with the PMMA membrane and the graphene flake can be separated easily from the volcano. The transfer temperature varies strongly with the humidity of the environment but usually lies around 130 °C. After this the only step left is the removal of the PMMA membrane which covers the substrate. Mechanical stability is crucial for the device performance and lifetime [135]. In order to ensure the mechanical stability, we use part of the PMMA membrane to clamp the resonator on its two sides. This is done by overexposing (cross-linking) part of the PMMA with ebeam lithography using dose of 10 000 $\mu C/cm^2$ [131]. The unexposed PMMA is

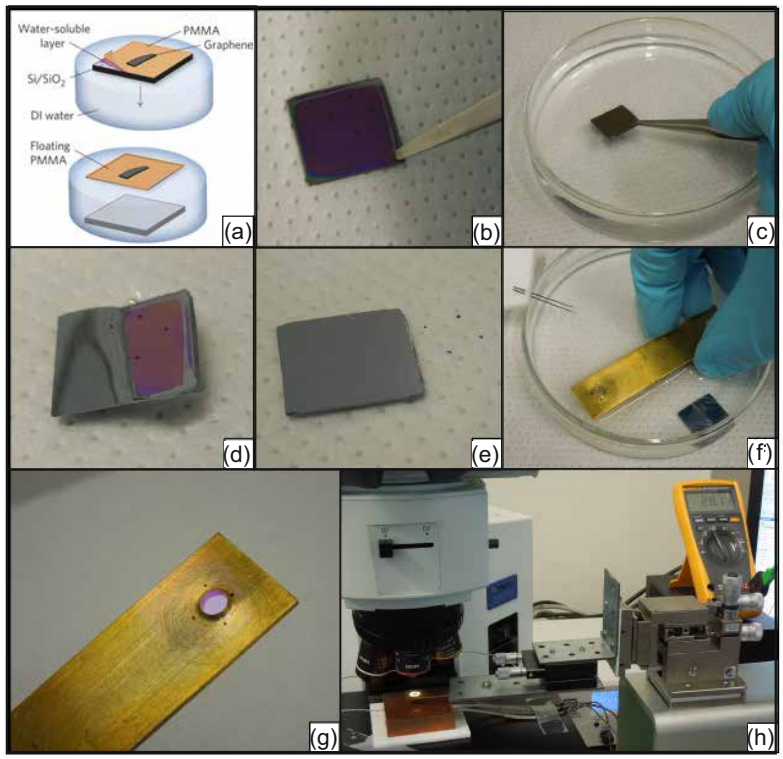

Figure 6.2 – Graphene transfer using a PMMA membrane. (a) Process of releasing the PMMA memrane with the graphene flake from the Si substrate. (Adapted from [130]) (b) One starts with an exfoliated graphene flake on a Si substrate with a double layer of PVA(100 nm)/PMMA(200 nm). The double layer is selected such that the contrast resembles the contrast for a Si substrate with 285 nm of SiO_2 [132] which allows to identify monolayers of graphene. (c) The substrate is placed onto the surface of DI-water. (d) Once the water starts to dissolve the PVA, the PMMA membrane gets separated from the Si substrate. (e) The substrate sinks to the bottom of the beaker and the membrane keeps floating (four blue points).(f) The membrane is fished from the surface with the brass with a vulcano shaped hole. (g) The membrane is homogenously extended and suspended over the volcano shaped hole after drying at 105 °C on a heater. (h) Transfer setup consisting of an optical microscope, a micromanipulator where the brass slide is mounted and a copper-block used to heat the substrate. Figure adapted from [134].

then removed in an acetone bath. Afterwards the sample is dried in a critical point dryer. This process results in a graphene resonator with its ends clamped by the cross-linked PMMA (Figure 6.5 (b,c)). In Figure 6.5 (b) we can see the cross-linked PMMA on two sides of the trench within the red rectangle. It can be differentiated from the electrode by its slightly green color.

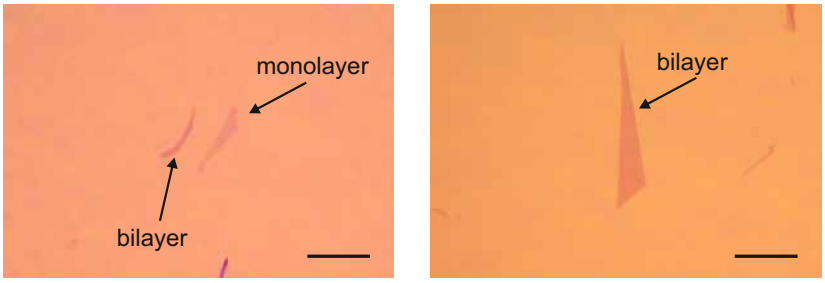

Figure 6.3 – Optical images of monolayer and bilayer graphene on a silicon substrate coated with a PVA/PMMA. The bilayer graphene on the right optical image was used for the graphene drum device illustrated in Figure B.2. The scale bars are 20 µm.

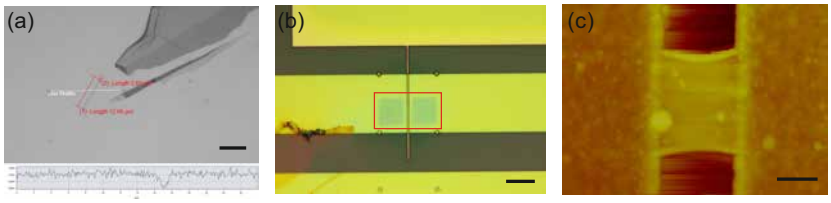

Figure 6.4 – Graphene resonator device and graphene flakes. (a) Bilayer graphene flake used for device C on a Si substrate coated with PVA/PMMA. The contrast difference with the background is around 800 a.u. The contrast for a monolayer graphene flake on the same substrate was previously calibrated to be around 400 a.u. The scale bar is 10 µm. (b) Final device under optical microscope. Red rectangle indicates area where the flake crosses the trench. The device is clamped by cross-linked PMMA (green areas). (c) AFM image of one of the final devices. The scale bar is 300 nm.

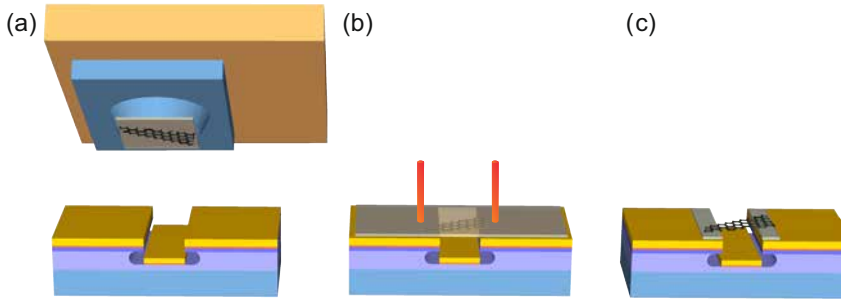

Figure 6.5 – Fabrication of graphene mechanical resonators. (a) Graphene transfer with PMMA membrane (grey) on top prefabricated trenches. (b) Cross-linking of PMMA on top of graphene flake using the electron beam (red). (c) Schematic of final graphene resonator after cleaning and critical point drying.

In a last step we improve the contact resistance of the sample and clean it from resist and chemical residues by performing an oven annealing at 240 °C for 1 hour in an argon (500 mln/min)/ and hydrogen (200 mln/min) atmosphere. An example of an optical microscope image of a final device can be seen in Figure 6.4(b) and an atomic force microscope image in Figure 6.4(c). Two graphene resonator that have been fabricated are shown in Figure 6.6 (a,b). The resonator shown in Figure (a) is the smallest graphene resonator that has been fabricated. It has a length of 170 nm.

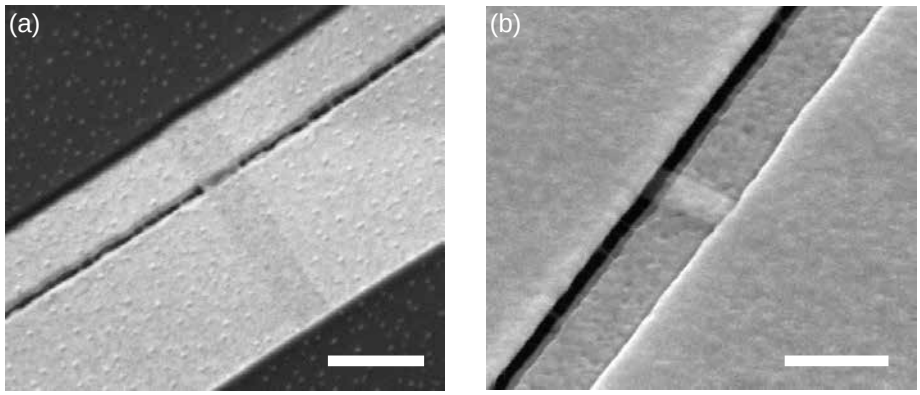

Figure 6.6 – Scanning electron micrograph of two graphene resonator that have been fabricated. (a) The monolayer graphene flake is ≈347 nm wide and the suspended part is ≈170 nm long. The scale bar is 1 μm. (b) The monolayer graphene flake is ≈190 nm wide and the suspended part is ≈370 nm long. The scale bar is 500 nm.

6.3 Experimental setup

The measurement setup we use throughout the work of this thesis is shown in Figure 6.7(a). It consists of a homebuilt ultra-high-vacuum (UHV) chamber and a cryogenic insert (ST-400, Janis Research Company). The system reaches a base pressure of $\sim 3 \cdot 10^{-11}$ mbar after two days of baking at 110 °C. The device is mounted on a printed circuit board[1] which is attached to the cold finger of the cryogenic insert and electrically connected via UHV compatible radio frequency cables[2] (Figure 6.7(b)). Only one device can be connected at a time and cooled down to 4.2 K using liquid helium. An ion gauge[3] monitors the pressure of the champer, and a diode[4] the temperature of the device. Additionally, the setup is equipped with a microdoser that can inject

[1] Novatek, double side, dielectric: Rogers RO3003 (0.8 mm), base copper thickness: 35 μm, surface finishing:chemical golden.
[2] Allectra 380-SMA-MF-500
[3] Varian, XGS-600
[4] DT-670B-Cu diode together with Lakeshore 332 temperature controller

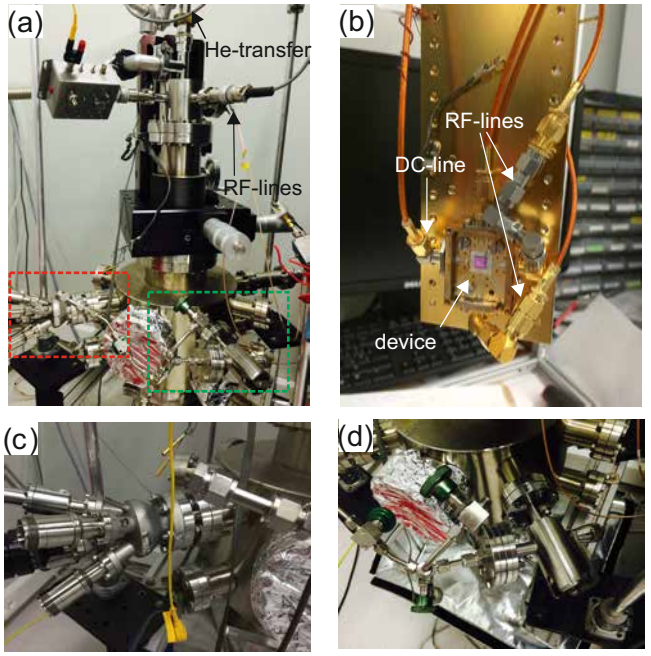

Figure 6.7 – UHV setup with cryogenic insert used to measure devices. (a) Picture of the setup. The red rectangle indicates the evaporator. The green rectangle shows the microdoser. (b) Cold finger of cryogenic insert with the PCB, the device and the electrical connections. (c) Thermal evaporator. (d) Pinhole microdoser.

gas atoms through a pinhole into the chamber (Figure 6.7(d). Moreover, there is a thermal evaporator[5] that allows to evaporate fullerene molecules onto our device (Figure 6.7(c)). The evaporator is aligned with the device location in such a way that the focus of the molecular beam lies on the surface of the sample. It has a mechanical shutter that allows switching on and off the dosing of fullerenes. The rate at which the molecules are dosed depends on the temperature of the crucible of the evaporator and must be experimentally calibrated.

6.4 Experimental results

6.4.1 Characterization

The very first characterization of any sample we measure is the measurement of the electrical resistance at room temperature. The graphene resonators we study have

[5] evaporation source organic molecular beam epitaxy, Dodecon nanotechnology GmbH

typically a two-point resistance between a few kΩ and several tenths of kΩ.

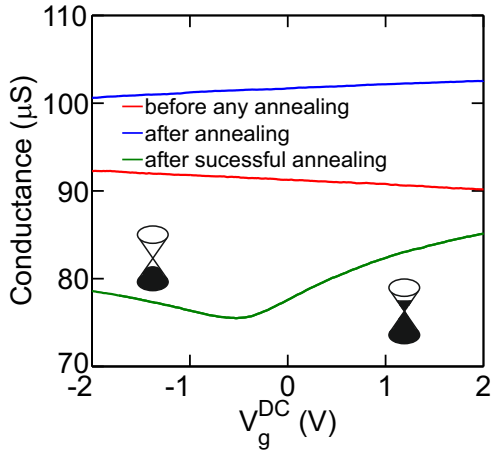

Figure 6.8 – Gate dependence of the conductance of one of the devices measured at 65 K before and after the last two annealing steps. The last annealing step is considered as succesful because it restores the charge neutrality point close to the zero gate voltage point.

In a next step, the sample is cooled down with liquid nitrogen to 65 K. At this temperature we study the change of the conductance as a function of the gate voltage. We then anneal the device for 1-2 min by passing a large current. This process is repeated several times and the annealing current is increased each time. This is needed to clean the graphene from contamination, which otherwise would act as dopants and interfere with the electronic properties of graphene in an irreproducible way (as already explained in chapter 2.2). Figure 6.8 shows the gate voltage dependence of the conductance of one of the devices measured before any annealing and after the last two annealing steps. After the last annealing step (300 μA) we observe the charge neutrality point close to zero gate voltage and the regime of hole and electrons transport (green curve).

Once we have a clean device we start to characterize its mechanical modes using electrostatic actuation and the frequency modulation mixing technique (chapter 4.2.2.1) to drive and read-out the motion. The response of the graphene motion as a function of the frequency of the driving force is proportional to the transconductance and the gate voltage applied to the local gate below the resonator (equation 4.13). For this reason the highest signal is typically observed where both the transconductance and the gate voltage are maximized. Figure 6.9 shows an example of the eigenmode spectrum of two of the measured resonators taken at 4.2 K. Both spectra show three prominent resonance peaks.

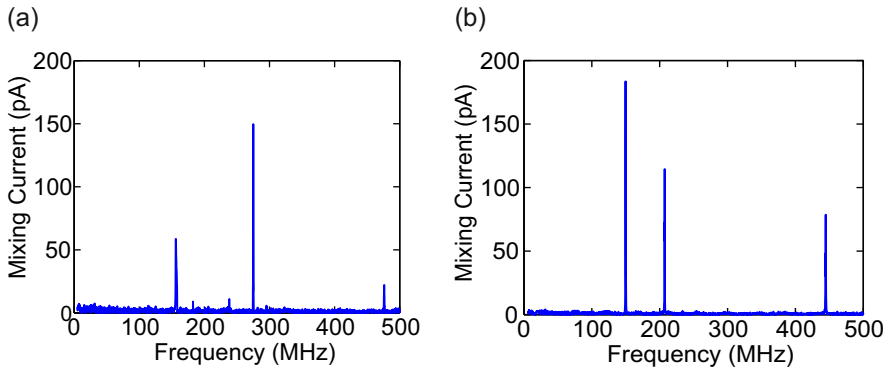

Figure 6.9 – Frequency spectrum of two different graphene devices measured at 4.2 K. (a) Device A. The measurement is taken at V_g^{DC}=-3 V and a driving amplitude of V_{FM}=10 mV. (b) Device B. The measurement is taken at V_g^{DC}=4 V and a driving amplitude of V_{FM}=5 mV.

The mechanical origin of any observed resonance peak is confirmed by measuring a change in the resonance frequency as a function of V_g^{DC}. Most devices have a low built-in tension. In this case capacitive hardening dominates the frequency dependence on V_g^{DC} (Figure 6.10). This means that the resonance frequency (and therefore the spring constant) increases with increasing $|V_g^{DC}|$. It can be understood in the following way: The equilibrium position of the resonator moves towards the gate electrode when increasing $|V_g^{DC}|$, therefore the device gets more and more stretched. This leads to an increase of the tension in the device, equivalent to an increase in the effective spring constant and consequently in the resonance frequency [136].

One device (device C) is found to have a significantly high built-in tension. In this case capacitive softening as described in chapter 3.3.4 governs the V_g^{DC} dependence of the resonance frequency on the gate voltage (Figure 6.11 (a)). It originates from nonlinear terms in the electrostatic force. Where capacitive softening dominates, the resonance frequency decreases quadratically upon increasing $|V_g^{DC}|$ as described by equation 3.43. We quantify the built-in tension T_0 and the effective mass m_{eff} of device C by fitting the resonance frequency dependence on V_g^{DC} in Figure 6.11 (a) using $f(V_g) = f_0 - f_0 \frac{L}{4\pi^2 T_0} C_g'' V_g^2$ (equation 3.43). Here, $L = 540 \pm 19$ nm is the length of the device and C_g'' the second derivative of the capacitance with respect to the displacement. C_g'' can be estimated with the plate capacitor model, knowing the area of the device and the distance to the gate from AFM measurements. The built-in tension is found to be 1330 ± 338 nN and the effective mass 2.4 ± 0.6 fg. The effective mass of a pristine graphene resonator of the same dimension is $m_{eff} = \frac{m_{pristine}}{2} = 0.26 \pm 0.02$ fg (equation 3.41). Here, $m_{pristine}$ is taken as the mass of a pristine bilayer

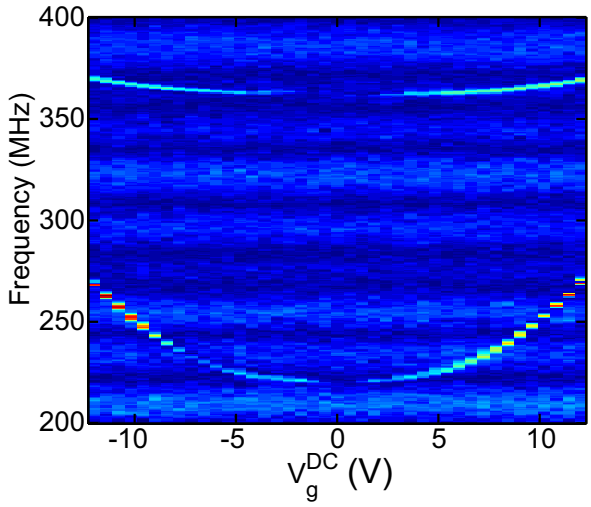

Figure 6.10 – Gate voltage dependence of the mechanical resonance frequency of device D measured at 78 K. The color scale corresponds to the mixing current. Dark red corresponds to 350 pA. The response shows that the device has a small built-in tension since the capacitive hardening dominates.

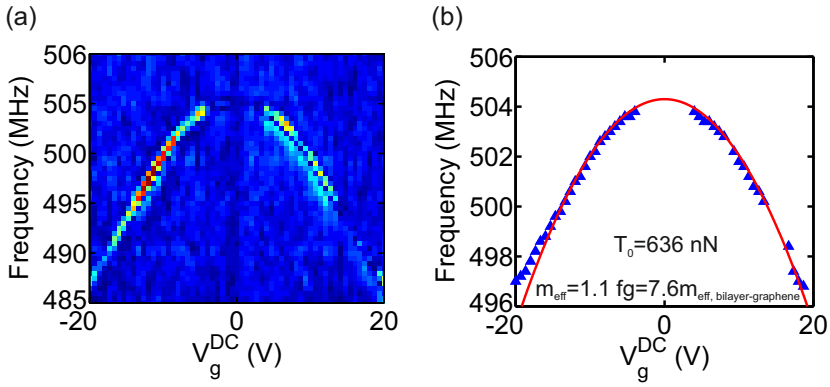

Figure 6.11 – Gate voltage dependence of the mechanical resonance frequency of device C measured at 4.2 K. (a) The color scale corresponds to the mixing current. Dark red corresponds to 120 pA. (b) Comparison between the experimentally measured resonance frequency and equation 3.42.

graphene, since device C is a bilayer. The effective mass determined from the fit is about a factor of 9 higher then the corresponding effective mass of a pristine graphene resonator. The higher mass can be attributed to residual contamination present on the surface of the graphene resonator coming from the fabrication process. Both the built-in tension and the effective mass found for this device are similar to values reported in literature for graphene resonators [33, 35, 41].

6.4.2 Allan deviation and mass resolution

The Allan deviation as introduced in chapter 5.3 is the parameter we use in order to quantify the frequency stability of all our resonators. As previously discussed, the Allan deviation allows to quantify the frequency fluctuations and therefore the mass resolution. Additionally it allows to gain an insight into the noise processes limiting the frequency stability.

We measure the fluctuations of the resonance frequency by driving the resonator at a setpoint frequency f_{driv} where the slope of the response is highest (see Figure 6.12). A change in resonance frequency leads to a change in the mixing current I_{mix}. When the resonance frequency drifts more than a certain limit value (indicated by the grey doted lines), we use a computer-controlled feedback loop to correct the driving frequency in order to return to the setpoint for which the slope of the response is highest [15]. We can convert the measured current fluctuations into frequency fluctuations knowing the slope around the setpoint. From the time dependent measurement of the resonance frequency fluctuations we then calculate the the Allan deviation using equation 5.5 (chapter 5.3).

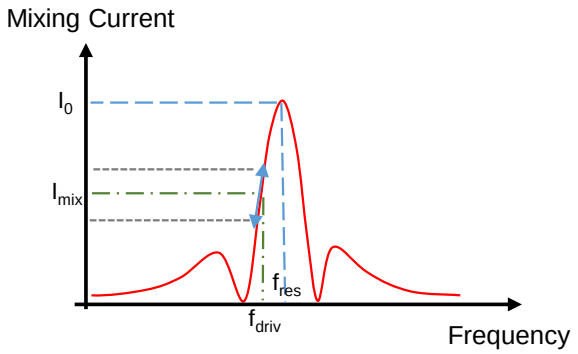

Figure 6.12 – Schematic of the response of the mixing current as a function of the driving frequency.

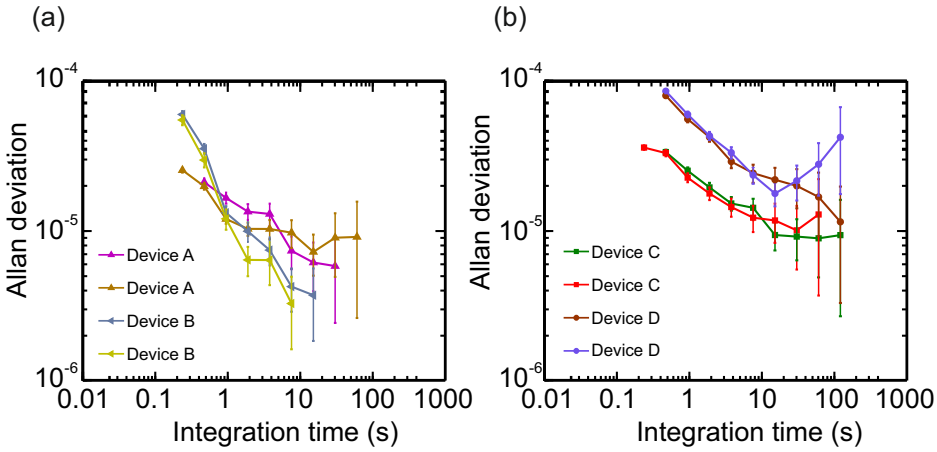

Figure 6.13 – Allan deviation of four different graphene devices at 4.2 K. (a) The suspended part of graphene devices A and B is ∼1 µm. The measurements of device A are performed applying a frequency-modulated oscillating voltage with amplitude $V_{FM} = 2$ mV (brown curve)and $V_{FM} = 3$ mV (violet curve). The measurements of device B are performed with $V_{FM} = 4$ mV (grey curve) and with $V_{FM} = 2$ mV (light green curve). (b) The suspended part of graphene devices C and D is ∼540 nm. The measurements of device C are performed with $V_{FM} = 10$ mV (green curve) and with $V_{FM} = 8$ mV (red curve) . The measurements of device D are performed with $V_{FM} = 10$ mV.

Figure 6.13 summarizes the best Allan deviations we get for different devices. All measurements are performed using the frequency-modulation technique at 4.2 K. Temperature fluctuations are typically ≤5 mK. All measurement parameters (DC gate voltage, driving voltage and frequency deviation) are optimized in order to get the best possible frequency stability for each device. The Allan deviations of device A and device B are shown in Figure 6.13 (a). The devices have a length of around 1 µm. For the shorter devices C and D (length ∼540 nm) we get a slightly lower frequency stability (Figure 6.13 (b)). For device C with the previously extracted effective mass of 2.4±0.6 fg (section 6.4.1) and an Allan deviation of $(3.2\pm0.2)\cdot10^{-5}$ for 0.5 s integration time, we get a mass resolution of 157±41 zg (using equation 5.10). This mass resolution corresponds to the mass of about 131 fullerene molecules and is therefore not sufficient to resolve the mass of a single fullerene molecule. For an integration time of 32 s the mass resolution becomes as low as 49±25 zg. Device C is the only device for which we extract the effective mass experimentally. For this reason the mass resolution we determine for device C is the best estimate.

The mass resolution value for an integration time of 0.5 s is the most relevant since it is in the range of the typical average time (between 0.5 and 1 s) we observe between

the adsorption of singe fullerene molecules (reciprocal value of the adsorption rate). We will see this in section 6.4.3 where we will present experiments on the adsorption of fullerene molecules. In a sensing experiment of fullerene molecules the average adsorption rate therefore defines the maximum integration time we can use in order to improve the frequency stability without integrating over several adsorption events of single molecules.

If we look at the mass resolution previously reported for graphene resonators there are very few experimental results. Chen et al. [41] for example have reported a mass resolution of 2 zg, however they did not estimate the mass resolution from the measured frequency fluctuations, but from the dynamic range. This estimation only holds true when the resonator is only limited by thermal noise [61]. Therefore their estimate does not give a realistic value of the mass resolution as in our case. Resonators made out of single crystal silicon carbide have achieved a mass resolution of 16.6 zg,. In this case the mass resolution was estimated from the experimentally accessed frequency stability [48]. Our results for graphene are comparable to the result reported for silicon carbide beams. Both types of resonators have a comparable surface area (100 to 500 fm^2) for sensing molecules. Moreover, graphene and silicon carbide resonators can be implemented on large scale arranging hundreds of devices in a parallel manner.

6.4.3 Adsorption of fullerene molecules

We carry out adsorption experiments dosing fullerene molecules from the thermal evaporator onto the surface of the different graphene resonators at 4.2 K. We optimize the frequency stability before dosing molecules.

Figure 6.14 (a) shows the example of the Allan deviation of device C just before dosing fullerene molecules. The resonance frequency change upon adsorption of fullerene molecules is shown in Figure 6.14 (b). Here the red arrows indicate when the shutter of the evaporator is opened and closed. The blue curve represents the resonance frequency measured with the computer controlled feedback with the integration time of the lock-in amplifier set at 30 ms. The green curve shows the moving average over 1 s of the resonance frequency data. We can estimate the average frequency shift caused by a single fullerene molecule of mass $m_{C60} = 1.2$ zg to be 59±15 Hz (using $\delta f = \frac{m_{C60}}{2 \cdot 2 \cdot m_{eff}} \cdot f_0$). The resonance frequency fluctuations lie far above the frequency shift of 59±15 Hz that we want to resolve. This is already expected since the frequency stability at 1 s of integration time (Figure 6.14 (a)) corresponds to a mass resolution of 108±29 zg equivalent to the mass of about 90 fullerene molecules.

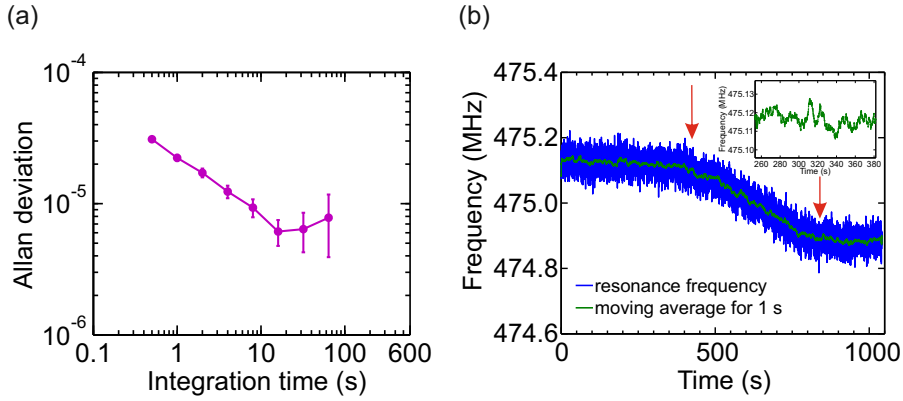

Figure 6.14 – Allan deviation and adsorption experiments on a graphene resonator. (a) Frequency stability of device C measured at 4.2 K and a driving voltage of 10 mV. The corresponding mass resolution of the device for 1 s is 108±29 zg. (b) Resonance frequency of device. Red arrows indicate the time at which the evaporator shutter is opened and closed. Fullerene molecules get evaporated onto the nanotube and the frequency starts shifting. The total shift corresponds to about 3753 molecules. The average shift induced by a single molecule is 59±15 Hz.

6.4.4 Frequency stability limited by the imprecision noise of the detection

Any experimental study of frequency noise in nanoelectromechanical systems leads to the following question: What is the actual limitation of the observed frequency stability of the particular device? The ultimate theoretical limit of the frequency stability is given by the thermal noise, however, as already introduced in chapter 5, this limit was actually never observed experimentally.

We estimate the expected imprecision noise limited Allan deviation (equation 5.7) device D. This allows us to understand whether or not the experimental frequency stability is limited by the imprecision noise of the detection. The noise level is calculated from the off-resonance noise of the resonance response of the mechanical mode (Figure 6.15(a)). We get a noise level of $N_T \approx 0.93\,\mathrm{pA}/\sqrt{\mathrm{Hz}}$. The Q factor is estimated from the fit to be 110. Together with the peak signal level $S = 23.4$ pA we estimate the Allan deviation to be $4.7{\cdot}10^{-5}\,\frac{1}{\sqrt{\tau}}$. This is very similar to the experimental Allan deviation for short τ_A as seen in Figure 6.15 (b). Our comparison indicates that the frequency stability is not limited by the intrinsic fluctuations of the device but rather by the imprecision noise of the read-out itself.

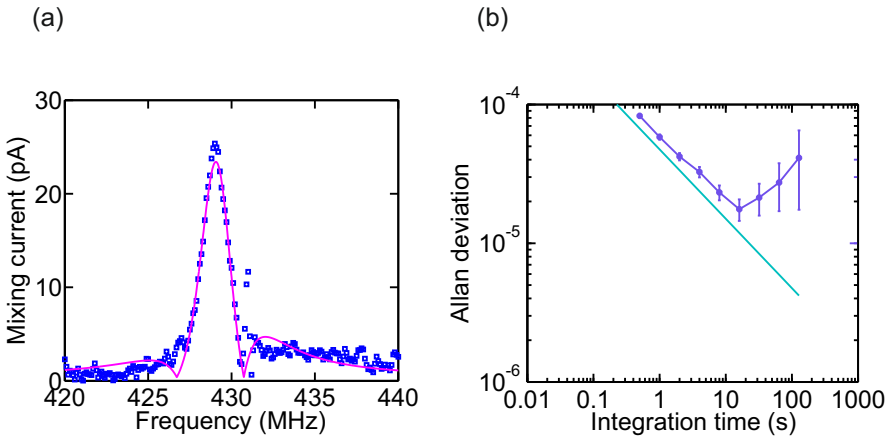

Figure 6.15 – (a) Resonance frequency response of device D measured at 4.2 K with driving voltage of 10 mV. (b) Experimentally measured Allan deviation (violet curve) compared to estimated imprecision noise limited Allan deviation looking at the off resonance noise level in (a).

6.5 Conclusion

In summary, we have fabricated double clamped graphene resonators and studied their frequency stability in order to investigate their performance as mass sensors. To the best of our knowledge we present the first results that give a realistic value of the mass resolution of graphene resonators estimated directly from the measured frequency stability. Our mass resolution is comparable to the one of state of the art silicon carbide resonators.

We have tried to improve the mass resolution of graphene resonators by downscaling the device dimensions. However, the frequency stability could not be improved through the approach of downscaling the device length. We have reached a point where the frequency stability of the devices between 1 μm and 540 nm is not sufficient for the detection of single fullerene molecules. The Allan deviation of the devices is limited by the noise of the read-out system we use to detect the mechanical motion. Additionally, the motion of any shorter graphene resonators could not be detected.

Self-oscillation is a promising approach for graphene resonators as mass sensors. Here, no active driving of the resonator is needed, instead a positive feedback is employed that guaranties the compensation of the energy loss in each oscillation cycle. Self-oscillation with a graphene resonator has already been demonstrated by Chen et al. [27]. The implementation of a self-oscillation scheme that is able to track

the change in the resonance frequency remains a challenging goal since the feedback circuit needs to be continuously adjusted in order to keep self-oscillation.

Overall, the imprecision noise limited frequency stability of the graphene resonators with lengths between ∼540 nm and ∼1 µm and the unresolvable mechanical motion of any smaller devices down to a length of 170 nm suggest that the mechanical motion transduction into a current signal is not sufficiently effective. We suspect that the amplitude of motion of graphene devices with lengths below ∼540 nm is too small to be transduced into a signal large enough to rise above the noise floor. Any future efforts towards improving the mass resolution of graphene based NEMS will require the development of a low-noise transduction technique that (i) no longer limits the frequency stability of the resonator and (ii) allows us to resolve the motion of even smaller graphene resonators. Resolving the motion of smaller resonators that vibrate at higher frequencies, however, always comes with two additional challenges: the need for establishing an impedance matched circuit in order to avoid strong attenuation and the enormously large frequency space needed to be explored in order to locate the mechanical resonance frequency. We took the first step and implemented a low noise read-out, which will be described in the next chapter.

7 Low noise read-out of the resonance frequency of nanotube resonators

Parts of this chapter have been published in:
Improving the read-out of the resonance frequency of nanotube mechanical resonators
J. Schwender, I. Tsioutsios, A. Tavernarakis, Q. Dong, Y. Jin, U. Staufer and A. Bachtold.
Applied Physics Letter 113, 063104 (2018)

7.1 Introduction and motivation

In recent years mechanical nano-resonators have been proven to be exceptional sensors of external forces [5, 7, 8, 137] and adsorption of mass [11, 12, 15]. Mechanical resonators can be used for scanning probe microscopy [138, 139, 140], magnetic resonance imaging [18, 19], mass spectrometry [21] and the study of surface science [56, 62, 115]. This includes the diffusion of adsorbed atoms on the surface of a resonator [62, 141, 142], the formation of monolayers of adsorbed atoms in the solid and liquid phases [56], and phase transitions [115]. Key for all these studies is a low noise transduction of the mechanical motion [143, 144, 145, 146, 147, 148].

Resonators made out of carbon nanotubes hold the records in force and mass sensitivities thanks to their incredible small masses. However, the transduction of the nanotube vibrations into a measurable signal is a challenging task. Because nanotubes are small, the transduced signal is minuscule. Moreover, the read-out scheme has to be compatible with the low-temperature setups used to achieve the highest sensitivities in force [8] and mass [15] detection. Furthermore, electrical transduction schemes are limited by parasitic capacitances from the device pads and cables to the ground, setting a cut-off limit for the read-out frequency typically in the range between 1 and 10 kHz. Efficient read-out was demonstrated by downmixing the high frequency signal of the motion to a low-frequency (1-10 kHz) current modulation using the nanotube as a mixer. At these relatively low frequencies, the current suffers

from large 1/f noise. Moreover, the current amplification took place at room temperature, so that the amplifier noise and the parasitic noise picked up by the cable between the device and the amplifier significantly contribute to the total noise.

In this chapter, we develop an electrical downmixing read-out of nanomechanical motion with reduced noise compared to previous works. It operates at higher frequencies ($\sim$ 1.6 MHz) using an RLC resonator to reduce the typically large output impedance of the nanotube device on the RLC resonance frequency. The current amplification is done with a high electron mobility transistor (HEMT) at liquid helium temperature [149]. This allows the downmixed current from the nanotube to be amplified with minimal additional electronic noise and parasitic noise picked up by the cables. We demonstrate an improved detection of the resonance frequency of carbon nanotube resonators. The frequency stability is no longer limited by additive noise related to the imprecision of the detection, but by noise intrinsic to the device. The intrinsic noise might be due to the diffusion of rest gas molecules.

Observing the intrinsic fluctuations allows us to measure the deterioration of the frequency stability due to xenon atoms on the resonator surface. Additionally, we can now resolve the thermal motion at 4.2 K of carbon nanotubes. In some initial experiments we show first results hinting to the observation of single fullerene adsorption events.

7.2 Low noise read-out implementation

We implement a low noise read out using a RLC resonator and a HEMT that allows to filter and amplify the downmixed signal of a mechanical resonator at low temperature. The details of the circuit around the HEMT and the noise characterization are found in annex A.2.

The RLC resonator is made out of commercial surface-mount components soldered onto a printed-circuit board (PCB). It consists of a resistance of 10 kΩ, an inductance of 33 μH and a capacitance of 200 pF. The resonance properties of the total system (RLC and HEMT) are defined by the resistance at resonance of 6.66 kOhm and a capacitance of 290 pF. The resistance at resonance is given by the parallel resistance of the RLC and the input impedance of the HEMT. It is obtained from the RLC linewidth. The capacitance of 290 pF is attributed to the 200 pF capacitance soldered on the PCB and the capacitance of the radio-frequency cables between the device and the HEMT.

We characterize the noise of the new read-out system at 4.2 K by measuring the

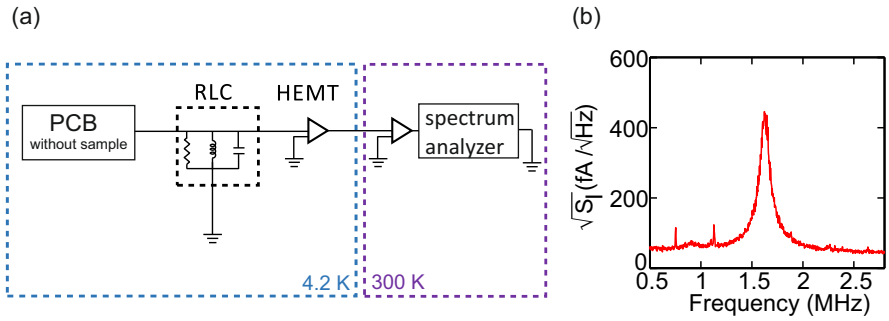

Figure 7.1 – Noise characterization of read-out with RLC and HEMT. (a) Schematic of the setup used to characterize the noise of the combined system of RLC-resonator and HEMT. (b) Current noise spectrum of the RLC resonator at 4.2 K. The peak current noise of 0.43±0.05 pA/$\sqrt{\text{Hz}}$ determines the noise for the detection of the vibrations. The measurement is obtained measuring the thermal noise of the RLC and the HEMT without any nanotube device.

thermal noise of the RLC resonance frequency with the HEMT and an amplifier [1] at room temperature using a spectrum analyzer (see Figure 7.1(a)). The gain of the HEMT is 2.6±0.3; it is estimated from the temperature dependence of the thermal noise. The total noise floor at 4.2 K is 0.43±0.05 pA/$\sqrt{\text{Hz}}$; it is estimated from the noise at the RLC resonance frequency (see Figure 7.1 (b)). This is remarkably low compared to the typical noise level using frequency-modulation mixing (FM) as we will see in section 7.4 [58]. The two main contributions to this low noise floor are the Johnson-Nyquist noise of the total impedance of the RLC resonator (0.18±0.01 pA/$\sqrt{\text{Hz}}$), and the noise picked up at the level of the sample copper box. The sample copper box is connected to the input of the RLC during the noise characterization and partially left open in order to emulate the real experimental conditions when measuring a resonator.

7.3 Fabrication of ultraclean carbon nanotube resonators

The carbon nanotube resonators studied in this chapter were grown on top of the same prefabricated trenches used for the double clamped graphene resonators (see chapter 6.2). This process compared to other top down approaches [15, 38] has the advantage of achieving ultraclean device with pristine properties. In the following we shortly summarize the fabrication procedure.

[1] SA-220F5, Low Noise FET Amplifier, NF Corporation.

For the growth of carbon nanotubes, squared openings of 600 nm x 600 nm are patterned into a PMMA layer on top of the electrodes by electron beam lithography at a distance of 1 µm away from the trenches (Figure 7.2(a-c)). A methanol solution containing iron (Fe) catalyst nanoparticles is then deposited on the substrate (Figure 7.2(d)). After evaporation of the methanol and lift-off of the PMMA in acetone, catalyst nanoparticles remain in the predefined locations (Figure 7.2(e)). The substrate is then transferred into a CVD oven. Here, carbon nanotubes are grown by a decomposition process of methane gas into carbon and hydrogen at the sites where Fe catalyst nanoparticle are located (Figure 7.2(f)). The growth process is performed in a hydrogen (400 mln/min) and argon atmosphere (500 mln/min) at 830 °C for 12 min with a methane flux of 550 mln/min. These parameters result in a high yield of single-walled carbon nanotubes. However, the growth directions are still random and many nanotubes do not cross the trench. For this reason it is important to have a large number of trenches on a single substrate. On each substrate we use, there are 24 trenches. Our yield to get an electrically working suspended carbon nanotube with this method is around 12.5 %. The electrical contact between the electrodes is tested

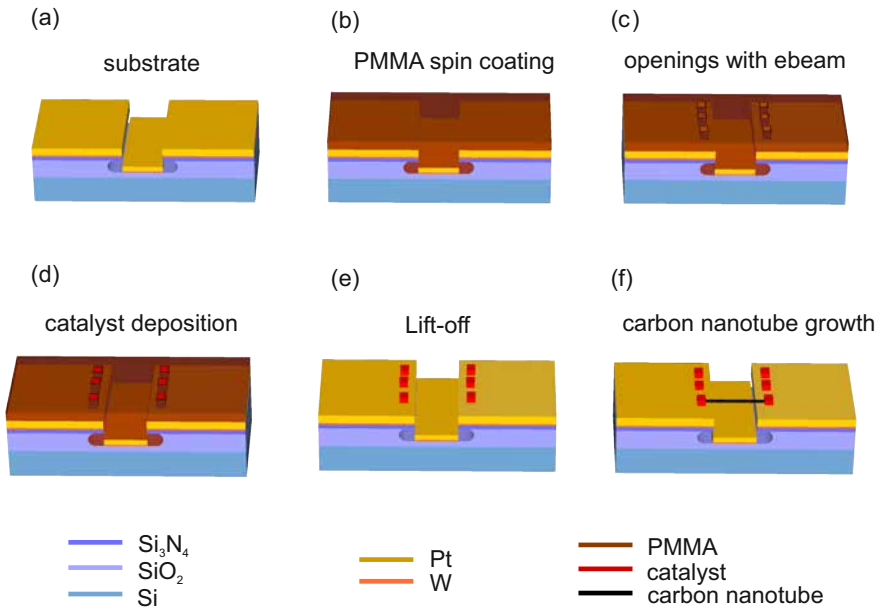

Figure 7.2 – Fabrication process of ultraclean carbon nanotube resonators. (a) Prefabricated substrate with trenches (see chapter 6.2). (b) Spin coating with PMMA. (c) Ebeam lithography to open catalyst sites. (d) Deposition of catalyst particle solution. (e) Lift-off of PMMA that leaves behind catalyst nanoparticles. (e) CVD of carbon nanotubes.

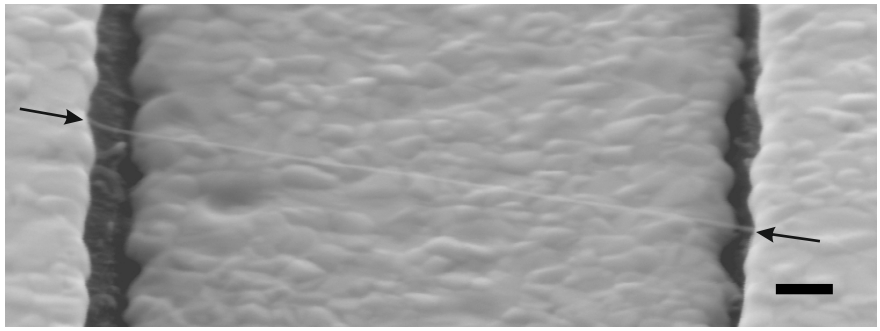

Figure 7.3 – Scanning electron microscopy image of a typical nanotube resonator. The scale bar is 100 nm.

in a probe station after the growth in order to identify the working devices. Scanning electron microscope images (Figure 7.3) are taken only after all experiments as the electron beam contaminates the device with amorphous carbon [150].

7.4 Frequency stability of carbon nanotube resonators

We measured the frequency stability of carbon nanotube resonators. All the measurements were carried out in a homebuilt ultra-high vacuum cryostat [15] at a base pressure of $3{\cdot}10^{-11}$ mbar and 4.2 K (as introduced in chapter 6.3).

The mechanical motion was driven and detected using two different methods as shown in Figure 7.4(c) and (d), often called two-source mixing [40] and frequency-modulation (FM) mixing [58]. The two-source mixing was used together with the low noise read-out setup consisting of the RLC resonator and the HEMT based on an AlGaAs/GaAs heterostructure. The FM mixing is not compatible with the high-frequency of the RLC resonator, but we used it as a benchmark, as it allowed to achieve the best frequency stability of nanotube resonators thus far [15].

Both measurement techniques rely on the nanotube-gate capactitance oscillation generated by the motion of the resonator, which in turn modulates the measured current [20]. The two-source method generates a current directly proportional to the amplitude of mechanical vibrations. By contrast, the current in the FM method is related to the derivative of the real part of the response of the resonator [58]. In both methods, we measured the noise of the resonance frequency by driving the resonator at a setpoint frequency where the slope of the response is highest (Figure 7.4(b)). A change in resonance frequency leads to a change in current. When the

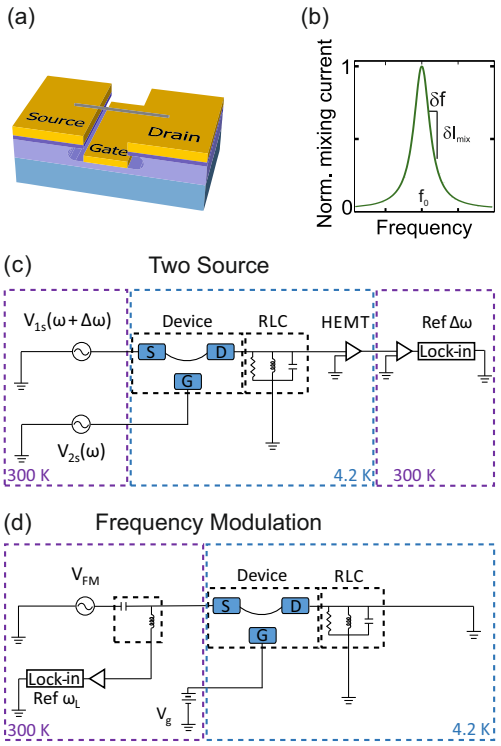

Figure 7.4 – (a) Sketch of the device. The nanotube is contacted electrically to two metal electrodes and suspended over a local gate electrode. The length of the suspended part of the nanotube is ∼1 µm and the distance to the gate is ∼350 nm. (b) Schematic of the read-out of the resonance frequency. Current fluctuations δI_{mix} are translated into frequency fluctuations δf via the slope of the resonance line shape. (c) Two-source setup. We apply an oscillating voltage with amplitude V_{1s} at frequency $\omega+\Delta\omega$ onto the source electrode and an oscillating voltage with amplitude V_{2s} at frequency ω on the gate electrode. We set $\Delta\omega$ equal to the RLC resonance frequency. (d) FM setup. We drive and detect the nanotube vibration in reflection by applying a frequency-modulated oscillating voltage with amplitude V_{FM} onto the source electrode. The reflection measurement allows to switch between the two modes of operation within the same cool down.

resonance frequency drifts more than a certain limit value, we use a computer-controlled feedback loop to correct the driving frequency in order to return to the setpoint for which the slope of the response is highest. The frequency stability is then calculated from the resonance frequency as a function of time using the Allan deviation (equation 5.5, chapter 5.3).

The Allan deviation measured with our new two-source method is significantly better

than the Allan deviation measured with FM (Figure 7.5(a-f)). Both measurements were carried out in the same cool down. The best Allan deviation with the two-source is observed at short integration times τ_A. This is of great interest for mass sensing and surface science experiments when adsorption, desorption, and diffusion processes are rapid. The Allan deviation with the two-source is independent of S, that is, the voltage amplitude V_{2s} applied to the gate (driving force). This indicates that the Allan deviation is limited by the noise of the resonance frequency of the nanotube resonator. The imprecision noise of the detection is irrelevant, since the corresponding Allan deviation is expected to be about two orders of magnitude smaller than the measured Allan deviation. The expected Allan deviation is $5.2{\cdot}10^{-7}$ for an integration time $\tau_A = 1\,\mathrm{s}$ using equation 5.7 with N_T=0.43 pA/$\sqrt{\mathrm{Hz}}$.

By contrast, the Allan deviation measured with FM is given by the imprecision noise of the detection at low τ_A. The Allan deviation scales as $1/\sqrt{\tau_A}$ and gets larger for lower S, as expected from equation 5.7. The measured Allan deviation is consistent with what is expected from the imprecision noise N_T, since we obtain $N_T = 18\,\mathrm{pA}/\sqrt{\mathrm{Hz}}$ from the measured $\sigma_{\mathrm{Allan}}(\tau_A)$ (dotted line in Figure 7.5(f)) and equation 5.7, which is comparable to $N_T = 16\,\mathrm{pA}/\sqrt{\mathrm{Hz}}$ estimated from the off-resonance current fluctuations observed in Figure 7.5(b). At long τ_A, the Allan deviation becomes similar to the Allan deviation measured with the two-source (Figures 7.5(e,f)). This indicates that the Allan deviation becomes limited by the noise of the resonance frequency of the nanotube resonator.

The $\sigma_{\mathrm{Allan}}(\tau_A)$ curves measured on three different devices with the two-source are similar (Figures 7.5(e), 7.6(a,b)). This indicates that the physical origin of the noise of the resonance frequency is the same for the three devices. The Allan deviation reaches $\sim 10^{-5}$ at 125 ms integration time. Comparing Allan deviation measurements to power law dependences, $\sigma_{\mathrm{Allan}} \propto \tau_A^{\alpha}$ allows to gain insight into the noise mechanisms behind. In our case, the exponent α approaches $\sim 1/4$. The positive slope of $\sigma_{\mathrm{Allan}}(\tau_A)$ plotted in a doubly-logarithm scale is often attributed to the drift of the resonance frequency due to the slow variations of the temperature and the voltage applied to the device. We characterized the fluctuations of the temperature, the static voltage applied to the gate electrode, and the amplitude of the high-frequency voltages applied to the device. These fluctuations correspond to Allan deviations that are between one and three orders of magnitude smaller than that measured in our devices (see section A.1). Therefore, the origin of the Allan deviation is not related to the drift of the temperature and the applied voltages.

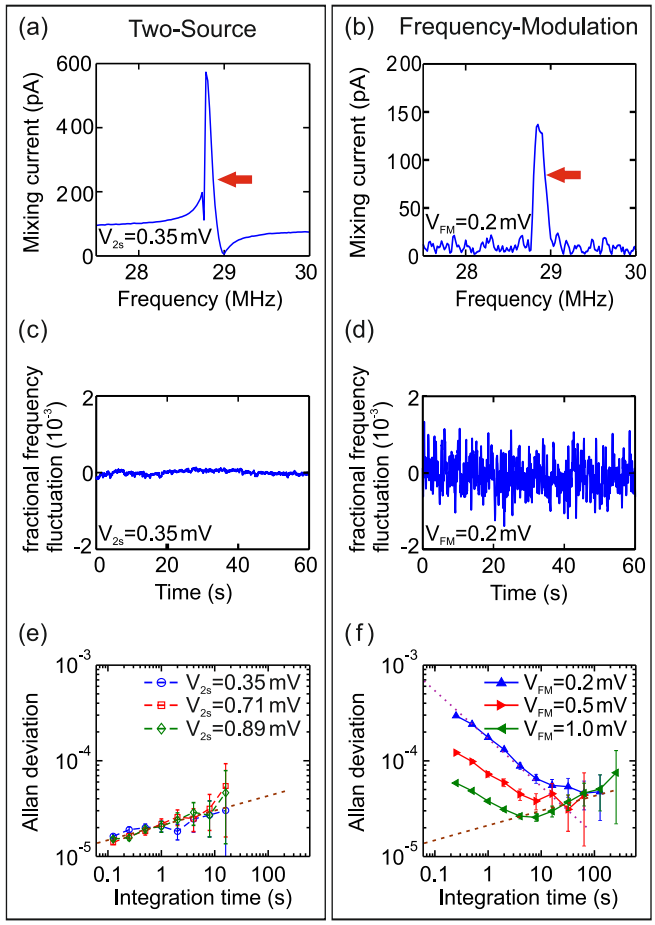

Figure 7.5 – (a) Response of the nanotube device 1 to the driving frequency at 4.2 K using the two-source setup. The large off-resonance current has a purely electrical origin [40]. (b) Response of the nanotube resonator to the driving frequency at 4.2 K using the FM setup. The integration time of the lock-in amplifier is 100 ms. The red arrows in (a) and (b) indicate the slope used to measure the fluctuations of the resonance frequency. (c,d) Fractional frequency fluctuation $\delta f_0/f_0$ of the resonator measured with the two-source setup and the FM setup. Here δf_0 is the measured deviation of the resonance frequency at time t with respect to the average resonance frequency f_0. (e) The frequency stability of the mechanical resonator measured with the two-source setup for different drives. The brown dashed line is a guide to the eye showing the trend of the Allan deviation as a function of the integration time. (f) The frequency stability of the mechanical resonator measured with the FM setup for different drives. The data at low integration time are compared to Eq. (5.7) (purple dotted line). The brown dashed line indicates the trend of the Allan deviation measured with the two-source setup in (e).

7.5 Frequency stability upon adsorption of xenon

In order to probe the sensitivity of the frequency fluctuations and work towards understanding their origin, we carried out adsorption experiments

Figure 7.6(b) shows how the Allan deviation is modified after having adsorbed a small number of xenon atoms onto the nanotube. The xenon atoms were administered through a small nozzle into the ultra-high vacuum cryostat. When impinging on the nanotube they have a certain sticking probability due to unspecific physisorption. From the shift of f_0, the number of xenon atoms is estimated to be 1.0 % of the total number of carbon atoms in the suspended portion of the nanotube [56, 115]. The presence of these xenon atoms significantly deteriorates the frequency stability of the device. The Allan deviation increases by a factor ~ 3 over the whole range of integration time. The deterioration of the frequency stability is attributed to the diffusion of xenon atoms over the surface of the nanotube, as reported in Ref. [62]. The reduced frequency stability is not related to adsorption/desorption processes, since the Allan deviation does not return to its initial value before the exposure to xenon while the measured pressure of the chamber does.

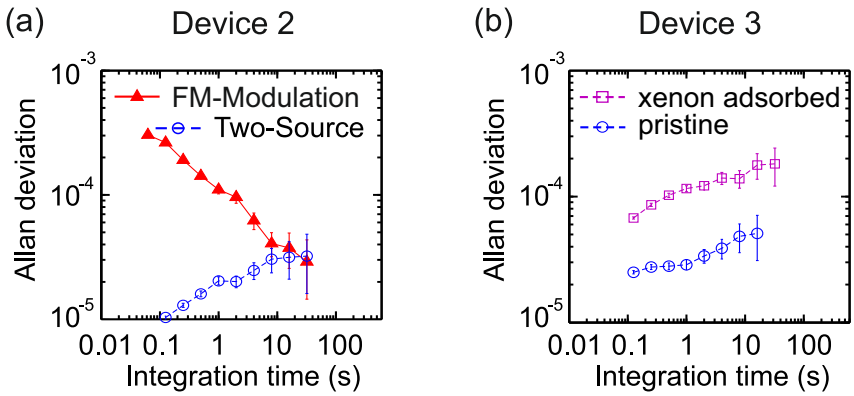

Figure 7.6 – (a) The frequency stability of device 2 measured with the FM setup and the two-source setup. The FM measurement was performed with V_{FM}=0.2 mV and the two-source measurement with V_{2s}=0.007 mV. (b) The frequency stability of device 3 with and without xenon atoms adsorbed onto the nanotube. Both measurements were performed with V_{2s}=0.071 mV.

The slope of $\sigma_{\mathrm{Allan}}(\tau_A)$ plotted in the doubly-logarithm scale is positive with or without the adsorption of xenon atoms. This suggests that the frequency stability of our devices without adsorbed xenon in Figs. 7.5(c) and 7.6(a,b) is also limited by the diffusion of adsorbed atoms and molecules. These particles might come from the rest gas

in our ultra-high vacuum setup, such as H_2, H_2O, CO, and CO_2. Our measurements are somewhat consistent with the model based on the diffusion of non-interacting particles, which predicts a positive slope. The noise due to diffusion is discussed in detail in the supplemental information of Ref. [62]. The typical exponent measured in our work is about half the value expected from this simple model where trapping of particles at defect sites and particle-particle interaction are both disregarded. A more complete characterization of the physics of the frequency stability of nanotube resonators will require further work in the future.

7.6 Mass resolution and fullerene sensing

The improvement of the read-out noise was motivated by pushing the mass sensing performance of carbon based resonators. Here we used carbon nanotubes as mass sensors. For this we first estimated their mass resolution from the frequency stability measurements and then carried out adsorption experiments with fullerene molecules.

The mass resolution of device 2 is as low as 0.12 ± 0.05 zg. This mass resolution is comparable to the mass of one fullerene molecule. It is extracted from the Allan deviation for 1 s of integration time (using equation 5.10)determined from the frequency fluctuations before dosing fullerene molecules (Figure 7.7 (a)). Here the effective mass is calculated from equation 3.41, since the device was observed to be under tension. The mass of the resonator is taken as the mass of a pristine carbon nanotube of length 1±0.1 µm and a diameter of 1.5±0.3 nm ($m_{\mathrm{pristineNT}} = 3.6 \pm 0.2$ ag).

Figure 7.7 (b) shows the measurements where we dosed fullerene molecules onto the nanotube and observed the frequency shifting down. We see some steps in the change of the resonance frequency, however, they can not be clearly differentiated from the level of noise. These step-like shifts might come from the adsorption of single fullerene molecules, since the mass of a single fullerene molecules leads to an average shift in frequency for this device of 5.2±2.2 kHz (using $\delta f = \frac{m_{\mathrm{C60}}}{2 \cdot 2 \cdot m_{\mathrm{eff}}} \cdot f_0$). This result shows that the observation of clear single fullerene molecule adsorption events on top of an ultraclean carbon nanotube resonator still remains a challenging task.

7.7 Conclusions

In conclusion, we implemented an electrical downmixing read-out scheme of nanomechanical motion using a RLC-resonator as a filter together with a high electron mo-

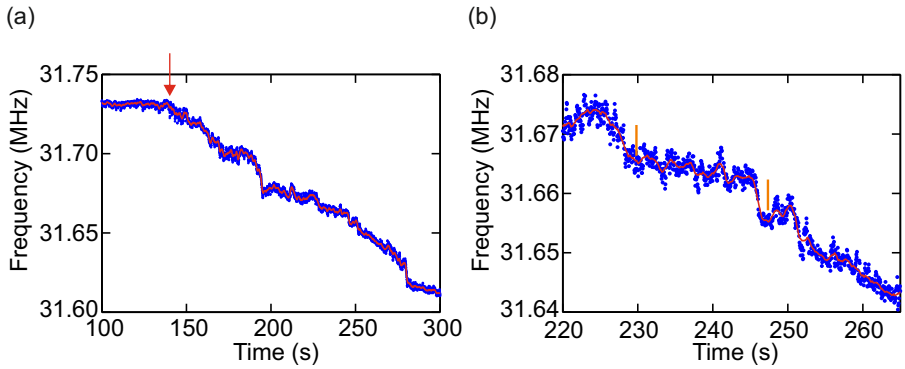

Figure 7.7 – (a) The resonance frequency of device 2 at 4.2 K as a function of time as fullerene molecules are being dosed. The red trace is the moving average for an integration time of 1 s of the experimental data (blue dots). The red arrow indicates the point in time where the dosing starts. The frequency stability before dosing molecules is $2.9{\cdot}10^{-5}$ for an integration time of 1 s. (b) Detailed view of a small part of (a). Here we see shifts in the resonance frequency consistent with the adsorption of single fullerene molecules (indicated by the orange vertical lines).

bility transistor as a low-temperature amplifier. The noise floor of the read-out is remarkably low and can resolve the thermal motion of the nanotube (see annex A.3). This scheme allows us to measure the frequency stability of nanotube mechanical resonators with an unprecedented quality and a mass resolution equivalent to 0.12±0.04 zg. The frequency noise measured at 4.2 K is limited by the resonator itself, and not by the imprecision of the measurement. The origin of the frequency noise might be related to the diffusion of atoms or molecules over the surface of the nanotube. Our new detection method allowed us to perform preliminary experiments hinting to the observation of single molecule adsorption. It holds promise for studying the diffusion of atoms and molecules over crystalline surfaces [62], the interplay between particle diffusion and mechanical vibrations [141, 142], and the phase transition in monolayers of adsorbed atoms [56, 115]. All in all, the results present an important tool for future work related to the understanding of frequency fluctuations in carbon nanotube resonators.

8 Conclusion and Outlook

Within the scope of this thesis we studied graphene and carbon nanotube mechanical resonators with a focus on their mass sensing performance. This work was motivated by the tremendous improvements made over the last decades in the mass resolution of NEMS based mass sensors. These improvements were possible thanks to the miniaturization of the device dimensions but also thanks to the improvement of the transduction of the mechanical motion. Today, despite all the efforts put into the implementation of new efficient read-out techniques, the mass sensing performance of NEMS remains limited by the read-out instrumentation and the frequency fluctuations related to the interaction of the devices with its environment.

In this thesis, we followed two different approaches towards achieving the ultimate mass sensing performance of carbon based NEMS. We tried in a first step to see how far we can push the mass sensing performance of graphene resonators. Then in a second step, we concentrated on improving the noise performance of the electrical downmixing read-out scheme with carbon nanotube resonators.

In the first part of this thesis we reduced the dimensions of graphene resonators down to the submicron level and measured their frequency stability. This allowed us to get a first realistic estimate of the mass resolution of graphene resonators. However their mass resolution is not improved compared to state of the art silicon carbide resonators. The frequency stability is limited by the imprecision noise of the read-out rather than by the thermomechanical noise of the device itself or by intrinsic noise processes. This is why we could not resolve the motion of graphene nanomechanical resonators with dimension below 600 nm.

In the second part of the thesis we therefore tackled the performance limitation of carbon-NEMS based mass sensors from a different angle: we focused on improving the transduction of the mechanical motion. We implemented an electrical read-out scheme that allows to detect the mechanical resonance of carbon nanotubes with an unprecedented quality down to the level where the nanotubes resonance

frequency stability is no longer limited by the imprecision of the detection but rather by frequency fluctuations intrinsic to the device. Our new setup shows an improved frequency stability at low integration times compared to standard low noise mixing techniques. The frequency fluctuations are quite likely related to the diffusion of unwanted molecules and atoms on the surface of the resonators that come from the rest gas present in the UHV.

In conclusion, the mass resolution of the ultimate two-dimensional resonators based on graphene still remains limited by the imprecision of the detection. In the future it would be interesting to see if the low noise read-out allows to observe the intrinsic fluctuations of graphene resonators and moreover if it enables to resolve the motion of shorter graphene resonators. Besides, it will be interesting to study mass sensing with graphene resonators fabricated from CVD graphene for large scale integration. However, the contamination of graphene based nanomechanical resonators remains an issue and affects the reproducibility and limits the use of graphene for surface science studies. No matter if working with exfoliated graphene or CVD based graphene cleaner fabrication methods should be employed in the future. The use of a dry transfer technique could be an option [151].

In the second part of this thesis, intrinsic frequency fluctuations of carbon nanotube resonators became experimentally accessible thanks to the low noise read-out implemented as a part of this thesis. This result offers an experimental platform that opens up many possibilities for future experiments. Examples are the study of diffusion of atoms and molecules over crystalline surfaces [62], the interplay between particle diffusion and mechanical vibrations [141, 142], and the phase transition in monolayers of adsorbed atoms [56, 115].

The new read-out scheme opens up the possibility to perform measurements of the mechanical motion at time scales down to the level of μs in future experiments. This can be of considerable interest for a variety of experimental studies. It can be used for mass sensing experiments with carbon based NEMS with faster time resolution. Our new detection scheme may allow to implement self-oscillation with an active feedback with carbon based resonators without the need of a direct read-out scheme or parametric amplification [97].

A new research direction in the area of carbon based resonators could rely on strain engineering. Uniaxial strains in graphene have been predicted to change the diffusion mechanism of hydrogen atoms on the surface [152]. A complex device design based on a tensile-MEMS has already demonstrated to achieve large strains in suspended graphene [153]. The advantage of this design compared to the use of an electrostatic field to induce strain is that it is able to reach much larger values of strain without

affecting the signal amplitude (via the transconductance). The implementation of such a device could provide a new experimental platform to study the strain dependence of diffusion mechanisms by monitoring the frequency stability.

A Additional information on chapter 7

A.1 Quantification of noise sources

We quantify the Allan deviation associated to the fluctuations of the temperature as follows. We measure the resonance frequency f_0 as a function of temperature T, yielding -2775 Hz/K for the $f_0 - T$ conversion at 4.2 K. We separately measure the temperature fluctuations by recording the temperature as a function of time at 4.2 K. We calculate the time trace of the corresponding resonance frequency using the measured $f_0 - T$ conversion. We compute the associated Allan deviation (Figure A.1).

The Allan deviation associated to the fluctuations of the voltages applied to the device is obtained in a similar way. The $f_0 - V_g$ conversion between the resonance frequency and the gate voltage is 12.1 MHz/V. From the measured time trace of the voltage delivered by our voltage source, we compute the associated Allan deviation (Figure A.1). In addition, we measure the time trace of the amplitude V_{1s} of the oscillating voltage bias applied across the nanotube. Using the relation $[\delta I_{mix} = I_{mix} \cdot \frac{\delta V_{1s}}{V_{1s}}]$ between the fluctuations of the mixing current δI_{mix} and the fluctuations δV_{1s}, and using the slope of the measured I_{mix} as a function of the driving frequency in Figure 7.5 (a) of the main text, we compute the associated Allan deviation.

Figure A.1 shows that the Allan deviation measured in the device 1 is not related to the drift of the temperature and the applied voltages.

A.2 HEMT implementation and characterization

In this section we present the implementation of the RLC and the high electron mobility transistor. Moreover, we explain in more detail the modelling and the noise characterization of the circuit containing the RLC and the HEMT.

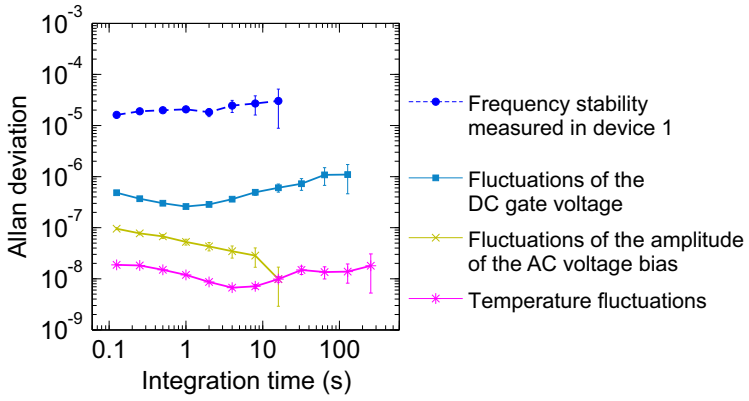

Figure A.1 – Allan deviation measured in device 1 compared to the Allan deviation estimated from measured temperature fluctuations and measured voltage fluctuations.

High electron mobility transistor amplifier and RLC resonator

The high electron mobility transistor is based on a two-dimensional electron gas formed at the interface of a AlGaAs/GAs heterostructure grown by molecular beam epitaxy [149]. It is implemented as the active element into an amplifier circuit [154]. Both, the HEMT and the amplifier circuit is provided by our collaborators Quan Dong and Yong Jin (Centre de Nanosciences et de Nanotechnologies, CNRS, Univ. Paris-Sud). The circuit is composed of the HEMT and several passive elements including commercial surface mount resistors and capacitors. All components are glued with UHV compatible epoxy[1] onto a previously fabricated PCB[2]. A schematic of the circuit is shown in Figure A.2. The capacitors and the resistances in the circuit serve as filters. The capacitors and resistors used in the circuit set and stabilize the polarization of the HEMT. The HEMT is polarized at V_{dd} and V_{s}. The AC signal filtered by the RLC resonator enters the amplifier circuit at the gate of the transistor. The signal is amplified by a factor G_{HEMT} when leaving the circuit at the drain voltage V_{d}. The factor G_{HEMT} is known as the gain of the amplifier. The active element, the transistor, in the linear regime can be seen as a system with a variable resistor that is controlled via V_{gs}. The gain G_{HEMT} strongly depends on the operating point of the transistor.

The parallel RLC resonator is fabricated with surface mount components on another PCB[2]. It consists of a resistor of 10 kΩ, an inductor of 33 µH and a capacitor of 200 pF. The components and SMA connectors are also fixed to the PCB with UHV compatible

[1] EPO-TEK H20E, Epoxy Technology

[2] Novatek, double sided, dielectric: Rogers RO3003 (0.8 mm), base copper thickness: 35 µm, surface finishing: chemical golden.

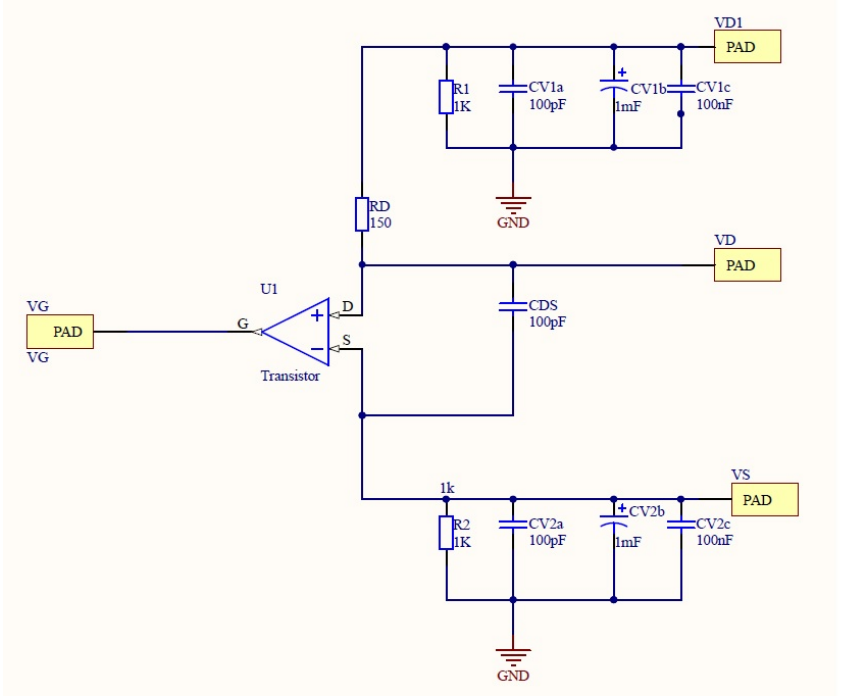

Figure A.2 – . Schematic of the circuit of the HEMT with all components. The references of the components can be found in [154]. Courtesy of Quan Dong and Yong Jin, Centre de Nanosciences et de Nanotechnologies, CNRS, Univ. Paris-Sud.

epoxy. Figure A.3 shows the back side of the cold finger of the cryostat where the two boxes containing the RLC and the HEMT are mounted. The output of the RLC is connected with the gate of the transistor by SMA connectors.

Noise characterization

A schematic of the system with its different noise contributions is shown in Figure A.4. We model the system of the RLC and the HEMT amplifier as a system with a total impedance Z_{tot} defined by the resistance of the RLC in parallel with the finite input impedance of the HEMT. The input impedance is finite due to the Miller capacitance of the amplifier. The Miller capacitance is related to the capacitance between the input and the output of the amplifier. The resistance of the RLC is given by the surface mount resistor and is 10 kΩ. The contribution of the resistance r of the inductor, L, of the RLC resonator is negligible compared to Z_{tot} since at low temperature it is measured to be below 1 Ω. Since we work in the MHz regime $r \ll L\Omega$. The fact that

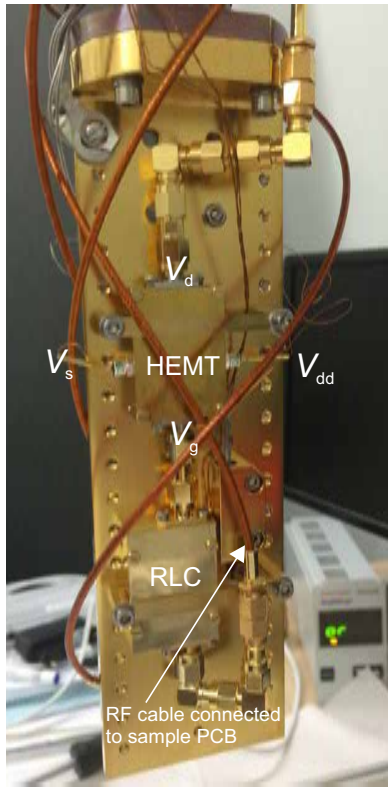

Figure A.3 – Backside of the cold finger of the cryostat with RLC and HEMT mounted.

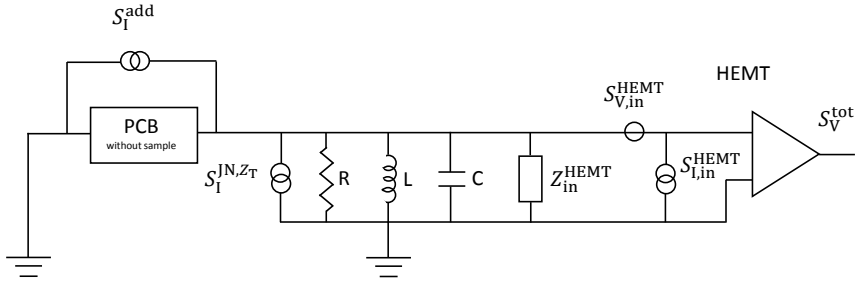

Figure A.4 – Schematic of the low noise read-out system with its different noise contributions. The different noise sources are the thermal noise of the total impedance of the system, additional current noise picked up at the level of the sample copper box, the input current noise of the HEMT and the input voltage noise of the HEMT.

$r < \Omega$ and $r \ll L\Omega$ allows to describe the power spectral density of the thermal noise of the combined system of the RLC and the HEMT by the following equation [154]:

$$S_V^{JN} = \frac{G_{HEMT}^2 4 k_B T \Re\{Z_{tot}\}}{1+4(\Re\{Z_{tot}\}C)^2 4\pi^2 (f-f_0)^2}, \tag{A.1}$$

where G_{HEMT} is the gain of the HEMT for a specific operating point.

We chose an operating point with a low noise. We work at a drain source voltage difference of 100 mV and a current of $I_{ds} = 1$ mA at 4.2 K. The voltages applied to the polarisation inputs V_{dd} and V_s of the HEMT are consequently set to 325 mV and 68 mV respectively. We measure the power spectral density response at 4.2 K with a spectrum analyzer. Fitting this response with the following equation:

$$S_V^{JN} = \frac{2A}{\pi \Delta f} \frac{1}{1+4(f-f_0)^2/\Delta f_0^2}, \tag{A.2}$$

allows to extract the capacitance C from the resonance frequency $f_0 \approx 1.63$ MHz of the RLC and the inductance of 33 µH using $C = \frac{1}{4\pi^2 f_0^2 L}$. The real part of the total impedance $\Re\{Z_{tot}\}$ is obtained from the linewidth Δf_0 (full width at half maximum) of the resonance response of the RLC using $\Re\{Z_{tot}\} = \frac{1}{2\pi \Delta f_0 C}$. This last equation can be derived from the equation valid for the Q factor of an RLC, which is $Q = \Re\{Z_{tot}\}\sqrt{\frac{C}{L}}$. We get a capacitance of 290 pF and a total impedance of around 6.66 kΩ. The capacitance is higher than the 200 pF surface mount capacitance. The additional capacitance comes from the radio frequency cables that are needed to connect the sample to the RLC-resonator and from the Miller capacitance of the HEMT. The offset of the Lorentzian response from the zero noise level is due to the input voltage noise of the HEMT. It is determined to be $\sqrt{S_{V,in}^{HEMT}} \approx 330\,\text{pV}/\sqrt{\text{Hz}}$. A schematic of the response and its different contributions is shown in Figure A.5(a).

The Johnson-Nyquist noise given by $G_{HEMT}^2 4 k_B T \Re\{Z_{tot}\}$ can be determined from the area under the Lorentzian A and the linewidth Δf_0 using the following equation: $\frac{2A}{\pi \Delta f_0}$. We measure the resonance response with the spectrum analzyer up to 15 K. Any change in the gain and in the linewidth is negligible within the temperature range of the measurement. Figure A.5 (b) shows the normalized area under the Lorentzian as a function of temperature. The red trace constitutes a linear fit to the data. The slope of the linear fit gives an estimate of the gain of the HEMT ($G_{HEMT} = \sqrt{slope}/\sqrt{4 k_B T \Re\{Z_{tot}\}} = 2.6 \pm 0.3$). The intercept at 0 K describes the voltage noise originating from the input current noise of the HEMT $S_{I,in}^{HEMT}$ and any additional current noise (S_I^{add}) picked up at the level of the sample copper box ($\sqrt{S_{I,in}^{HEMT} + S_I^{add}} = \sqrt{intercept}/(G_{HEMT}\Re\{Z_{tot}\})$). The normalized area under the Lorentzian is given

by the following equation:

$$\frac{A}{\Delta f_0} = \frac{\pi}{2} G_{\mathrm{HEMT}}^2 [4k_{\mathrm{B}} T \Re\{Z_{\mathrm{tot}}\} + (S_{\mathrm{I,in}}^{\mathrm{HEMT}} + S_{\mathrm{I}}^{\mathrm{add}}) \Re\{Z_{\mathrm{tot}}\}^2]. \tag{A.3}$$

The noise of interest is the total on resonance current noise since it defines the measurement noise when we measure the mechanics of a resonator at 4.2 K. The total on resonance current noise at the level of the device is the noise before any amplification and conversion from a current into a voltage that we measure at the output of the HEMT. It can be calculated from the on resonance voltage noise $S_{\mathrm{V}}^{\mathrm{tot}}(f_0)$ measured at the output of the HEMT (see Figure A.4) given by:

$$S_{\mathrm{V}}^{\mathrm{tot}}(f_0) = G_{\mathrm{HEMT}}^2 [4k_{\mathrm{B}} T \Re\{Z_{\mathrm{tot}}\} + (S_{\mathrm{I,in}}^{\mathrm{HEMT}} + S_{\mathrm{I}}^{\mathrm{add}}) \Re\{Z_{\mathrm{tot}}\}^2 + S_{\mathrm{V,in}}^{\mathrm{HEMT}}]. \tag{A.4}$$

The on resonance current noise at the level of the sample then becomes:

$$\sqrt{S_{\mathrm{I}}(f_0)} = \sqrt{\frac{S_{\mathrm{V}}^{\mathrm{tot}}(f_0)}{G_{\mathrm{HEMT}}^2 \Re\{Z_{\mathrm{tot}}\}^2}}, \tag{A.5}$$

The resonance response of the RLC at 4.2 K at the level of the sample expressed

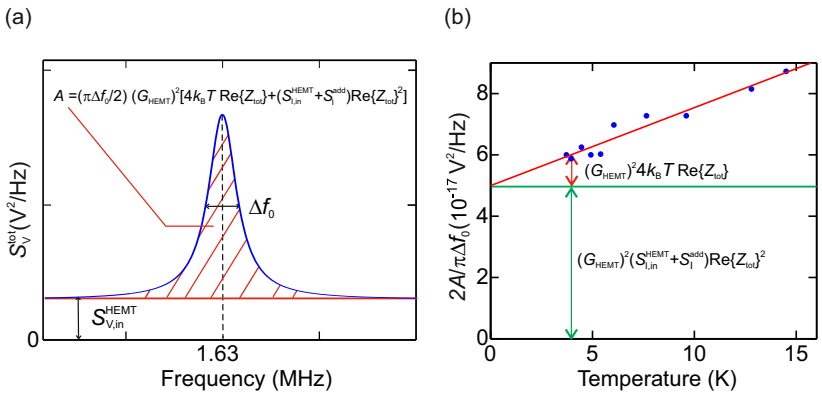

Figure A.5 – (a) Schematic of the power spectral density of the total voltage noise measured at the output of the HEMT. It shows the Lorentzian response of the RLC resonator. (b) Temperature dependence of the voltage noise measured at the RLC resonance frequency. The red trace is a fit to the experimental data obtained by fitting the measured response to a Lorentzian (blue dots). The uncertainty of the Lorentzian fits is smaller than the size of the data points and therefore neglected in the graph. The noise at 0 K originates from the input current noise of the HEMT and any additional noise picked up by the sample box.

in units of pA/$\sqrt{\text{Hz}}$ is shown in Figure 7.1 (b). The on resonance noise level then becomes $\sqrt{S_I(f_0)} = 0.43 \pm 0.05\,\text{pA}/\sqrt{\text{Hz}}$ as already discussed in section 7.2.

A.3 Thermal vibration detection

Our implemented detection scheme with the RLC and the HEMT allows to resolve the thermal motion of carbon nanotube resonators. Figure A.6 shows the power spectral density of the current fluctuations of device 3 measured with the RLC and the HEMT. In the absence of any applied oscillating voltage to the nanotube we see the pure background of the thermal noise of the RLC resonator (blue trace). Here we only show the spectrum around the resonance frequency of the RLC. The thermal motion of the device is observed applying an oscillating voltage to the source of the device at an offset of ~1.563 MHz compared to resonance frequency of the device (green trace). The offset is chosen slightly below the resonance frequency of the RLC in order to visualize the thermal motion better. The measurement is very similar to the noise measurement technique described in chapter 4.2.2.2. Also here the detection relies on the capacitance modulation induced by the thermal motion of the

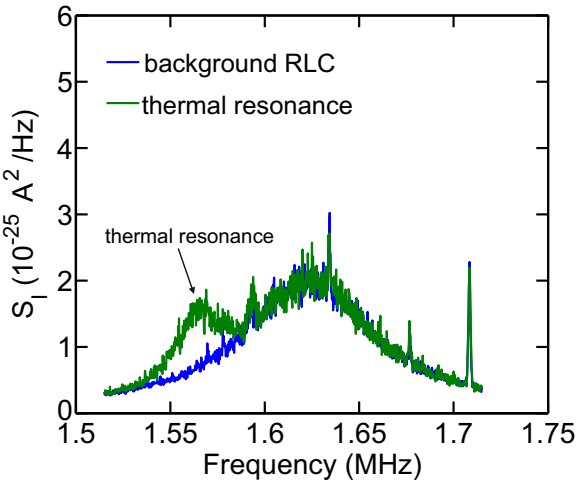

Figure A.6 – Thermal vibration of a carbon nanotube resonator measured at 4.2 K. The blue trace indicates the background noise of the RLC, measured when no signal is applied to the nanotube. The green trace shows the thermal resonance on the left hand. It is read-out applying a voltage at the source of the nanotube with an offset of ~1.563 MHz compared to the resonance frequency of the nanotube. The offset is chosen slightly below the resonance frequency of the RLC in order to visualize the thermal motion better.

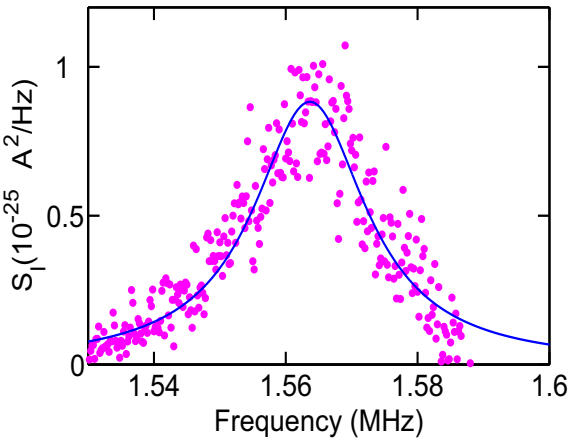

Figure A.7 – Spectrum of the current noise of the thermal vibration at 4.2 K.

resonator which in turn modulates the conductance, so the current noise measured at the drain. The imprecision noise given by the thermal noise of the RLC can be subtracted from the measurement of the thermal motion of the resonator in order to confirm the lorentzian nature of the response (see Figure A.7). These preliminary results show that the detection of the thermal motion is possible. However, future experiments should be dedicated to a detailed characterization of the thermal noise spectrum in order to show that its temperature dependence can be described by the equipartition theorem. These measurements would then also allow to extract the effective mass of the device experimentally and understand at which temperature the device thermalizes. For this study the quality-factor of the device we measured is not sufficient since it does not exhibit a linewidth which is sufficiently smaller than the linewidth of the RLC and can therefore only be visualized off the RLC resonance where filtering of the signal is no longer neglegible.

B Fabrication of graphene drum resonators

In the scope of this thesis, downscaling the device dimensions of graphene resonators was one of the main efforts. In this context we worked not only on double clamped geometries as presented in chapter 6, but also on drums.

Working with a drum geometry has two main advantages over a double clamped geometry: drum resonators have well defined mode shapes since they do not posses unclamped edges. This can be important for the reliability and reproducibility of one single device and from device to device. Apart from this, drums typically exhibit higher Q-factors compared to double clamped geometries. Their Q-factors also decrease with decreasing size [155]. In double clamped geometries the edge modes can lead to unwanted dissipation [156]. Both high Q-factors and well defined mode shapes are crucial for the mass sensing performance of NEMS.

We developed a new fabrication process that allowed us to achieve small (d≈300 nm) graphene drum resonators with a local gate. The devices showed reasonable resistances and transconductances, however we were not able to detect their mechanical motion. In the following we explain the fabrication process in detail.

The process flow of the fabrication is summarized in Figure B.1. For this we start off with a high resistive Si substrate covered with a 442 nm thick layer of thermally grown SiO_2. We then define the structure for the local gate contacts and alignment marks by electron beam lithography, metal deposition (Cr 1 nm, Au 45 nm) and lift-off. In order to clean the sample from any PMMA residues for further processing, we perform an oven annealing at 240 °C in a hydrogen and argon atmosphere. The hydrogen flux is 500 mln/min and the argon flux is 500 mln/min as well. We then grow a 50-60 nm thick layer of Aluminium oxide via atomic layer deposition. The temperature during the deposition is 150 °C and the puls lengths of the H_2O precursor and the TMA precursor are 0.03 s. The resulting layer thickness is measured with an ellipsometer and confirms the growth rate of 1.31 Å/cycle. In a second ebeam lithography step we pattern circular holes with a diameter of 300 nm on top of the local gate electrodes

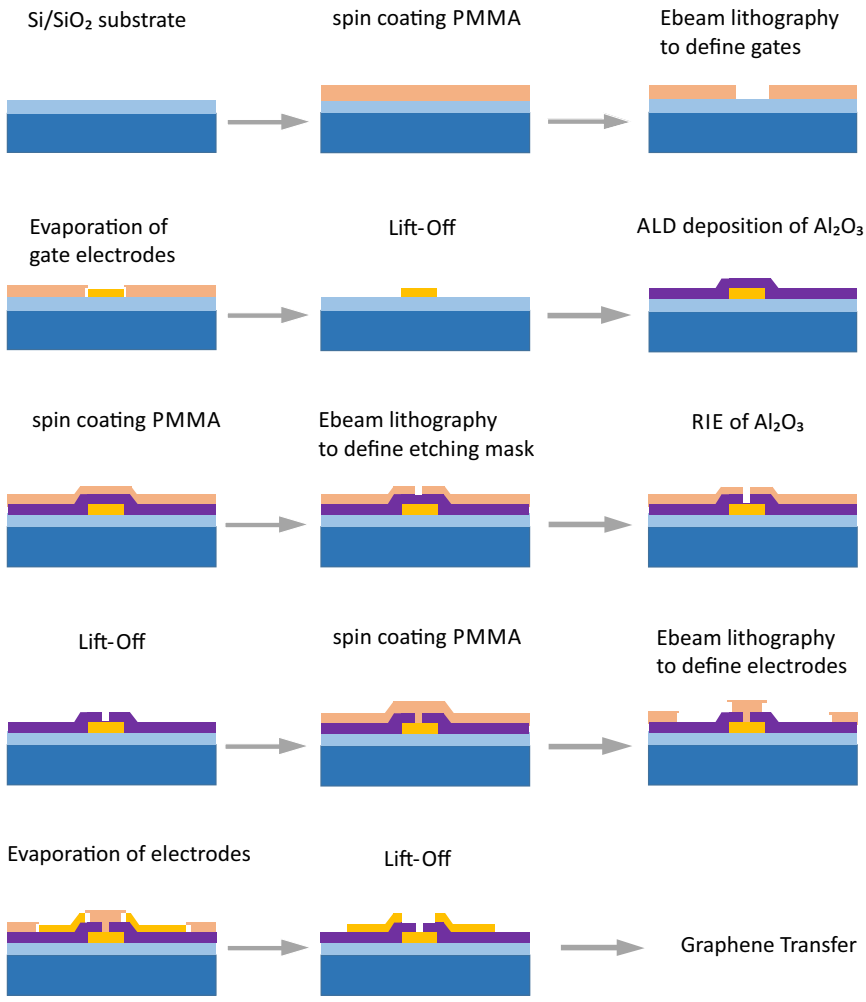

Figure B.1 – Process flow of the fabrication of drum resonators.

covered with aluminum oxide. The final depth of the holes is about 50 nm. We then inspect the drum structure with the AFM in order to identify dimensions, profile and look for possible contamination. In the case of contamination caused by the reactive ion etching, we clean the sample in an oxygen plasma. In a last ebeam lithography step we pattern source and drain electrodes that end at a distance of 1 µm away from the drums. The ebeam lithography step is followed by metal evaporation (Cr 1 nm, Au 45 nm) and lift-off. Afterwards another oven annealing is performed to

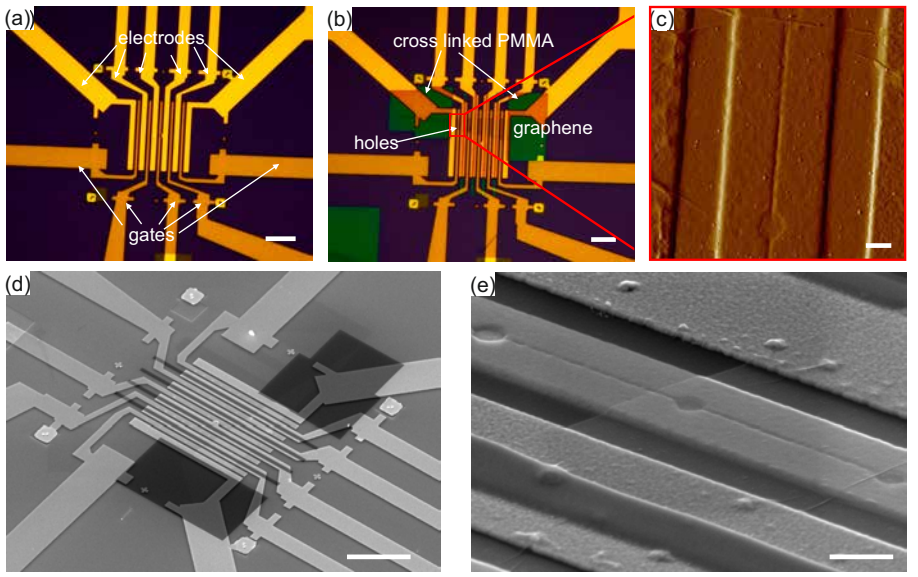

Figure B.2 – Optical microscope images of the device before (a) and after the graphene transfer (b). The scale bars are 10 µm. (c) Atomic force microscope image of a graphene drum device. The graphene flake becomes nicely visible on the structure where it forms wrinkles. The scale bar is 300 nm. (d) Scanning electron microscope image of the device after the graphene transfer. The scale bar is 15 µm. (e) Scanning electron micrograph of the graphene drum device seen in (c). The scale bar is 500 nm.

remove residual ebeam resist. An optical image of the final device can be seen in Figure B.2 (a). On these structures we then transfer narrow (2 µm) graphene flakes with the same method that we used for the double clamped graphene resonators. The successful alignment and transfer of narrow flakes on this type of structures, however, requires much more alignment precision. Such a device with a transferred graphene flake is shown in Figures B.2 (b-e).

Bibliography

[1] J. Bardeen and W. H. Brattain. The Transistor, A Semi-Conductor Triode. *Physical Review*, 74(2):230–231, 1948.

[2] J. S. Kilby and E. Keonjian. Design of a semiconductor-solid-circuit adder. In *1959 International Electron Devices Meeting*, volume 5, pages 76–78, 1959.

[3] G. E. Moore. Cramming more components onto integrated circuits, Reprinted from Electronics, volume 38, number 8, April 19, 1965, pp.114 ff. *IEEE Solid-State Circuits Society Newsletter*, 11(3):33–35, 2006.

[4] A. H. Atabaki, S. Moazeni, F. Pavanello, H. Gevorgyan, J. Notaros, L. Alloatti, M. T. Wade, C. Sun, S. A. Kruger, H. Meng, K. A. Qubaisi, I. Wang, B. Zhang, A. Khilo, C. V. Baiocco, M. A. Popović, V. M. Stojanović, and R. J. Ram. Integrating photonics with silicon nanoelectronics for the next generation of systems on a chip. *Nature*, 556(7701):349–354, 2018.

[5] H. J. Mamin and D. Rugar. Sub-attonewton force detection at millikelvin temperatures. *Applied Physics Letters*, 79(20):3358–3360, 2001.

[6] J. D. Teufel, T. Donner, M. A. Castellanos-Beltran, J. W. Harlow, and K. W. Lehnert. Nanomechanical motion measured with an imprecision below that at the standard quantum limit. *Nature Nanotechnology*, 4(12):820–823, 2009.

[7] E. Gavartin, P. Verlot, and T. J. Kippenberg. A hybrid on-chip optomechanical transducer for ultrasensitive force measurements. *Nature Nanotechnology*, 7(8):509–514, 2012.

[8] J. Moser, J. Güttinger, A. Eichler, M. J. Esplandiu, D. E. Liu, M. I. Dykman, and A. Bachtold. Ultrasensitive force detection with a nanotube mechanical resonator. *Nature Nanotechnology*, 8(7):493–496, 2013.

[9] Y. Tao, J. M. Boss, B. A. Moores, and C. L. Degen. Single-crystal diamond nanomechanical resonators with quality factors exceeding one million. *Nature Communications*, 5:3638, 2014.

[10] E. Forsen, G. Abadal, S. Ghatnekar-Nilsson, J. Teva, J. Verd, R. Sandberg, W. Svendsen, F. Perez-Murano, J. Esteve, E. Figueras, F. Campabadal, L. Montelius, N. Barniol, and A. Boisen. Ultrasensitive mass sensor fully integrated with complementary metal-oxide-semiconductor circuitry. *Applied Physics Letters*, 87(4):043507, 2005.

[11] Y. T. Yang, C. Callegari, X. L. Feng, K. L. Ekinci, and M. L. Roukes. Zeptogram-Scale Nanomechanical Mass Sensing. *Nano Letters*, 6(4):583–586, 2006.

[12] H.-Y. Chiu, P. Hung, H. W. C. Postma, and M. Bockrath. Atomic-Scale Mass Sensing Using Carbon Nanotube Resonators. *Nano Letters*, 8(12):4342–4346, 2008.

[13] K. Jensen, K. Kim, and A. Zettl. An atomic-resolution nanomechanical mass sensor. *Nature Nanotechnology*, 3(9):533–537, 2008.

[14] B. Lassagne, D. Garcia-Sanchez, A. Aguasca, and A. Bachtold. Ultrasensitive Mass Sensing with a Nanotube Electromechanical Resonator. *Nano Letters*, 8(11):3735–3738, 2008.

[15] J. Chaste, A. Eichler, J. Moser, G. Ceballos, R. Rurali, and A. Bachtold. A nanomechanical mass sensor with yoctogram resolution. *Nature Nanotechnology*, 7(5):301–304, 2012.

[16] A. N. Cleland and M. L. Roukes. A nanometre-scale mechanical electrometer. *Nature*, 392(6672):160–162, 1998.

[17] H. Okamoto, N. Kitajima, K. Onomitsu, R. Kometani, S.-i. Warisawa, S. Ishihara, and H. Yamaguchi. High-sensitivity charge detection using antisymmetric vibration in coupled micromechanical oscillators. *Applied Physics Letters*, 98(1):014103, 2011.

[18] D. Rugar, R. Budakian, H. J. Mamin, and B. W. Chui. Single spin detection by magnetic resonance force microscopy. *Nature*, 430(6997):329–332, 2004.

[19] C. L. Degen, M. Poggio, H. J. Mamin, C. T. Rettner, and D. Rugar. Nanoscale magnetic resonance imaging. *Proceedings of the National Academy of Sciences*, 106(5):1313–1317, 2009.

[20] R. G. Knobel and A. N. Cleland. Nanometre-scale displacement sensing using a single electron transistor. *Nature*, 424(6946):291–293, 2003.

[21] M. S. Hanay, S. Kelber, A. K. Naik, D. Chi, S. Hentz, E. C. Bullard, E. Colinet, L. Duraffourg, and M. L. Roukes. Single-protein nanomechanical mass spectrometry in real time. *Nature Nanotechnology*, 7(9):602–608, 2012.

[22] W. E. Newell. Miniaturization of Tuning Forks. *Science*, 161(3848):1320–1326, 1968.

[23] A.-C. Wong and C. T. C. Nguyen. Micromechanical mixer-filters ("mixlers"). *Journal of Microelectromechanical Systems*, 13(1):100–112, 2004.

[24] C. T.-C. Nguyen. MEMS technology for timing and frequency control. *IEEE Transactions on Ultrasonics, Ferroelectrics, and Frequency Control*, 54(2):251–270, 2007.

[25] X. L. Feng, C. J. White, A. Hajimiri, and M. L. Roukes. A self-sustaining ultrahigh-frequency nanoelectromechanical oscillator. *Nature Nanotechnology*, 3(6):342–346, 2008.

[26] L. G. Villanueva, R. B. Karabalin, M. H. Matheny, E. Kenig, M. C. Cross, and M. L. Roukes. A Nanoscale Parametric Feedback Oscillator. *Nano Letters*, 11(11):5054–5059, 2011.

[27] C. Chen, S. Lee, V. V. Deshpande, G.-H. Lee, M. Lekas, K. Shepard, and J. Hone. Graphene mechanical oscillators with tunable frequency. *Nature Nanotechnology*, 8(12):923–927, 2013.

[28] A. Uranga, J. Verd, and N. Barniol. CMOS–MEMS resonators: From devices to applications. *Microelectronic Engineering*. Micro and Nanofabrication Breakthroughs for Electronics, MEMS and Life Sciences, 132:58–73, 2015.

[29] A. D. O'Connell, M. Hofheinz, M. Ansmann, R. C. Bialczak, M. Lenander, E. Lucero, M. Neeley, D. Sank, H. Wang, M. Weides, J. Wenner, J. M. Martinis, and A. N. Cleland. Quantum ground state and single-phonon control of a mechanical resonator. *Nature*, 464(7289):697–703, 2010.

[30] J. D. Teufel, T. Donner, D. Li, J. W. Harlow, M. S. Allman, K. Cicak, A. J. Sirois, J. D. Whittaker, K. W. Lehnert, and R. W. Simmonds. Sideband cooling of micromechanical motion to the quantum ground state. *Nature*, 475(7356):359–363, 2011.

[31] J. Chan, T. P. M. Alegre, A. H. Safavi-Naeini, J. T. Hill, A. Krause, S. Gröblacher, M. Aspelmeyer, and O. Painter. Laser cooling of a nanomechanical oscillator into its quantum ground state. *Nature*, 478(7367):89–92, 2011.

[32] X. M. H. Huang, X. L. Feng, C. A. Zorman, M. Mehregany, and M. L. Roukes. VHF, UHF and microwave frequency nanomechanical resonators. *New Journal of Physics*, 7(1):247, 2005.

[33] A. Eichler, J. Moser, J. Chaste, M. Zdrojek, I. Wilson-Rae, and A. Bachtold. Nonlinear damping in mechanical resonators made from carbon nanotubes and graphene. *Nature Nanotechnology*, 6(6):339–342, 2011.

[34] J. P. Mathew, R. N. Patel, A. Borah, R. Vijay, and M. M. Deshmukh. Dynamical strong coupling and parametric amplification of mechanical modes of graphene drums. *Nature Nanotechnology*, 11(9):747–751, 2016.

[35] I. Tsioutsios, J. Moser, J. A. Plaza, and A. Bachtold. Controlled assembly of graphene sheets and nanotubes: Fabrication of suspended multi-element all-carbon vibrational structures. *Journal of Applied Physics*, 114(10):104310, 2013.

[36] J. L. Muñoz-Gamarra, P. Alcaine, E. Marigó, J. Giner, A. Uranga, J. Esteve, and N. Barniol. Integration of NEMS resonators in a 65nm CMOS technology. *Microelectronic Engineering*, 110:246–249, 2013.

[37] M. Imboden and P. Mohanty. Dissipation in nanoelectromechanical systems. *Physics Reports*. Dissipation in nano-electromechanical systems, 534(3):89–146, 2014.

[38] J. Chaste, M. Sledzinska, M. Zdrojek, J. Moser, and A. Bachtold. High-frequency nanotube mechanical resonators. *Applied Physics Letters*, 99(21):213502, 2011.

[39] E. A. Laird, F. Pei, W. Tang, G. A. Steele, and L. P. Kouwenhoven. A High Quality Factor Carbon Nanotube Mechanical Resonator at 39 GHz. *Nano Letters*, 12(1):193–197, 2012.

[40] V. Sazonova, Y. Yaish, H. Üstünel, D. Roundy, T. A. Arias, and P. L. McEuen. A tunable carbon nanotube electromechanical oscillator. *Nature*, 431(7006):284–287, 2004.

[41] C. Chen, S. Rosenblatt, K. I. Bolotin, W. Kalb, P. Kim, I. Kymissis, H. L. Stormer, T. F. Heinz, and J. Hone. Performance of monolayer graphene nanomechanical resonators with electrical readout. *Nature Nanotechnology*, 4(12):861–867, 2009.

[42] A. K. Hüttel, G. A. Steele, B. Witkamp, M. Poot, L. P. Kouwenhoven, and H. S. J. van der Zant. Carbon Nanotubes as Ultrahigh Quality Factor Mechanical Resonators. *Nano Letters*, 9(7):2547–2552, 2009.

[43] J. Moser, A. Eichler, J. Güttinger, M. I. Dykman, and A. Bachtold. Nanotube mechanical resonators with quality factors of up to 5 million. *Nature Nanotechnology*, 9(12):1007–1011, 2014.

[44] J. S. Bunch, A. M.v. d. Zande, S. S. Verbridge, I. W. Frank, D. M. Tanenbaum, J. M. Parpia, H. G. Craighead, and P. L. McEuen. Electromechanical Resonators from Graphene Sheets. *Science*, 315(5811):490–493, 2007.

[45] S. N. R. Kazmi, M. A. A. Hafiz, K. N. Chappanda, S. Ilyas, J. Holguin, P. M.F. J. Costa, and M. I. Younis. Tunable nanoelectromechanical resonator for logic computations. *Nanoscale*, 9(10):3449–3457, 2017.

[46] K. Wang and C. T. C. Nguyen. High-order medium frequency micromechanical electronic filters. *Journal of Microelectromechanical Systems*, 8(4):534–556, 1999.

[47] Y.-W. Lin, S. Lee, S.-S. Li, Y. Xie, Z. Ren, and C. T. C. Nguyen. Series-resonant VHF micromechanical resonator reference oscillators. *IEEE Journal of Solid-State Circuits*, 39(12):2477–2491, 2004.

[48] A. K. Naik, M. S. Hanay, W. K. Hiebert, X. L. Feng, and M. L. Roukes. Towards single-molecule nanomechanical mass spectrometry. *Nature Nanotechnology*, 4(7):445–450, 2009.

[49] A. Eichler, M. del Álamo Ruiz, J. A. Plaza, and A. Bachtold. Strong Coupling between Mechanical Modes in a Nanotube Resonator. *Physical Review Letters*, 109(2):025503, 2012.

[50] X. Song, M. Oksanen, M. A. Sillanpää, H. G. Craighead, J. M. Parpia, and P. J. Hakonen. Stamp Transferred Suspended Graphene Mechanical Resonators for Radio Frequency Electrical Readout. *Nano Letters*, 12(1):198–202, 2012.

[51] J. Gieseler, L. Novotny, and R. Quidant. Thermal nonlinearities in a nanomechanical oscillator. *Nature Physics*, 9(12):806–810, 2013.

[52] J. Gieseler, M. Spasenović, L. Novotny, and R. Quidant. Nonlinear Mode Coupling and Synchronization of a Vacuum-Trapped Nanoparticle. *Physical Review Letters*, 112(10):103603, 2014.

[53] B. Lassagne, Y. Tarakanov, J. Kinaret, D. Garcia-Sanchez, and A. Bachtold. Coupling Mechanics to Charge Transport in Carbon Nanotube Mechanical Resonators. *Science*, 325(5944):1107–1110, 2009.

[54] G. A. Steele, A. K. Hüttel, B. Witkamp, M. Poot, H. B. Meerwaldt, L. P. Kouwenhoven, and H. S.J.v. d. Zant. Strong Coupling Between Single-Electron Tunneling and Nanomechanical Motion. *Science*, 325(5944):1103–1107, 2009.

[55] M. Ganzhorn and W. Wernsdorfer. Dynamics and Dissipation Induced by Single-Electron Tunneling in Carbon Nanotube Nanoelectromechanical Systems. *Physical Review Letters*, 108(17):175502, 2012.

[56] A. Tavernarakis, J. Chaste, A. Eichler, G. Ceballos, M. Gordillo, J. Boronat, and A. Bachtold. Atomic Monolayer Deposition on the Surface of Nanotube Mechanical Resonators. *Physical Review Letters*, 112(19):196103, 2014.

[57] B. Dzyubenko, H.-C. Lee, O. E. Vilches, and D. H. Cobden. Surface electron perturbations and the collective behaviour of atoms adsorbed on a cylinder. *Nature Physics*, 11(5):398–402, 2015.

[58] V. Gouttenoire, T. Barois, S. Perisanu, J.-L. Leclercq, S. T. Purcell, P. Vincent, and A. Ayari. Digital and FM Demodulation of a Doubly Clamped Single-Walled Carbon-Nanotube Oscillator: Towards a Nanotube Cell Phone. *Small*, 6(9):1060–1065, 2010.

[59] Y. Xu, C. Chen, V. V. Deshpande, F. A. DiRenno, A. Gondarenko, D. B. Heinz, S. Liu, P. Kim, and J. Hone. Radio frequency electrical transduction of graphene mechanical resonators. *Applied Physics Letters*, 97(24):243111, 2010.

[60] A. M.v. d. Zande, R. A. Barton, J. S. Alden, C. S. Ruiz-Vargas, W. S. Whitney, P. H. Q. Pham, J. Park, J. M. Parpia, H. G. Craighead, and P. L. McEuen. Large-Scale Arrays of Single-Layer Graphene Resonators. *Nano Letters*, 10(12):4869–4873, 2010.

[61] M. Sansa, E. Sage, E. C. Bullard, M. Gély, T. Alava, E. Colinet, A. K. Naik, L. G. Villanueva, L. Duraffourg, M. L. Roukes, G. Jourdan, and S. Hentz. Frequency fluctuations in silicon nanoresonators. *Nature Nanotechnology*, 11(6):552–558, 2016.

[62] Y. T. Yang, C. Callegari, X. L. Feng, and M. L. Roukes. Surface Adsorbate Fluctuations and Noise in Nanoelectromechanical Systems. *Nano Letters*, 11(4):1753–1759, 2011.

[63] K. Y. Fong, W. H. P. Pernice, and H. X. Tang. Frequency and phase noise of ultrahigh Q silicon nitride nanomechanical resonators. *Physical Review B*, 85(16):161410, 2012.

[64] Y. Zhang, J. Moser, A. Bachtold, and M. I. Dykman. Interplay of driving and frequency noise in the spectra of vibrational systems. *arXiv:1406.1406 [cond-mat]*, 2014. arXiv: 1406.1406.

[65] M. H. Matheny, L. G. Villanueva, R. B. Karabalin, J. E. Sader, and M. L. Roukes. Nonlinear Mode-Coupling in Nanomechanical Systems. *Nano Letters*, 13(4):1622–1626, 2013.

[66] T. Miao, S. Yeom, P. Wang, B. Standley, and M. Bockrath. Graphene Nanoelectromechanical Systems as Stochastic-Frequency Oscillators. *Nano Letters*, 14(6):2982–2987, 2014.

[67] K. S. Novoselov, A. K. Geim, S. V. Morozov, D. Jiang, Y. Zhang, S. V. Dubonos, I. V. Grigorieva, and A. A. Firsov. Electric Field Effect in Atomically Thin Carbon Films. *Science*, 306(5696):666–669, 2004.

[68] P. R. Wallace. The Band Theory of Graphite. *Physical Review*, 71(9):622–634, 1947.

[69] X. Li, W. Cai, J. An, S. Kim, J. Nah, D. Yang, R. Piner, A. Velamakanni, I. Jung, E. Tutuc, S. K. Banerjee, L. Colombo, and R. S. Ruoff. Large-Area Synthesis of High-Quality and Uniform Graphene Films on Copper Foils. *Science*, 324(5932):1312–1314, 2009.

[70] A. K. Geim and K. S. Novoselov. The rise of graphene. *Nature Materials*, 6(3):183, 2007.

[71] S. Iijima. Helical microtubules of graphitic carbon. *Nature*, 354(6348):56, 1991.

[72] T. W. Ebbesen and P. M. Ajayan. Large-scale synthesis of carbon nanotubes. *Nature*, 358(6383):220–222, 1992.

[73] T. Guo, P. Nikolaev, A. Thess, D. T. Colbert, and R. E. Smalley. Catalytic growth of single-walled manotubes by laser vaporization. *Chemical Physics Letters*, 243(1):49–54, 1995.

[74] M. José-Yacamán, M. Miki-Yoshida, L. Rendón, and J. G. Santiesteban. Catalytic growth of carbon microtubules with fullerene structure. *Applied Physics Letters*, 62(2):202–204, 1993.

[75] A. H. Castro Neto, F. Guinea, N. M. R. Peres, K. S. Novoselov, and A. K. Geim. The electronic properties of graphene. *Reviews of Modern Physics*, 81(1):109–162, 2009.

[76] K. I. Bolotin, K. J. Sikes, Z. Jiang, M. Klima, G. Fudenberg, J. Hone, P. Kim, and H. L. Stormer. Ultrahigh electron mobility in suspended graphene. *Solid State Communications*, 146(9):351–355, 2008.

[77] L. Wang, I. Meric, P. Y. Huang, Q. Gao, Y. Gao, H. Tran, T. Taniguchi, K. Watanabe, L. M. Campos, D. A. Muller, J. Guo, P. Kim, J. Hone, K. L. Shepard, and C. R. Dean. One-Dimensional Electrical Contact to a Two-Dimensional Material. *Science*, 342(6158):614–617, 2013.

[78] I. Meric, M. Y. Han, A. F. Young, B. Ozyilmaz, P. Kim, and K. L. Shepard. Current saturation in zero-bandgap, top-gated graphene field-effect transistors. *Nature Nanotechnology*, 3(11):654–659, 2008.

[79] A. Mostofizadeh, Y. Li, B. Song, and Y. Huang. Synthesis, Properties, and Applications of Low-Dimensional Carbon-Related Nanomaterials. *Journal of Nanomaterials*, 2011:Article ID 685082, 2011.

[80] R. Saito, G. Dresselhaus, and M. S. Dresselhaus. *Physical Properties of Carbon Nanotubes*. Imperial College Press, 1998. Google-Books-ID: w5oHCWhA2EQC.

[81] M. S. Dresselhaus, G. Dresselhaus, and P. A. Vouris. *Carbon Nanotubes - Synthesis, Structure, Properties and Applications*, volume 27. Springer, 2001.

[82] M. Büttiker. Absence of backscattering in the quantum Hall effect in multiprobe conductors. *Physical Review B*, 38(14):9375–9389, 1988.

[83] J. Kong, E. Yenilmez, T. W. Tombler, W. Kim, H. Dai, R. B. Laughlin, L. Liu, C. S. Jayanthi, and S. Y. Wu. Quantum Interference and Ballistic Transmission in Nanotube Electron Waveguides. *Physical Review Letters*, 87(10):106801, 2001.

[84] E. D. Minot. *Tuning the band structure of carbon nanotubes*. PhD thesis, Cornell University, 2004.

[85] T. Dürkop, S. A. Getty, E. Cobas, and M. S. Fuhrer. Extraordinary Mobility in Semiconducting Carbon Nanotubes. *Nano Letters*, 4(1):35–39, 2004.

[86] P. Stiller. *Ultraclean carbon nanotubes and superconducting coplanar resonators: Materials, nano-electromechanics, and few-electron systems*. PhD thesis, Universität Regensburg, 2016.

[87] G. A. Steele, G. Gotz, and L. P. Kouwenhoven. Tunable few-electron double quantum dots and Klein tunnelling in ultraclean carbon nanotubes. *Nature Nanotechnology*, 4(6):363–367, 2009.

[88] B. H. Schneider, S. Etaki, H. S.J.v. d. Zant, and G. A. Steele. Coupling carbon nanotube mechanics to a superconducting circuit. *Scientific Reports*, 2:599, 2012.

[89] L. P. Kouwenhoven, C. M. Marcus, P. L. McEuen, S. Tarucha, R. M. Westervelt, and N. S. Wingreen. Electron Transport in Quantum Dots. In *Mesoscopic Electron Transport*, NATO ASI Series, pages 105–214. Springer, Dordrecht, 1997.

[90] M. J. Biercuk, S. Ilani, C. M. Marcus, and P. L. McEuen. Electrical Transport in Single-Wall Carbon Nanotubes. In *Carbon Nanotubes*, Topics in Applied Physics, pages 455–493. Springer, Berlin, Heidelberg, 2007.

[91] J. Moser, A. Barreiro, and A. Bachtold. Current-induced cleaning of graphene. *Applied Physics Letters*, 91(16):163513, 2007.

[92] O. L. Blakslee, D. G. Proctor, E. J. Seldin, G. B. Spence, and T. Weng. Elastic Constants of Compression - Annealed Pyrolytic Graphite. *Journal of Applied Physics*, 41(8):3373–3382, 1970.

[93] C. Lee, X. Wei, J. W. Kysar, and J. Hone. Measurement of the Elastic Properties and Intrinsic Strength of Monolayer Graphene. *Science*, 321(5887):385–388, 2008.

[94] M.-F. Yu, B. S. Files, S. Arepalli, and R. S. Ruoff. Tensile Loading of Ropes of Single Wall Carbon Nanotubes and their Mechanical Properties. *Physical Review Letters*, 84(24):5552–5555, 2000.

[95] E. D. Minot, Y. Yaish, V. Sazonova, J.-Y. Park, M. Brink, and P. L. McEuen. Tuning Carbon Nanotube Band Gaps with Strain. *Physical Review Letters*, 90(15):156401, 2003.

[96] B. Babić, J. Furer, S. Sahoo, S. Farhangfar, and C. Schönenberger. Intrinsic Thermal Vibrations of Suspended Doubly Clamped Single-Wall Carbon Nanotubes. *Nano Letters*, 3(11):1577–1580, 2003.

[97] A. Eichler, J. Chaste, J. Moser, and A. Bachtold. Parametric Amplification and Self-Oscillation in a Nanotube Mechanical Resonator. *Nano Letters*, 11(7):2699–2703, 2011.

[98] H. B. Callen and T. A. Welton. Irreversibility and Generalized Noise. *Physical Review*, 83(1):34–40, 1951.

[99] C. Chatfield. *The Analysis of Time Series: An introduction*. Chapman and Hall, 6th edition, 2004.

[100] L. D. Landau and E. M. Lifshitz. *Statistical Physics, Part 1*, volume 34. Butterworth-Heinemann, Amsterdam u.a, 3 edition edition, 1981.

[101] H. Nyquist. Thermal Agitation of Electric Charge in Conductors. *Physical Review*, 32(1):110–113, 1928.

[102] R. Lifshitz and M. C. Cross. Nonlinear Dynamics of Nanomechanical and Micromechanical Resonators. In H. G. Schuster, editor, *Reviews of Nonlinear Dynamics and Complexity*, pages 1–52. Wiley-VCH Verlag GmbH & Co. KGaA, 2008.

[103] B. D. Hauer, C. Doolin, K. S. D. Beach, and J. P. Davis. A general procedure for thermomechanical calibration of nano/micro-mechanical resonators. *Annals of Physics*, 339:181–207, 2013.

[104] D. W. Carr, S. Evoy, L. Sekaric, H. G. Craighead, and J. M. Parpia. Measurement of mechanical resonance and losses in nanometer scale silicon wires. *Applied Physics Letters*, 75(7):920–922, 1999.

[105] A. N. Cleland and M. L. Roukes. Fabrication of high frequency nanometer scale mechanical resonators from bulk Si crystals. *Applied Physics Letters*, 69(18):2653–2655, 1996.

[106] K. L. Ekinci, Y. T. Yang, X. M. H. Huang, and M. L. Roukes. Balanced electronic detection of displacement in nanoelectromechanical systems. *Applied Physics Letters*, 81(12):2253–2255, 2002.

[107] I. Bargatin, E. B. Myers, J. Arlett, B. Gudlewski, and M. L. Roukes. Sensitive detection of nanomechanical motion using piezoresistive signal downmixing. *Applied Physics Letters*, 86(13):133109, 2005.

[108] R. G. Beck, M. A. Eriksson, M. A. Topinka, R. M. Westervelt, K. D. Maranowski, and A. C. Gossard. GaAs/AlGaAs self-sensing cantilevers for low temperature scanning probe microscopy. *Applied Physics Letters*, 73(8):1149–1151, 1998.

[109] K. L. Ekinci, Y. T. Yang, and M. L. Roukes. Ultimate limits to inertial mass sensing based upon nanoelectromechanical systems. *Journal of Applied Physics*, 95(5):2682–2689, 2004.

[110] B. Lassagne, D. Ugnati, and M. Respaud. Ultrasensitive Magnetometers Based on Carbon-Nanotube Mechanical Resonators. *Physical Review Letters*, 107(13):130801, 2011.

[111] M. Li, E. B. Myers, H. X. Tang, S. J. Aldridge, H. C. McCaig, J. J. Whiting, R. J. Simonson, N. S. Lewis, and M. L. Roukes. Nanoelectromechanical Resonator Arrays for Ultrafast, Gas-Phase Chromatographic Chemical Analysis. *Nano Letters*, 10(10):3899–3903, 2010.

[112] I. Bargatin, E. B. Myers, J. S. Aldridge, C. Marcoux, P. Brianceau, L. Duraffourg, E. Colinet, S. Hentz, P. Andreucci, and M. L. Roukes. Large-Scale Integration of Nanoelectromechanical Systems for Gas Sensing Applications. *Nano Letters*, 12(3):1269–1274, 2012.

[113] T. P. Burg, M. Godin, S. M. Knudsen, W. Shen, G. Carlson, J. S. Foster, K. Babcock, and S. R. Manalis. Weighing of biomolecules, single cells and single nanoparticles in fluid. *Nature*, 446(7139):1066–1069, 2007.

[114] R. A. Barton, B. Ilic, S. S. Verbridge, B. R. Cipriany, J. M. Parpia, and H. G. Craighead. Fabrication of a Nanomechanical Mass Sensor Containing a Nanofluidic Channel. *Nano Letters*, 10(6):2058–2063, 2010.

[115] Z. Wang, J. Wei, P. Morse, J. G. Dash, O. E. Vilches, and D. H. Cobden. Phase Transitions of Adsorbed Atoms on the Surface of a Carbon Nanotube. *Science*, 327(5965):552–555, 2010.

[116] D. W. Allan. Time and Frequency (Time-Domain) Characterization, Estimation, and Prediction of Precision Clocks and Oscillators. *IEEE Transactions on Ultrasonics, Ferroelectrics, and Frequency Control*, 34(6):647–654, 1987.

[117] W. J. Riley. *Handbook of Frequency Stability Analysis*. National Institute of Standards and Technology, Washington, 2008.

[118] A. N. Cleland and M. L. Roukes. Noise processes in nanomechanical resonators. *Journal of Applied Physics*, 92(5):2758–2769, 2002.

[119] S. Schmid, L. G. Villanueva, and M. L. Roukes. *Fundamentals of Nanomechanical Resonators*. Springer International Publishing, 2016.

[120] J. R. Vig and Y. Kim. Noise in microelectromechanical system resonators. *IEEE Transactions on Ultrasonics, Ferroelectrics, and Frequency Control*, 46(6):1558–1565, 1999.

[121] J. Atalaya, A. Isacsson, and M. I. Dykman. Diffusion-induced dephasing in nanomechanical resonators. *Physical Review B*, 83(4):045419, 2011.

[122] K. L. Ekinci, X. M. H. Huang, and M. L. Roukes. Ultrasensitive nanoelectromechanical mass detection. *Applied Physics Letters*, 84(22):4469–4471, 2004.

[123] S. T. Bartsch, A. Rusu, and A. M. Ionescu. Phase-locked loop based on nanoelectromechanical resonant-body field effect transistor. *Applied Physics Letters*, 101(15):153116, 2012.

[124] O. Malvar, E. Gil-Santos, J. J. Ruz, D. Ramos, V. Pini, M. Fernandez-Regulez, M. Calleja, J. Tamayo, and A. San Paulo. Tapered silicon nanowires for enhanced nanomechanical sensing. *Applied Physics Letters*, 103(3):033101, 2013.

[125] M. Kumar and H. Bhaskaran. Ultrasensitive Room-Temperature Piezoresistive Transduction in Graphene-Based Nanoelectromechanical Systems. *Nano Letters*, 15(4):2562–2567, 2015.

[126] S. S. Narine and A. J. Slavin. Use of the quartz crystal microbalance to measure the mass of submonolayer deposits: Measuring the stoichiometry of surface oxides. *Journal of Vacuum Science & Technology A*, 16(3):1857–1862, 1998.

[127] T. Thundat, S. L. Sharp, W. G. Fisher, R. J. Warmack, and E. A. Wachter. Micromechanical radiation dosimeter. *Applied Physics Letters*, 66(12):1563–1565, 1995.

[128] J. Cao, Q. Wang, and H. Dai. Electron transport in very clean, as-grown suspended carbon nanotubes. *Nature Materials*, 4(10):745–749, 2005.

[129] J. Cao, Q. Wang, D. Wang, and H. Dai. Suspended Carbon Nanotube Quantum Wires with Two Gates. *Small*, 1(1):138–141, 2005.

[130] C. R. Dean, A. F. Young, I. Meric, C. Lee, L. Wang, S. Sorgenfrei, K. Watanabe, T. Taniguchi, P. Kim, K. L. Shepard, and J. Hone. Boron nitride substrates for high-quality graphene electronics. *Nature Nanotechnology*, 5(10):722–726, 2010.

[131] P. Weber, J. Güttinger, I. Tsioutsios, D. E. Chang, and A. Bachtold. Coupling Graphene Mechanical Resonators to Superconducting Microwave Cavities. *Nano Letters*, 14(5):2854–2860, 2014.

[132] P. Blake, E. W. Hill, A. H. Castro Neto, K. S. Novoselov, D. Jiang, R. Yang, T. J. Booth, and A. K. Geim. Making graphene visible. *Applied Physics Letters*, 91(6):063124, 2007.

[133] Z. H. Ni, H. M. Wang, J. Kasim, H. M. Fan, T. Yu, Y. H. Wu, Y. P. Feng, and Z. X. Shen. Graphene Thickness Determination Using Reflection and Contrast Spectroscopy. *Nano Letters*, 7(9):2758–2763, 2007.

[134] S. J. Cartamil Bueno. *Graphene Resonators with High Quality Factor Using a Substrate In- dependent Transfer Technique*. Master's thesis, Universidad Autonoma de Barcelona, 2012.

[135] W. Bao, K. Myhro, Z. Zhao, Z. Chen, W. Jang, L. Jing, F. Miao, H. Zhang, C. Dames, and C. N. Lau. In Situ Observation of Electrostatic and Thermal Manipulation of Suspended Graphene Membranes. *Nano Letters*, 12(11):5470–5474, 2012.

[136] C. Chen. *Graphene NanoElectroMechanical Resonators and Oscillators*. PhD thesis, Columbia University, 2013.

[137] M. Héritier, A. Eichler, Y. Pan, U. Grob, I. Shorubalko, M. D. Krass, Y. Tao, and C. L. Degen. Nanoladder Cantilevers Made from Diamond and Silicon. *Nano Letters*, 18(3):1814–1818, 2018.

[138] N. Rossi, F. R. Braakman, D. Cadeddu, D. Vasyukov, G. Tütüncüoglu, A. Fontcuberta i Morral, and M. Poggio. Vectorial scanning force microscopy using a nanowire sensor. *Nature Nanotechnology*, 12(2):150–155, 2017.

[139] L. M. de Lépinay, B. Pigeau, B. Besga, P. Vincent, P. Poncharal, and O. Arcizet. A universal and ultrasensitive vectorial nanomechanical sensor for imaging 2d force fields. *Nature Nanotechnology*, 12(2):156–162, 2017.

[140] F. R. Braakman, N. Rossi, G. Tütüncüoglu, A. F. i. Morral, and M. Poggio. Coherent Two-Mode Dynamics of a Nanowire Force Sensor. *Physical Review Applied*, 9(5):054045, 2018.

[141] J. Atalaya, A. Isacsson, and M. I. Dykman. Diffusion-Induced Bistability of Driven Nanomechanical Resonators. *Physical Review Letters*, 106(22):227202, 2011.

[142] C. Rhén and A. Isacsson. Particle number scaling for diffusion-induced dissipation in graphene and carbon nanotube nanomechanical resonators. *Physical Review B*, 93(12):125414, 2016.

[143] S. Stapfner, L. Ost, D. Hunger, J. Reichel, I. Favero, and E. M. Weig. Cavity-enhanced optical detection of carbon nanotube Brownian motion. *Applied Physics Letters*, 102(15):151910, 2013.

[144] V. Singh, S. J. Bosman, B. H. Schneider, Y. M. Blanter, A. Castellanos-Gomez, and G. A. Steele. Optomechanical coupling between a multilayer graphene mechanical resonator and a superconducting microwave cavity. *Nature Nanotechnology*, 9(10):820–824, 2014.

[145] X. Song, M. Oksanen, J. Li, P. Hakonen, and M. Sillanpää. Graphene Optomechanics Realized at Microwave Frequencies. *Physical Review Letters*, 113(2):027404, 2014.

[146] R. M. Cole, G. A. Brawley, V. P. Adiga, R. De Alba, J. M. Parpia, B. Ilic, H. G. Craighead, and W. P. Bowen. Evanescent-Field Optical Readout of Graphene Mechanical Motion at Room Temperature. *Physical Review Applied*, 3(2):024004, 2015.

[147] J. Güttinger, A. Noury, P. Weber, A. M. Eriksson, C. Lagoin, J. Moser, C. Eichler, A. Wallraff, A. Isacsson, and A. Bachtold. Energy-dependent path of dissipation in nanomechanical resonators. *Nature Nanotechnology*, 12(7):631–636, 2017.

[148] A. Tavernarakis, A. Stavrinadis, A. Nowak, I. Tsioutsios, A. Bachtold, and P. Verlot. Optomechanics with a hybrid carbon nanotube resonator. *Nature Communications*, 9(1):662, 2018.

[149] Q. Dong, Y. X. Liang, D. Ferry, A. Cavanna, U. Gennser, L. Couraud, and Y. Jin. Ultra-low noise high electron mobility transistors for high-impedance and low-frequency deep cryogenic readout electronics. *Applied Physics Letters*, 105(1):013504, 2014.

[150] R. B. Anderson and P. H. Emmett. Measurement of Carbon Black Particles by the Electron Microscope and Low Temperature Nitrogen Adsorption Isotherms. *Journal of Applied Physics*, 19(4):367–373, 1948.

[151] A. Castellanos-Gomez, M. Buscema, R. Molenaar, V. Singh, L. Janssen, H. S.J.v. d. Zant, and G. A. Steele. Deterministic transfer of two-dimensional materials by all-dry viscoelastic stamping. *2D Materials*, 1(1):011002, 2014.

[152] M. Yang, A. Nurbawono, C. Zhang, R. Wu, Y. Feng, and Ariando. Manipulating absorption and diffusion of H atom on graphene by mechanical strain. *AIP Advances*, 1(3):032109, 2011.

[153] H. H. Pérez Garza, E. W. Kievit, G. F. Schneider, and U. Staufer. Controlled, Reversible, and Nondestructive Generation of Uniaxial Extreme Strains (>10%) in Graphene. *Nano Letters*, 14(7):4107–4113, 2014.

[154] V. Freulon. *Etude de la décohérence de paquets d'onde monoélectroniques dans les canaux de bord de l'effet Hall quantique entier. Mesoscopic Systems and Quantum Hall Effect*. PhD thesis, Ecole Normale Supérieure, 2014.

[155] R. A. Barton, B. Ilic, A. M. van der Zande, W. S. Whitney, P. L. McEuen, J. M. Parpia, and H. G. Craighead. High, Size-Dependent Quality Factor in an Array of Graphene Mechanical Resonators. *Nano Letters*, 11(3):1232–1236, 2011.

[156] D. Garcia-Sanchez, A. M. van der Zande, A. S. Paulo, B. Lassagne, P. L. McEuen, and A. Bachtold. Imaging Mechanical Vibrations in Suspended Graphene Sheets. *Nano Letters*, 8(5):1399–1403, 2008.